CHEMICAL AND DYNAMICAL CHARACTERISTICS OF

STRATOSPHERE-TROPOSPHERE EXCHANGE

A Dissertation

by

CAMERON ROSS HOMEYER

Submitted to the Office of Graduate Studies of
Texas A&M University
in partial fulfillment of the requirements for the degree of

DOCTOR OF PHILOSOPHY

August 2012

Major Subject: Atmospheric Sciences

CHEMICAL AND DYNAMICAL CHARACTERISTICS OF

STRATOSPHERE-TROPOSPHERE EXCHANGE

A Dissertation

by

CAMERON ROSS HOMEYER

Submitted to the Office of Graduate Studies of
Texas A&M University
in partial fulfillment of the requirements for the degree of

DOCTOR OF PHILOSOPHY

Approved by:

Chair of Committee,   Kenneth P. Bowman
Committee Members,   Andrew Dessler
   Craig Epifanio
   Istvan Szunyogh
   Steven F. DiMarco
Head of Department,   Kenneth P. Bowman

August 2012

Major Subject: Atmospheric Sciences

ABSTRACT

Chemical and Dynamical Characteristics of

Stratosphere-Troposphere Exchange. (August 2012)

Cameron Ross Homeyer, B.S., Texas A&M University;

M.S., Texas A&M University

Chair of Advisory Committee: Kenneth P. Bowman

Stratosphere-troposphere exchange processes are responsible for controlling the distribution of chemically and radiatively important trace gases in the upper troposphere and lower stratosphere. Extensive characterization of exchange processes is critical to the development of our understanding and prediction of the climate system. This study examines the occurrence and dynamical and chemical characteristics related to two primary stratosphere-troposphere exchange processes: Rossby wavebreaking and moist convection.

Intrusions of air from the tropical upper troposphere into the extratropical stratosphere above the subtropical jet via Rossby wavebreaking potentially have a significant impact on the composition of the lowermost stratosphere (the stratospheric part of the "middleworld"). We first present an analysis of tropospheric intrusion events observed in aircraft observations using kinematic and chemical diagnostics. The transport processes operating during each event are discussed using high-resolution model analyses and backward trajectory calculations. In situ chemical observations of the tropospheric intrusions are used to estimate the mixing timescales of the observed intrusions through use of a simple box model and trace species with different photochemical lifetimes. We estimate that the timescale for an intrusion to mix with the background stratospheric air is 5 to 6 days. Detailed analysis of small-scale features with tropospheric characteristics observed in the stratosphere suggests frequent irre-

versible transport associated with tropospheric intrusions. We also present a 30-year climatology (1981–2010) of anticyclonically and cyclonically sheared Rossby wave-breaking events along the boundary of the tropics in the 350–500 K potential temperature range from ECMWF ERA-Interim reanalyses. Lagrangian transport analyses show poleward transport at altitudes below and above the 370–390 K layer. Poleward transport at lower levels is in disagreement with previous studies and is shown to be largely dependent on the choice of tropical boundary. In addition, transport analyses reveal three modes of transport for anticyclonic wavebreaking events near the tropical tropopause (380 K): poleward, equatorward, and bidirectional. These transport modes are associated with distinct characteristics in the geometry of the mean flow.

Stratospheric intrusions (tropopause folds) are known to be major contributors to stratosphere-troposphere exchange. The specific mixing processes that lead to irreversible exchange between stratospheric intrusions and the surrounding troposphere, however, are not entirely understood. This study presents direct observations of moist convection penetrating into stratospheric intrusions. The characteristics of convective injection are shown by using in situ aircraft measurements, radar reflectivities, and model analyses. Convective injection is observed at altitudes up to 5 km above the bottom of a stratospheric intrusion. Aircraft measurements show that convective injection in stratospheric intrusions can be uniquely identified by coincident observations of water vapor greater than about 100 ppmv and ozone greater than about 125 ppbv. Trajectory analyses show that convective injection can impact transport in both directions: from troposphere to stratosphere and from stratosphere to troposphere. We present a conceptual model of the synoptic meteorological conditions conducive to convective injection in stratospheric intrusions. In particular, convective injection is found to be associated with a "split front" where the upper-level frontal boundary outruns the surface cold front.

ACKNOWLEDGMENTS

TABLE OF CONTENTS

LIST OF TABLES

LIST OF FIGURES

FIGURE   Page

FIGURE   Page

CHAPTER I

INTRODUCTION

The mechanisms of stratosphere-troposphere exchange (STE) continue to be an area of active research. The influence of STE on the composition of the upper troposphere and lower stratosphere (UTLS), particularly in the "middleworld" [2], has important consequences for chemistry, climate and the radiation budget. As outlined in [3] and [4], STE is not fully understood due to the existence of multiple transport pathways in the UTLS and the irregular occurrence of many exchange events.

STE can occur in both directions: stratosphere-to-troposphere transport (STT) and troposphere-to-stratosphere transport (TST). TST has several commonly-occurring transport pathways. The dominant method of TST is slow ascent in the tropics associated with the Brewer-Dobson circulation [5, 6]. There are also several important mechanisms for TST that take place on shorter timescales. For example, upwelling in the Asian monsoon anticyclone is a topic of active research [[7], and references therein]. Additionally, TST through isentropic transport of air from the tropical upper troposphere into the midlatitude lowermost stratosphere above the subtropical jet (370–400 K potential temperature range) has received recent attention [e.g., 8, 9, 10, 11]. [10] label these exchange events as tropospheric intrusions, parallel to the term "stratospheric intrusions". They provide diagnostic methods for identifying tropospheric intrusions by using static stability and the occurrence of secondary tropopauses. It is well known that tropospheric intrusions have been observed as low ozone laminae in the stratosphere in many previous studies [e.g., 12]. Irreversibility and frequency of low ozone laminae has received increasing attention [e.g., 9].

The journal model is *IEEE Transactions on Automatic Control.*

At this time extensive research on the detailed chemical composition, frequency and dynamical evolution of these events has not been done.

Tropospheric intrusions have been shown to accompany large-scale Rossby wave-breaking [13] events in the UTLS in previous studies [e.g., 14, 15, 16, 17, 10]. Rossby wavebreaking, however, is known to be a two-way transport mechanism and there have also been studies focused on intrusions of extratropical LS air into the tropical UT [e.g., 18, 19]. Two established methods for identifying wavebreaking from fields of potential vorticity (PV) or a similar dynamical quantity on surfaces of potential temperature can be found in the literature. [20] provide a method for identifying Rossby wavebreaking events as meridional gradient reversals (folds) of PV. [21] identify Rossby wavebreaking events as streamers and cut-off features of PV which, during most lifecycles, evolve into meridional gradient reversals. Although these approaches are distinct characterizations of wavebreaking, analyses from both methods are comparable [e.g., 20, 21, 22, 23]. In addition, analyses of breaking Rossby waves have typically included the separation of events by their evolution. Namely, whether they occur in areas of anticyclonic or cyclonic shear and whether they break predominantly poleward or equatorward. [24] propose the classification of equatorward breaking waves as type LC1 (anticyclonic) or LC2 (cyclonic). [25] similarly classify poleward breaking waves as type P1 (cyclonic) or P2 (anticyclonic). All four types have been the focus of meridional fluxes of Rossby wave activity in recent studies [e.g., 26, 27].

There have been several modeling studies that examine the dependence of wavebreaking evolution on the structure of the jet. The primary direction of breaking Rossby waves is illustrated to be dependent on asymmetries of the mean flow in either the zonal or meridional direction, and the nearer critical line in the meridional direction [e.g., 28, 25]. Although these modeling studies illustrate that distinct idealized jet structures can produce wavebreaking in either or both directions, the

dependence of wavebreaking direction on the mean flow in observations of the UTLS is not known. Previous observational studies suggest that poleward wavebreaking events above the subtropical jet may be associated with a double jet structure in the meridional direction [e.g., 10]. Analysis of individual poleward wavebreaking events, such as that given in Figure 2 discussed below, show that the double jet structure can be result of the subtropical jet splitting, migrating poleward on the upstream side of the wavebreaking event and overrunning the equatorward subtropical jet downstream.

As discussed in [10], Rossby wavebreaking has not been studied extensively in the 370–400 K potential temperature range where tropospheric intrusions have been observed. Previous studies have largely focused on wavebreaking at the tropopause in the 320–360 K potential temperature range, often below and poleward of the subtropical jet. The frequency and preferential regions of Rossby wavebreaking at 350 K illustrated in previous studies suggest that tropospheric intrusions, at least from Rossby wavebreaking, occur commonly in the central Pacific and western Atlantic and have significant seasonal variability [e.g., 20, 29, 23]. The frequency of Rossby wavebreaking at 350 K has been shown to peak in late spring into summer.

Another possible source for tropospheric intrusions is through Rossby wavebreaking in the so-called "westerly ducts" where mean westerly winds occur in the tropics. Climatological mean westerlies are found in the tropical upper troposphere in two regions of the northern hemisphere, predominantly in winter and spring. The southernmost jet is found in the east Pacific between ∼180° and 225° longitude and centered at ∼15°N latitude. The second is found over the tropical Atlantic ocean and centered at ∼20°N latitude. Figure 1 shows the climatological mean zonal wind speed on the 350 K isentropic surface for the tropics and northern hemisphere midlatitudes for April–June 1981-2010 from the European Center for Medium-Range Weather Forecasts ERA-Interim Reanalysis [30]. The 350 K isentropic surface is often at the core

of the subtropical jet and tropical westerly ducts. These westerly ducts are favorable for cross-equatorial propagation of Rossby waves, while easterly winds, which occur throughout most of the tropics, inhibit propagation [e.g., 31]. The westerly ducts also have a strong association with the El Niño-Southern Oscillation (ENSO). In particular, the Pacific westerly duct is considerably stronger during the ENSO cold phase (or La Niña) and equatorward Rossby wave propagation is increased [32]. [33] show that within these ducts Rossby wavebreaking creates distinct transport routes for tropical air near the tropopause into the midlatitude lower stratosphere, particularly during the winter season. [18] further associate intrusions of midlatitude air into the tropics, which are often accompanied by tropospheric intrusions, with the strength of the westerly ducts and ENSO phase. Although this method of transport also involves Rossby wavebreaking, equatorward propagating waves breaking in the westerly ducts are responsible for transport in this case. It is also not immediately known if this type of wavebreaking results in significant meridional folding of PV contours.

As discussed previously, the climatological distribution and seasonality of wavebreaking at lower potential temperature levels (320–360 K) is well understood while wavebreaking and transport between the tropical UTLS and extratropical LS in the 370–400 K potential temperature range has not been adequately investigated. In addition, the irreversible transport properties of wavebreaking events between the troposphere and stratosphere are not entirely understood. [34] illustrate that the dependence of mixing (or transport) intensity along the tropopause in the northern hemisphere reaches a maximum over the Atlantic region, while a secondary maximum is observed over the Pacific region, consistent with previous climatologies of wavebreaking frequency. The analyses presented in [34] relate the observed maximum in mixing over the Atlantic to the dual meridional structure of the jet (see Figure 1). There are also several studies of isentropic transport and mixing be-

tween the tropics and extratropics, which is dominated by Rossby wavebreaking [e.g., 35, 36, 37, 38, 39, 40]. As is true for investigations of Rossby wavebreaking frequency, isentropic transport studies have largely been limited to potential temperature levels at or below 360 K and above 500 K. It is evident from these analyses, however, that quantitative estimates of transport are largely sensitive to the dynamical representation of the tropopause and collectively show net stratosphere-to-troposphere transport at potential temperature levels at or below 350 K.

Transport calculations depend on how the boundaries between domains of interest are defined. Because of its quasi-conservative nature, potential vorticity is commonly used to define the boundary between the tropics and extratropics, or between the stratosphere and troposphere, but quantitative transport calculations can depend strongly on the value of the PV surface used to define the boundary. Furthermore, previous studies have shown that large differences exist in the characterization of the UTLS between PV as a troposphere-stratosphere boundary and the lapse-rate tropopause [e.g., 41, 42]. An example of the sensitivity of transport estimates to the choice of troposphere-stratosphere boundary for an anticyclonic Rossby wavebreaking event is given in Figure 2. Three PV contours are shown (3, 4, and 5 pvu where 1 pvu = 10^{-6} K m^2 kg^{-1} s^{-1}) and offer representations the boundary between the tropical upper troposphere and extratropical lower stratosphere at 350 K during this time period. During the mature stage of the breaking wave (Fig. 2a), the 4 and 5 pvu contours show characteristic folding in the meridional direction, while the 3 pvu contour is confined to the larger tropical reservoir. Away from the wavebreaking region, all three contours lie within a tight latitudinal range along the strong PV gradient observed between the tropics and extratropics. As the breaking wave evolves and separates from the tropical reservoir downstream, the 4 and 5 pvu contours show significant transport of tropical UT air into the extratropical LS (Fig. 2b). At 2 and 4

days later (Figs. 2c & 2d), the air mass has been further stretched and mixed into the extratropical LS, evidenced by decreasing area enclosed by the PV contours. In this example, a choice of 3 pvu as the troposphere-stratosphere boundary would result in no wavebreaking identification and therefore no identification of transport. If 4 or 5 pvu are used as the boundary, troposphere-to-stratosphere transport would be identified, but at significantly different magnitudes. Therefore, the dynamical representation of the tropopause is essential for accurate estimations of transport for individual events and consequently, the net annual transport direction (TST or STT) at a given altitude. As will be shown in Chapter IIIB1, 4 pvu is considered to be the best representation of the boundary between tropics and extratropics at 350 K, illustrated in Figure 2 by the increased contour thickness and division between red (tropical) and blue (extratropical) air masses.

In addition to wavebreaking, there are several mechanisms for stratosphere-to-troposphere transport. Stratospheric intrusions (tropopause folds) are an important STT mechanism, and have been the focus of many research studies and aircraft experiments [e.g, 43, 44, 45, 46, 47, 48, 49, 11]. There are several known processes that lead to irreversible exchange (mixing) of air between stratospheric intrusions and the surrounding troposphere during their lifecycles. Many of these are collectively referred to as clear air turbulence [e.g., 50, 51, 44]. Mechanisms for generation of clear air turbulence include inertio-gravity waves [e.g., 52], Kelvin-Helmholtz instabilities [e.g., 44] and boundary layer mixing [e.g., 53]. Diabatic processes such as latent heating and radiative cooling associated with clouds near the tropopause can also be important [e.g. 54, 55]. Filamentation and roll-up of intrusions into vortices that interleave tropospheric and stratospheric air masses is a significant mixing process [e.g., 47]. Convection is also a potential source of irreversible mixing during stratospheric intrusions. The impacts of convective injection could be large given the deep descent of

intrusions into the troposphere and the ability of convection to rapidly transport air vertically. Convective injection of tropospheric air into stratospheric intrusions has been inferred from observations, but has not been observed directly [e.g., 56, 57, 58]. The analyses presented in this study, however, show direct observations of convective injection.

Stratospheric intrusions occur outside of the tropics, and they have distinct climatological characteristics in terms of their depth and seasonality. The frequency of stratospheric intrusions has been found to be highest along the subtropical jet stream and the magnitude of stratosphere-to-troposphere transport in general is larger in middle latitudes and during the winter and spring seasons [e.g., 18, 38, 59, 60, 61, 62]. Although they are more common in the subtropics, individual stratospheric intrusions tend to be deeper (descend to lower altitudes) and have stronger mass exchange fluxes along the polar jet stream in midlatitudes [e.g., 60, 62]. [61] show that the deepest exchange events are often found over the ocean storm track regions, which coincide with areas of deep, explosive cyclogenesis [e.g., 63, 64].

The dynamics of stratospheric intrusions have been discussed widely in the literature, largely in the context of upper-level frontal systems [e.g., 65]. These intrusions, characterized by descent below the cyclonic side of an upper-tropospheric jet stream, are the product of a vertical ageostrophic circulation resulting from interactions between horizontal temperature gradients and the geostrophic wind [e.g., 66, 67, 68, 69]. The ageostrophic circulation, as illustrated in [66], can be calculated directly for a two-dimensional frontal cross section by using the Sawyer-Eliassen secondary circulation equation [70, 71]. Large-scale ageostrophic motions from acceleration and curvature effects of the jet stream tend to strengthen the cross-front circulation on the upstream side of a large-amplitude trough and weaken the circulation on the downstream side. The direction and magnitude of the circulation are important for the evolution and

large-scale transport of the intrusion.

There is some indirect evidence for convective injection of tropospheric air into stratospheric intrusions. [56] use ground based lidar (ozone & aerosol), satellite water vapor images, and radiosonde measurements to suggest that the sudden disappearance of a stratospheric intrusion is the result of moist convective injection. [57] use VHF radar to estimate turbulence, convective injection, and mixing in an observed stratospheric intrusion, but lack in situ measurements to confirm the radar observations. Their analysis also suggests that convective injection in stratospheric intrusions is rare, at least in their radar dataset over Aberystwyth, UK (1 in 17 cases of observed turbulence). The turbulent mixing observed during the convective event in [57] was comparable to the strongest shear turbulence observed. [58] suggest that variability in ozone and relative humidity below an observed stratospheric intrusion over Hawaii is the result of convective injection into the intrusion. The authors use aircraft data and infrared satellite brightness temperature to associate the observed variability with coincident convection.

A considerable amount of attention has been given to the occurrence of convection that overshoots the lapse-rate tropopause [e.g., 72, 73, 74, 75, 76, 77, 78, 79]. Although the chemical impacts of overshooting convection and convective injection into stratospheric intrusions may be comparable (both mix tropospheric boundary layer and stratospheric air), they occur under significantly different dynamical conditions. The boundary between a descending stratospheric intrusion and tropospheric air, as identified by potential vorticity and trace constituents, is often several kilometers below the lapse-rate tropopause as defined by the World Meteorological Organization (WMO) definition [80]. This is especially true in model analyses, where the vertical resolution may not be sufficient to resolve the stability structure [e.g., 81]. Much of the air in a stratospheric intrusion can return to the stratosphere, but

convective injection into stratospheric intrusions may not be identified correctly as troposphere to stratosphere transport because the top of the convection lies below the lapse-rate tropopause. To put this another way, in the vicinity of stratospheric intrusions the lapse-rate tropopause may not be a good indicator of the boundary between tropospheric and stratospheric air.

In this study, we analyze tropospheric intrusions and stratospheric intrusions sampled during the Stratosphere-Troposphere Analyses of Regional Transport 2008 (START08) experiment [11]. One goal is to study the transport mechanisms associated with tropospheric intrusions in further detail. In our analysis, we show the dynamical evolution of each event by using high-resolution meteorological analyses from the operational NCEP Global Forecast System (GFS) model. We also use back trajectories to show the source region and transport pathway of each air mass and its relationship to the local meteorological and dynamical field. Another goal of this study is to characterize the chemical properties of the observed tropospheric intrusions. We use trace constituents with various sources to relate the observed atmospheric composition to the large-scale dynamical fields. Also, by using a simple box model and a selection of gases with tropospheric sources and varying lifetime, we provide an estimate of the mixing timescale for the observed tropospheric intrusion events. A short global analysis of tropospheric intrusions in the 370–400 K potential temperature range during the START08 experiment period is also given. We also present direct aircraft observations of convection penetrating into two stratospheric intrusions observed during START08. The convective injection is identified by using in situ trace gas and microphysical measurements, three-dimensional radar reflectivities, and model analyses from the NCEP GFS. Trace constituents with tropospheric and stratospheric sources are used to identify relationships inherent to convective injection in stratospheric intrusions. We present an additional case study using only

model analyses and radar reflectivities to illustrate the relationship between synoptic meteorological conditions and the occurrence of convective injection. In addition, forward trajectories are used to show that two-way exchange of air between the stratosphere and troposphere is possible due to convective injection into tropopause folds.

One additional goal of this study is to further characterize the occurrence and transport properties of Rossby wavebreaking between the tropics and extratropics above the subtropical jet. We use ERA-Interim reanalyses to identify wavebreaking events in the 350–500 K potential temperature range, a layer spanning the tropical UTLS and extratropical LS. We present a seasonally dependent representation of the boundary between troposphere and stratosphere (or tropics and extratropics) for wavebreaking identification. For transport identification, we employ a Lagrangian method similar to that of [38] to represent mixing of the tropical (extratropical) air into the extratropics (tropics). Composite mean dynamical states for wavebreaking events are also shown to illustrate the dependence of transport direction on the mean flow.

CHAPTER II

DATA

A. START08 Data

During April to June of 2008, the START08 project used the National Science Foundation – National Center for Atmospheric Research (NSF-NCAR) Gulfstream V (GV) aircraft to investigate trace gas distributions for a variety of meteorological situations. The focus was on UTLS transport, but research flights also targeted gravity wave events and convection. For START08 the GV payload was designed to measure atmospheric trace constituents in the UTLS and to study their relationship to transport processes. The GV aircraft flew 18 flights during the project and sampled strong tropospheric intrusions during two flights: Research Flights 1 and 14 (RF01 and RF14). Additionally, during several flights the aircraft encountered air with tropospheric characteristics in the extratropical lower stratosphere that were not part of tropospheric intrusions observed in the model analyses within a week prior to the observation time. The GV aircraft made extensive measurements in stratospheric intrusions during 4 flights. During Research Flights 12 (RF12) and 6 (RF06), the aircraft flew through and near the tops of convective clouds penetrating into stratospheric intrusions.

The START08 flights reached from the Gulf of Mexico to Canada ($\sim$25° to 65°N) and from $\sim$120° to 85°W while reaching a maximum altitude of $\sim$14.3 km. A description of the instrument payload can be found in [11]. Many of the parameters measured by instruments on the GV are sampled at 1 Hz, although some trace gas instruments measured less frequently, such as the Advanced Whole Air Sampler (AWAS). The spatial resolution of the 1 Hz data is about 200 m at standard cruise speed.

In our analysis we use trace constituents that are useful for diagnosing mixing and large-scale transport. These include ozone (O_3), carbon monoxide (CO), water vapor (H_2O), and several additional trace species with anthropogenic and/or natural sources at the surface. Ozone data are from the National Oceanic and Atmospheric Administration (NOAA) dual-beam ultraviolet (UV) absorption ozone photometer [82]. The NOAA ozone instrument has a precision of 0.6 ppbv and an accuracy of 3%. Carbon monoxide data are from the NCAR Research Aviation Facility (RAF) vacuum UV resonance fluorescence instrument (similar to that in [83]). The RAF carbon monoxide instrument has a precision of 2 ppbv and an accuracy of 5%. Water vapor data are from the vertical cavity surface emitting laser (VCSEL) instrument [84]. The VCSEL hygrometer has a precision of <3% and an accuracy of 6%. For the remaining constituents, we use measurements from the AWAS instrument. The AWAS instrument captures up to 60 samples per flight in stainless-steel canisters, with each canister pressurized to ∼3 atmospheres. The time required for AWAS to collect a sample is between ∼10 and 40 s, depending on altitude. Samples are analyzed following each flight by using gas chromatography and mass spectrometry to determine the mixing ratio of a large number of trace species. A list of the AWAS trace gases used in our analysis, their approximate lifetimes, and estimates of precision and accuracy is given in Table I. We also use ice particle measurements for cloud identification. Ice particle mean diameter data are from the small ice detector probe (SID-2H). The SID-2H probe infers particle shape by measuring forward scattering intensity at 28 angles around each ice particle using a laser with a wavelength of 532 nm. During START08, the size range measured by the SID-2H probe was ∼5–50 μm.

B.   GFS Data

For dynamical analysis and trajectory calculations for START08 flights, we use the gridded analyses produced by the NCEP Global Data Assimilation System (GDAS) for the high-resolution GFS spectral model. The GFS analyses are assimilated on a Gaussian grid with a longitude-latitude resolution of $0.3125° \times \sim 0.3125°$ (~ 35 km) and 64 hybrid sigma-pressure levels in the vertical. In the UTLS the vertical resolution is typically 500-1000 m. Analyses are provided daily at 00, 06, 12, and 18 UTC on a 47-level pressure grid. For comparison with in situ observations from START08, the GFS analyses are linearly interpolated in space and time to each flight track.

C.   ERA-Interim Data

For Rossby wavebreaking climatology, we use 30 years (1981–2010) of the ERA-Interim global atmospheric reanalysis produced by the European Center for Medium-Range Weather Forecasts (ECMWF). Reanalyses are provided daily at 00, 06, 12, and 18 UTC on a horizontal Gaussian grid with a longitude-latitude resolution of $0.75° \times \sim 0.75°$ (~ 80 km) and 37 pressure levels in the vertical. For Rossby wave-breaking identification and trajectory calculations, data are linearly interpolated to a $1.5° \times 1.5°$ horizontal grid and 9 potential temperature levels in the vertical: 350, 360, 370, 380, 390, 400, 420, 450, and 500 K.

D.   NEXRAD Data

To identify the coverage and vertical extent of convection, we use Next Generation Weather Radar (NEXRAD) program Weather Surveillance Radar – 1988 Doppler (WSR-88D) level II data provided by the National Climatic Data Center (NCDC)

[85]. The level II three-dimensional radar data are available on native spherical grids. Temporal and spatial resolution of the data varies depending on meteorology, operating status, and range from the radar. The typical time between volume scans during precipitation events is 5 to 10 minutes. For comparison with in situ observations and GFS analyses, radar data are interpolated in space and time, if necessary.

For convenience the NEXRAD level II radar data are transformed to a Cartesian grid. We use the National Center for Atmospheric Research Earth Observing Laboratory (NCAR EOL) REORDER software for grid transformation. The analysis uses a Cressman distance-weighting scheme with a vertical resolution of 250 m and a horizontal resolution of 2 km. For comparison with GFS analyses, we combine observations from several radars by space and time interpolation and averaging, if necessary.

CHAPTER III

METHODS

Trajectory analyses of the observed tropospheric and stratospheric intrusions follow the methods given in [86]. In this study higher-resolution, three-dimensional GFS analysis wind fields are used with the TRAJ3D trajectory model of [87] and [88] for START08 flights. For Rossby wavebreaking climatology, ERA-Interim reanalysis wind fields are used.

A.   Tropospheric Intrusion Box Model

We use a simple box model to help understand the evolution of the mixing ratios of trace species in the tropospheric intrusions observed during START08. The goal of this exercise is to develop some quantitative insight into the relative importance of the various processes that affect the composition of the intrusion. In particular, we are interested in estimating the timescale for mixing of these air masses with the surrounding stratospheric air. The trace species of interest have natural or anthropogenic sources in the lower troposphere or at the surface. This model is similar in concept to previous studies that estimated mixing timescales for entrainment of midlatitude air into the tropical lower stratosphere, although in this case we apply the model to individual intrusions, rather than the climatological effect of multiple transport events [e.g., 89, 90, 91].

We model the evolution of the composition of an air parcel that originates in the tropical upper troposphere or lower stratosphere and moves into the extratropical lower stratosphere. The mixing ratios of the species of interest, which have no sources in the UTLS, change due to photochemical losses and in-mixing of stratospheric background air as the intruding air masses move from the tropics into the extratropics.

The background stratospheric air normally has a lower mixing ratio than the relatively young air in the intrusion. We model the change in mixing ratio of a given species as

$$\frac{d\chi}{dt} = -\frac{\chi}{\tau_s} + \frac{\chi_s - \chi}{\tau_m} \qquad (3.1)$$

where χ is the mixing ratio of the species of interest in the intrusion, χ_s is its background stratospheric mixing ratio, τ_s is its chemical lifetime in the lower stratosphere (known from experiment), and τ_m is the timescale for mixing of background stratospheric air into the intrusion. The second term on the r.h.s. of (3.1) represents the dilution of the intruding air mass by background stratospheric air. The initial mixing ratio in the tropical upper troposphere and lower stratosphere at $t = 0$ is $\chi(0) = \chi_{TTL}$.

The general solution to (3.1) is

$$\chi(t_s) = \chi_{TTL}\, e^{-(\frac{1}{\tau_s} + \frac{1}{\tau_m})t_s} + \frac{\chi_s}{1 + \frac{\tau_m}{\tau_s}}\left(1 - e^{-(\frac{1}{\tau_s} + \frac{1}{\tau_m})t_s}\right) \qquad (3.2)$$

The mixing ratios inside and outside of the intruding air mass, $\chi(t_s)$ and χ_s, are obtained from in situ measurements by the GV aircraft as it flew through the intrusions and the surrounding stratospheric air. The time since the intruding air mass left the tropical upper troposphere, t_s, is estimated from back trajectories of parcels in the core of the intrusion.

During START08 the GV measured trace gas mixing ratios in the extratropical troposphere, but not in the tropical upper troposphere where the intrusion started. Therefore, we model χ_{TTL} as

$$\chi_{TTL} = \chi_t\, e^{-\frac{1}{\tau_t}t_t} \qquad (3.3)$$

where χ_t is the average extratropical tropospheric mixing ratio (measured by the GV), τ_t is its chemical lifetime in the troposphere, and t_t is the transit time to the

tropical upper troposphere. This assumption for χ_{TTL} is appropriate for atmospheric constituents that are emitted in midlatitudes and transported to the tropical upper troposphere. It may be inappropriate for species with primary sources that are oceanic and/or tropical (e.g., bromoform and methyl nitrate). Modeling studies suggest, however, that concentrations of these species over the tropical Pacific and Continental United States may be comparable [e.g., 92].

The complete solution is then

$$\frac{\chi(t_s)}{\chi_t} = \left(e^{-\frac{1}{\tau_t}t_t}\right)e^{-(\frac{1}{\tau_s}+\frac{1}{\tau_m})t_s} + \frac{\chi_s}{\chi_t(\frac{\tau_m}{\tau_s}+1)}\left(1 - e^{-(\frac{1}{\tau_s}+\frac{1}{\tau_m})t_s}\right) \tag{3.4}$$

which is written here in terms of the ratio of the mixing ratio of the trace gas remaining in the air mass to its initial mixing ratio in the mid-latitude troposphere. In this system, $\chi(t_s)$, χ_t, χ_s, τ_t, τ_s, and t_s are known. The mixing time τ_m and tropospheric transit time t_t are unknown. We estimate τ_m and t_t by computing $\chi(t_s)/\chi_t$ for multiple species and fitting a curve of the form in (3.4) as a function of chemical lifetime τ_s and τ_t. We use the nonlinear curve-fitting routine MPFIT in IDL to find τ_m and t_t [93]. We also estimate the sensitivity of τ_m to uncertainties in t_t.

For plotting purposes only, in order to display the fit of the box model as a function of a single parameter, we assume a simple relationship between the tropospheric and stratospheric lifetimes. The Arrhenius equation represents the temperature dependence of the rate constant, k, of a chemical reaction as

$$k = Ae^{\frac{-E_a}{RT}} \tag{3.5}$$

where A is the pre-exponential factor, E_a is the activation energy, R is the gas constant, and T is temperature. The lifetime, τ, of a given compound is then related to the rate constant k by $\tau = 1/(k[\text{C}])$, where $[\text{C}]$ is the concentration of the reac-

tant (e.g., oxidation by OH). For a single reaction, the tropospheric and stratospheric lifetimes can then be related using the relationship between τ, k, and the Arrhenius equation by

$$\tau_t = e^{ln(\tau_s)\frac{T_s}{T_t}} \tag{3.6}$$

where τ_t is the tropospheric lifetime, τ_s is the stratospheric lifetime, T_s is the stratospheric temperature, and T_t is the tropospheric temperature. For our analysis we use $T_s = 223$ K and $T_t = 253$ K. This is a reasonable assumption for species that undergo loss predominantly through oxidation processes but would not apply to species whose losses are dominated by photodissociation.

B.   Rossby Wavebreaking

1.   Tropical Boundary Definition

Because the goal of this study is to characterize Rossby wavebreaking and isentropic transport above the subtropical jet between the tropical UTLS and the extratropical LS, an appropriate definition of the boundary between the tropics and extratropics is required. In this study, we use the lapse-rate tropopause to define the tropical boundary. The tropopause is found at high altitudes in the tropics (15–17 km) and at low altitudes in the extratropics (<12 km), as is evidenced by a clear bimodal frequency distribution in previous studies [e.g., 94, 95]. The transition between these two modes takes place near the subtropical jet, often within a narrow latitude range and consequently, is referred to as the "tropopause break" [e.g., 96, 97]. We use the location of the break as the instantaneous boundary between the tropical tropospheric air on the equatorward side of the jet and extratropical stratospheric air on the poleward side of the jet. Figure 3 is a schematic of the tropopause structure. The figure also shows

the frequency distribution of the pressure altitude of the tropopause from the ERA-Interim reanalysis. This distribution is bimodal with a distinct minimum between tropical and extratropical tropopause altitudes is near 13 km in this distribution. For this analysis, we identify the tropopause break in each hemisphere as the location of the 13 km tropopause altitude contour that extents completely around the globe (360 degrees of longitude). Because the tropopause is uniformly higher that 13 km in the deep tropics and lower than 13 km in high latitudes, this contour is guaranteed to exist. The latitude of the contour can vary significantly for a given analysis time.

An example of the observed sharpness of the troposphere-stratosphere transition across the tropopause break is given in Figure 4. Figure 4a shows conventional Eulerian zonal mean meteorological fields from the ERA-Interim reanalysis at 00 UTC on 1 May 2008. Figure 4b shows the same analysis variables in a coordinate system that is averaged relative to the tropopause in altitude and relative to the tropopause break in latitude (the 13 km altitude contour) [e.g., 79]. Red contours of potential temperature in each section show the bounds of the wavebreaking layer analyzed in this study (350–500 K). The small-scale undulations in potential temperature and PV contours seen within the gray vertical lines in Figure 4b are artifacts resulting from relative-altitude calculations in the region where the altitude of the tropopause is highly variable (within 1 grid point of the tropopause break). Regardless, this tropopause-relative zonal mean view illustrates the sharpness of the horizontal boundary between troposphere and stratosphere along the subtropical jet which, due to significant latitudinal variation of the tropopause break, is not observed in a simple zonal mean. A large portion of the potential temperature layer analyzed in this study, typically upwards of 380 K, is often above the tropical tropopause. For this analysis, we assume that the boundary between the tropical and extratropical stratosphere at levels above 380 K lies at the same location as the tropopause break.

This may not be accurate at all analysis times, but analyses of the location of the maximum meridional PV gradient show that it coincides with the tropopause break in the 350–370 K potential temperature range and extends into the LS [e.g. 98]. This suggests that the tropopause break is also an appropriate boundary in the LS.

The jump in the lapse-rate tropopause at the subtropical jet provides a natural boundary between the tropics and extratropics in the layer above the jet, but lapse-rate tropopause altitude is not a conserved quantity. Therefore, we calculate climatological values of potential vorticity (PV) along the 13 km tropopause height contour to identify a PV value that best represents the location of the tropopause break. Figure 5a shows the annual-mean PV along the tropopause break as a function of altitude (solid line). The dashed lines indicate the annual range of the climatological monthly-mean values. Note the natural increase of PV as the static stability increases with altitude. At all altitudes and in both hemispheres, the annual range of PV along the tropopause break is small ($\pm$0.5–1.5 pvu). Previous studies have used PV values near ± 2 pvu as a tropical boundary for wavebreaking identification in the 350–370 K potential temperature range. PV in the same layer at the tropopause break observed here is near ± 4 pvu, while ± 2 pvu is found deeper into the tropics (see also Figure 4b). These differences in the location of the tropical boundary may have significant impacts on estimates of the direction and magnitude of transport.

Figure 5b shows the annual-mean and annual range of climatological monthly-mean equivalent latitude along the tropopause break. Equivalent latitude is a quasi-conservative PV-based meridional coordinate that effectively removes zonal variability due to large-scale waves. For a given PV value q_0, the equivalent latitude ϕ_e is defined as the latitude of the boundary of a polar cap whose area is equal to the area of all locations with $q > q_0$. There is a one-to-one correspondence between PV and equivalent latitude. In physical terms, equivalent latitude tells you the latitude that

an air parcel would have if all the parcels on an isentropic surface were rearranged to be zonally symmetric and to have PV monotonic in latitude. Because magnitudes of PV increase rapidly with altitude above the subtropical jet, we instead use equivalent latitude at the tropopause break for our analysis to achieve consistency at all vertical levels.

2. Wavebreaking Identification

Once an appropriate PV value for the tropical boundary has been chosen, Figure 6 illustrates the necessary steps to identify a continuous boundary and to characterize wavebreaking events. We identify Rossby wavebreaking events using a method similar to that outlined in [20]. For a given potential temperature surface, wavebreaking exists at a particular longitude if there is a significant reversal in the meridional gradient of potential vorticity (PV) or equivalent latitude. In order to require that gradient reversals involve deep tropical and extratropical air masses, [20] consider a reversal of at least ± 0.5 pvu relative to the PV boundary used as evidence of Rossby wavebreaking. Comparisons with the PV reversal criteria in [20] at 350 K suggest that an equivalent latitude reversal of ± 2.5 degrees relative to the boundary is comparable. Figure 5b shows that the annual cycle of equivalent latitude at the tropopause break is large (10–15 degrees) due to the seasonality of the meridional location of the subtropical jet and tropopause break. To account for the annual cycle of equivalent latitude at the tropopause break, we use climatological monthly-mean values of ϕ_e to define the contours used for wavebreaking analysis.

Figure 6a illustrates the identification of a continuous tropical boundary for identifying gradient reversals (folds). At any given analysis time, there may be cut-off regions of tropical air masses within the extratropical reservoir (or vice versa). These cut-offs may be residual evidence of previous wavebreaking events. In order to iden-

tify active Rossby wavebreaking events between tropical and extratropical air masses and ignore cut-off regions, we first isolate global contours of equivalent latitude in each hemisphere using the library function CONTOUR in Interactive Data Language. Each global contour is subsequently searched for regions of meridional folding. Following [20], if the meridional gradient reversal criteria within a folded region is satisfied for at least 10 degrees of consecutive longitude, the fold is tagged as a Rossby wavebreaking region. This 10 degree longitude threshold is used to ignore folds that result from processes that take place at scales much smaller than Rossby waves. For analysis, we store the magnitude of the gradient reversal at each longitude, the contour segments of the equatorward and poleward boundaries of the folded region, and the areas of the tropical and extratropical air masses.

Figure 6b illustrates the classification of wavebreaking evolution: anticyclonic or cyclonic. In previous studies, anticyclonically and cyclonically sheared breaking waves have been separated by the local downstream longitudinal PV gradient and/or the meridional component of the wave activity flux [e.g., 99, 26, 27]. In this study, we separate anticyclonic and cyclonic wavebreaking by the direction of the meridional fold in each global equivalent latitude contour. Contour paths, in the absence of folding, are analyzed from west to east. Analyzing contours in the eastward direction allows anticyclonically sheared breaking waves to be characterized by pole-to-equator contour folding while cyclonically sheared breaking waves are characterized by equator-to-pole contour folding. In the example in Figure 6b, an anticyclonically sheared breaking wave is identified over the west Pacific and a cyclonically sheared breaking wave is identified over the east Pacific.

Following identification at each analysis time, instantaneous wavebreaking signatures are objectively linked with succeeding times to identify full wavebreaking lifecycles. We consider wavebreaking events to be those that are identified for at least

3 consecutive analysis times (18 hours) and: 1) If anticyclonic, have a minimum east-ward propagation of 1.5 degrees and a maximum eastward propagation of 15 degrees and 2) If cyclonic, have a maximum zonal propagation in either direction of 15 degrees. Subjective analyses suggest that requiring a minimum wavebreaking lifecycle is necessary to avoid the identification of small, short-lived folds in the dynamical boundary that do not exhibit characteristics consistent with Rossby wavebreaking. Minimum propagation distances are used for anticyclonic wavebreaking events to avoid over-identification of stationary dynamical features such as monsoon circulations. Maximum propagation distances between analysis times are used to correctly associate regional wavebreaking signatures between analysis times. Once grouped, wavebreaking event lifecycles are used for characterization and transport analyses.

We identify transport for each Rossby wavebreaking event using forward trajectories initialized in the tropical and extratropical air masses of the identified fold (red and blue particles in Fig. 6c). At the final analysis time of each event, particles are initialized at a longitude-latitude resolution of 0.5 degrees and isentropically advected forward 10 days. If particles in the tropical (extratropical) air mass gain (lose) 5 degrees of equivalent latitude and are within regions of extratropical (tropical) tropopause heights ($<(>)$13 km) 10 days downstream, they are considered to be irreversibly transported (mixed). Although this transport threshold is sensitive to the choice of equivalent latitude change, inspection of many events suggests that a 10-day equivalent latitude change of 5 degrees is appropriate for the ERA-Interim dataset. It is important to note that such a threshold identifies events that are transported a significant distance from their original reservoirs. The net transport from this analysis may differ from the net local stirring along the jet due to small changes in PV or equivalent latitude for a given particle. In addition, previous studies have shown that transport and mixing for a given event using contour advection techniques

generally takes place within the first 7 days of it's lifecycle [e.g., 37]. For that reason, the transport estimates presented in this analysis are expected to be comparable to those from previous studies.

C.   Stratospheric Intrusion Interpolation

During RF06 the observed stratospheric intrusion moved rapidly between the available 6-hourly GFS analyses, although the shape of the intrusion did not change much. For example, between the 1 May 2008 18 UTC and 2 May 2008 00 UTC analyses, the tropopause fold moved a distance about equal to the size (or width) of the fold itself. As a result, if simple space-time interpolation is used, the size and magnitude of the fold are underestimated. To provide a more accurate interpolation, we assume that the fold is moving at a constant velocity between analyses, which we estimate subjectively by examination of the two GFS analyses. Interpolating in this moving reference appears to give a more realistic estimate of the structure of the fold. Varying the direction chosen for the moving reference frame by up to ± 20 degrees does not significantly change the results. The tropopause fold observed during RF12 was not moving as quickly as the one sampled during RF06, so simple linear interpolation of the GFS analyses in space and time is used.

CHAPTER IV

RESULTS

A.   Tropospheric Intrusions

1.   Research Flight 1

Research Flight 1 (RF01) took place 18 April 2008 and targeted a large mass of tropospheric air that intruded into the stratosphere ∼5–8 days earlier. The intrusion is associated with a large-amplitude Rossby wavebreaking event over the western Pacific that occurred from 11 to 16 April. Figure 7 shows potential vorticity (PV) on the 380 K isentropic surface from the GFS analysis at 24 h intervals, illustrating the evolution of the tropospheric intrusion. In Figure 7 the division between red and blue colors is located at 6 pvu, which is representative of the boundary between tropical upper troposphere air and midlatitude lower stratosphere air at 380 K during this time period. On 11 April the incipient intrusion can be seen just east of Japan (Figure 7a). The intrusion becomes more deformed and stretches farther north until it breaks off from the tropical reservoir around 15 April (Figure 7e). This evolution is consistent with the characteristics of a blocking anticyclone [e.g., 100].

Figure 8a shows the 380 K PV field at 18 UTC on 18 April and the flight track taken by the GV aircraft. To focus on the core of the intrusion, which has the lowest PV values, in this figure the red-blue division is located at 4 pvu. Figure 8b shows the flight track and PV estimated from a 5 day reverse-domain-filling (RDF) back-trajectory calculation from the analysis time in Figure 8a [101]. The similarity of the analyzed PV and the RDF calculation indicates that the PV in the intrusion was largely conserved between the time it intruded into the stratosphere and when it was sampled by the GV.

Figure 9 shows atmospheric parameters from the GFS analysis along a curtain that follows the GV flight track. The intrusion can be seen as air near the 380 K level with lower static stability (lighter colors) and lower values of PV (2–4 pvu), which lies ∼3 km above the tropopause. This intrusion of low-stability air may contribute to the stratospheric stability minimum often found above the tropopause inversion layer (TIL), which is defined as the stability maximum within 2–3 km above the tropopause [e.g., 102, 103, 104, 96]. The tropospheric intrusion was sampled multiple times during the first half of the flight along the flight segments labeled 1, 2, and 3. Another stability minimum is observed in the second half of the flight (∼1945–2045 UTC), but this is related to a strong cyclone over the central U.S., not a tropospheric intrusion [e.g., 105, 106, 107, 81]. The flight segment labeled 4 sampled air outside the intrusion in the background stratosphere near the 380 K isentropic surface. These four segments are also labeled along the flight track in Fig. 8a.

For a different view of the evolution of the intrusion, we examine back trajectories of air parcels from the core of the intrusion. Panels on the left in Figure 5 show maps of the locations of ∼200 parcels that have $|PV| < 4$ pvu at both the analysis time for RF01 and 15 days earlier. The panels on the right in Figure 10 are vertical sections through the group of parcels. The locations of the vertical sections were chosen subjectively and are shown by the thick black line on each map. The parcels colored red in Figure 10 are those located within 1° of the vertical section at each analysis time. Parcels located more than 1° from each vertical section are shown on the maps in blue, but are omitted from the vertical section plots for clarity. Because of this selection criterion, the particular parcels colored red and blue are different at each time. In the atmospheric sections, the tropopause altitudes (orange) are calculated by applying the WMO tropopause algorithm to the GFS pressure grid [80]. These tropopause altitudes are consistent with the GFS model output tropopause except in

cases of misidentification by the model algorithm near the subtropical jet [81]. All other variables are from the GFS analysis. On 11 April (Figure 10a), eight days before the intrusion was sampled, back trajectories show that the parcels are predominantly in a filament in the tropical upper troposphere that stretches westward from the western Pacific where the Rossby wavebreaking event is beginning (see Figure 7). A few parcels are located above the tropopause. On 12 April (Figure 10b), twenty-four hours later, the air mass has moved north into the region of the tropopause break, identified by the overlapping (double) tropical and extratropical tropopauses, along the edge of the subtropical jet stream [e.g., 108, 109, 96]. By 13 April (Figure 10c) the air mass has moved through the break and into the midlatitude lower stratosphere, where it remains until observed on 18 April. The air mass reaches its highest latitude in the midlatitude lower stratosphere on 15 April (Figure 10d) and then moves east and somewhat south. At the time the aircraft sampled the tropospheric intrusion, trajectory calculations show that it was completely separated from its tropical source by a strong subtropical jet and the air had been in the lower stratosphere for $\sim$7 days.

Observations of long-lived trace species made by the GV provide additional insight into the evolution of the intrusion. Figure 11a is a scatterplot of all O_3-CO observations during the flight. The relationship between O_3 and CO can be used to identify the stratosphere, troposphere and extratropical transition layer [e.g., 110, 111, 41]. Observations during the four horizontal flight segments labeled in Figure 9 are colored by PV to illustrate their relationship to the observed dynamics. Air with low PV ($<$ 5.5 pvu, red) has the strongest tropospheric characteristics, with CO mixing ratios of $\sim$40–60 ppbv (double that of the background stratosphere sampled) and O_3 mixing ratios of $\sim$100–200 ppbv. This air is not typical of the free troposphere, which has higher CO, but it has much lower O_3 than typical stratospheric air. In previous studies, the lower bound of the stratospheric branch is $\sim$200–300 ppb O_3

and $\sim$30–40 ppb CO [e.g., 41]. Although this low PV air is not characteristic of the free troposphere, it suggests that the primary origin is in the tropical upper troposphere. Annual mean concentrations of CO in the tropical upper troposphere and lower stratosphere (the tropical tropopause layer or TTL) are 80–90 ppbv and $\sim$40 ppbv, respectively [e.g., 112, 113]. Air near the boundary of the intrusion (6 pvu from Figure 7) is shown in black and is also found in the lower half of the stratospheric branch, with significantly higher O_3 and lower CO than the low PV air. Air with high PV (> 6.5 pvu, blue) represents the normal stratospheric branch of the O_3-CO scatterplot. This comparison gives chemical evidence of air in the lower stratosphere with significant tropospheric influence and agrees with the observed PV fields. This relationship is in agreement with that illustrated in [10].

AWAS data are used to estimate the mixing timescale of the observed intrusion by fitting the model described in Chapter IIIA to the measurements. The trajectories for RF01 give an approximate stratospheric transit time t_s of 1 week. Figure 12a shows the ratio of mean trace gas concentrations in the intrusion to mean tropospheric concentrations for several species, $\chi(t_s)/\chi_t$, as a function of stratospheric lifetime τ_s for RF01 (black dots). A list of the trace species used is given in Table I. The values of the model fitted to these ratios by simultaneously varying the two unknown parameters t_t (the tropospheric transit time) and τ_m (the mixing time) are shown by black diamonds. The solid line is the model fit following our assumed relationship between stratospheric and tropospheric lifetimes using the Arrhenius equation (see Chapter IIIA). Table II gives the number of observations used in this analysis and the fitted parameters. For RF01, there are 9 AWAS samples in the intrusion and 8 in the troposphere. The values for t_t and τ_m given by the fit are 0.38 weeks and 0.73 weeks, respectively. The fit is not sensitive to the value of t_t. If t_t is varied by ± 1 week (long/short dashed lines in Figure 12a), τ_m changes by less than a day

(Table II). This insensitivity arises because the longer-lived species, which have a strong influence on the shape of the curve, do not undergo significant losses between their source regions and the tropical upper troposphere. The low sensitivity of τ_m to changes in t_t is a direct result of this relationship and thus the exact value of t_t is not important for our analysis. On the other hand, varying τ_m while holding t_t fixed causes significant changes to the fit. Increasing or decreasing τ_m by a factor of 2 gives the gray envelope in Fig. 12a. This indicates that the data constrain τ_m well for RF01.

2. Research Flight 14

Research Flight 14 (RF14) took place 18 June 2008 and targeted a mass of tropospheric air that intruded into the stratosphere $\sim$4–6 days prior. Unlike RF01, the tropospheric intrusion sampled during RF14 is associated with a slow northward migrating jet in the tropical east Pacific. As discussed briefly in Chapter I, a persistent westerly jet is observed in this region, particularly during northern hemisphere winter and spring. Rossby waves propagate equatorward in the westerlies and break, providing a transport route to midlatitudes. As the jet migrates north, air in the tropical upper troposphere and lower stratosphere above and north of the jet is transported across the tropopause into the midlatitude stratosphere. Figure 13 shows PV on the 390 K isentropic surface from the GFS analysis at 48 h intervals, illustrating the evolution of the observed intrusion. In Figure 13, the division between red and blue colors is located at 4 pvu, which is representative of the boundary between tropical upper troposphere air and midlatitude lower stratosphere air at 390 K during this time period. It should be noted that the 390 K isentropic surface is frequently very near or above the tropopause in the tropics and some of the low PV air shown may be in the lower stratosphere [e.g., 114]. On 12 June the intrusion can be seen north of

Hawaii between 200° and 225° longitude (Figure 13a). Two days later on 14 June the air mass moves farther north and slightly to the east (Figure 13b). By 16 June the air mass separates from the source of tropical air and moves just north of 30°N latitude (Figure 13c). The air mass then moves north and east with the midlatitude westerlies to the northwestern U.S. by 18 June (Figure 13d, centered near 235° longitude and 50°N latitude).

Following our methods in section 1 for RF01, we select horizontal flight segments during RF14 that sampled intrusion air and the stratospheric background for chemical analysis. The atmospheric parameters along a curtain following the flight track for RF14 (not shown) are comparable to those seen for RF01 (Figure 9). The low static stability and PV fields in this case are centered at about 390 K ($\sim$3 km above the tropopause). The GV sampled the tropospheric intrusion during two flight segments. The background stratosphere was not measured at 390 K during the flight, so we use one flight segment near 370 K to represent the background stratosphere.

Figure 14 shows maps of parcel locations and vertical sections for parcels from the core of the intrusion. On 11 June (Figure 14a), nearly 8 days before the intrusion was sampled, back-trajectories show that the parcels are above and north of the tropical westerly jet in the east Pacific and near the tropopause break in the tropical upper troposphere. By 15 June (Figure 14c) the jet moves north to $\sim$20°N latitude and the air mass is in the lower stratosphere. Over the next 4 days the air mass moves north and east with the midlatitude westerly flow. During this time the westerlies at midlatitudes weaken considerably (Figures 14c and 14d), allowing the air mass to be transported north of the subtropical jet where it was sampled with the GV (Figure 14e). At the time the aircraft sampled the tropospheric intrusion, the air had been in the lower stratosphere for $\sim$5 days.

Figure 11b is a scatterplot of O_3 and CO observations during RF14. Observations

along flight segments in the intrusion and background stratosphere are again colored by PV (as in Figure 11a). The low PV air ($<$ 5.5 pvu, red) is again at the lower O_3 bound of the stratospheric branch and has the highest CO concentrations of the branch. Again, this air is not characteristic of the free troposphere, but the elevated CO concentrations and low O_3 (compared to the stratospheric background) suggest a significant tropospheric influence.

Results from fitting the box model to the AWAS data are shown in Figure 12b. Trajectories for RF14 give an approximate stratospheric transit time t_{strat} of 0.75 weeks for our model. The relationship between the observations and model is similar to the fit for RF01 (Figure 12a). If the tropospheric transit time t_t is varied $\pm$ 1 week, the mixing time τ_m also changes $\pm \sim$**1** day in this case (see Table II), again suggesting that τ_m has low sensitivity to changes in t_t. The data also constrain τ_m well for RF14. In this case the mixing time given by the model is 0.84 weeks ($\sim$6 days), slightly longer than in RF01. The variability in τ_m for changes in t_t is slightly, but not significantly, higher for RF14.

3.   Research Flights 7, 9 and 10

During START08 the GV aircraft observed many small-scale features in the stratosphere with tropospheric chemical characteristics. These features suggest that irreversible transport by tropospheric intrusions is important for lower stratospheric composition. Three research flights observed air with these characteristics in the 370–400 K potential temperature range at latitudes 10°–15° north of the subtropical jet (RF07, RF09, & RF10). Unlike the large-scale tropospheric intrusions sampled in RF01 and RF14, there are no obvious features with low stability or low PV in the GFS analyses at the locations where these small-scale chemical variations are observed (not shown). All of the observed features are found $\sim$3–5 km above the

tropopause and in regions of PV $\geq$ 8 pvu and static stability $\geq$ 14 K/km for each flight.

Figures 15a, 15b and 15c show measurements of O_3, CO, and ethyne for RF07, RF09, and RF10, respectively. For each time series, the small-scale features with tropospheric characteristics can be seen in significantly decreased O_3 (300–600 ppb lower than the background stratosphere) and increased CO (10–20 ppbv higher than the background stratosphere). The relevant flight segments are identified by a gray background. The features can also be seen in short-lived tropospheric trace species such as ethyne, which has a lifetime of 3 weeks. In RF07 and RF10 the small-scale features have nearly double the concentration of ethyne compared to the surrounding stratospheric air. The feature observed in RF09 cannot be contrasted with the surrounding air because there is only one AWAS sample during the interval shown. The timeline for RF10 (Figure 15c) ends at the point where the aircraft descended to a lower altitude.

To test whether these small-scale features are produced by stretching and folding by the large-scale resolved flow, we compute 10 day reverse-domain-filled (RDF) maps of equivalent latitude on a high-resolution 0.1° x 0.1° grid for flights RF07, RF09, and RF10 at the hour nearest in time to when the small-scale features are sampled by the aircraft. Trajectory methods like RDF can often provide detailed information about transport and stirring that Eulerian analyses cannot [e.g., 101]. Figures 16a and b show RDF maps of equivalent latitude on isentropic surfaces near the level where the air with tropospheric characteristics is observed during flights RF07 and RF10, respectively. The measured CO along the flight track is plotted in green or yellow during times when the aircraft potential temperature is within 5 K of the isentropic surface shown. The narrow gray lines indicate when the aircraft was flying at other altitudes. For both flights elevated levels of CO (>30 ppbv, green) coincide

well with filaments of air that has been transported from tropical/subtropical regions, indicated by their low equivalent latitudes of origin ($\leq 30°$, red colors). Additionally, background stratospheric levels of CO (<30 ppbv, yellow) are found in air with middle and high equivalent latitudes of origin ($> 30°$, blue colors).

It is not surprising that the global analyses fail to resolve these rather small-scale features. The RDF analysis shows that they are remnants of intrusions that started more than a week prior to when they were sampled by the GV. Although these features are no longer recognizable in large-scale Eulerian fields, the source air masses are easily identifiable in the in situ measurements from the aircraft and in Lagrangian studies driven by the large-scale winds [e.g., 86].

4. Global Intrusion Analysis

The following results give a subjective global analysis of tropospheric intrusions in the 370–400 K potential temperature range for the START08 experiment period (April–June 2008) using the GFS analyses. At each model analysis time parcels are initialized on a $0.5° \times 0.5° \times 10$ K potential temperature grid over the Northern Hemisphere and run backward for 10 days. Using 5 and 10 day RDF maps of equivalent latitude, tropospheric intrusions are manually identified as air masses with equivalent latitude of origin $\leq 30°$ that are entirely detached from the tropical reservoir and are advected poleward from the reservoir in the period following detachment. During the analysis period 19 tropospheric intrusions can be identified using the aforementioned guidelines. All 19 events are associated with Rossby wavebreaking in one of the forms discussed in Chapter I. The events vary spatially in size and typically intrude and detach within ~ 3 days. The intrusion sampled during RF01 is one of the largest events observed.

Figure 17a is an example that shows 10 day RDF equivalent latitude on the 380

K isentropic surface for an intrusion that resulted from large-amplitude Rossby wave-breaking in the central Pacific. The intrusion air mass and source Rossby wavebreaking event are identified by arrows in the map. Following the analysis time shown, the intrusion and source air masses separate as the source air mass collapses back into the tropical reservoir. Additionally, some of the stratospheric air seen here in the tropics (blue colors in the east Pacific) is mixed in with the tropical reservoir after the breaking event collapses [e.g., 18]. We find that the events can be divided into three tropical source regions: the west/central Pacific (120°–200° longitude), the east Pacific (200°–260° longitude) and the Atlantic (280°–340° longitude). The west/central Pacific and Atlantic regions are associated with high-frequency Rossby wavebreaking at 350 K in previous studies (see Chapter I). The east Pacific region encapsulates the strongest portion of the Pacific westerly duct (see Figure 1) that, when coupled with equatorward Rossby wavebreaking, can provide transport pathways to higher latitudes (see Chapter I). Figure 17b shows the source regions and the number of intrusion events observed in our analysis. The most active region for tropospheric intrusions during the START08 period is the west/central Pacific, with 11 intrusions observed during the 91 analysis days (a frequency of ∼1 per week). In the eastern Pacific region, 7 intrusions are observed during the time period (a frequency of ∼1 every 2 weeks). Only 1 tropospheric intrusion has its source air mass from Rossby wavebreaking over the Atlantic region in our analysis.

Tropospheric intrusion events over the west/central Pacific and east Pacific regions have very different character during the time period. In the west/central Pacific intrusions typically resemble the one sampled by RF01 (see Figure 7). In the east Pacific, the intrusion events are all similar to that in RF14 (see Figure 13), with slow evolution dominated by meridional transport. These different characteristics can be related to the different Rossby wavebreaking regimes discussed in Chapter I. Rossby

wavebreaking along the subtropical jet stream and north of the westerly ducts typically occurs in zonal flow. When Rossby waves propagate equatorward and break within the westerly ducts, however, the zonal component is in the deep tropics and intrusions are transported primarily in the meridional direction. These evolutionary differences have been classified before by [25] as type 1 (tilts downstream, broadens, wraps up anticyclonically) and type 2 (tilts upstream, thins, advected cyclonically) poleward breaking events. It is evident from our analysis that large-amplitude Rossby wavebreaking events are predominantly type 1 and Rossby wavebreaking in the westerly ducts, type 2. It should also be noted that previous studies suggest that the west/central Pacific and Atlantic regions should be comparable in Rossby wavebreaking frequency, at least at 350 K. However, 2008 was predominantly an ENSO cold phase (La Niña) year which could explain the observed frequency of tropospheric intrusions in the east Pacific and Atlantic regions.

B.   Rossby Wavebreaking Characteristics

The Rossby wavebreaking identification techniques described in detail in Chapter III2 were applied to 30 years of ERA-Interim reanalyses (1981–2010). The number of events identified as a function of the 9 potential temperature levels analyzed (350–500 K) is given in Figure 18. The fewest number of Rossby wavebreaking events are found at the lowest potential temperature levels (350–360 K, near the core of the subtropical jet) and increase with altitude up to a pronounced maximum at 420 K. The general behavior is consistent across hemispheres and wavebreaking evolution (cyclonic or anticyclonic). There are more anticyclonically sheared wavebreaking events than cyclonic events at all altitudes. Anticyclonic events are most prevalent in the southern hemisphere, while cyclonic events are most prevalent in the northern hemisphere. In

addition, cyclonically sheared wavebreaking events are nearly absent at the lowest altitudes (< 1 per month in each hemisphere), increase by an order of magnitude with increasing altitude from 360 to 420 K and subsequently decrease aloft, largely contributing to the observed peak at 420 K. Anticyclonic events increase rapidly from 360 to 380 K, but show comparable frequencies with increasing altitude above 380 K. Although not shown, annual cycles of wavebreaking frequency in the 350–400 K potential temperature range are comparable to results from previous studies at 350 K, which show a strong peak in the summer of each hemisphere [e.g., 20]. There is no observed annual cycle at 420 K in this analysis, while the annual cycle becomes strong again at 500 K, but is shifted 6 months relative to the lower altitudes (a winter peak). This behavior at 500 K is consistent with the occurrence of mean easterly winds at this level during summer which inhibit Rossby wave propagation altogether.

Net annual Rossby wavebreaking transport estimates from trajectory calculations of each event as a function of potential temperature are shown for each hemisphere in Figure 19. Transport magnitudes are shown as the percentage of the area of one hemisphere with error bars (±1 standard deviation) illustrating the inter-annual variability. Negative values represent net transport into the tropics and positive values, into the extratropics. The remaining discussion will refer to transport into the tropics as equatorward and transport into the extratropics as poleward. For both hemispheres, net transport is poleward except from 370–390 K in the northern hemisphere and 380–390 K in the southern hemisphere. Net poleward transport aloft is comparable to previous studies at 500 K [e.g., 36]. Poleward transport below 370 K, however, is in disagreement with previous studies of isentropic transport. The observed transport characteristics here and geographical distributions discussed in further detail below show that potential temperature levels can be grouped by similarity into 4 distinct layers: 350–360 K, 370–400 K, 420 K, and 450–500 K. The

remaining analyses will focus on 4 representative levels from these layers: 350 K (near the core of the subtropical jet and a focus of many previous studies), 380 K (coincident with previous tropospheric intrusion analyses), 420 K (the observed peak in cyclonic wavebreaking events from Figure 18), and 500 K (a level well into the tropical and extratropical stratosphere and near the altitude of the winter polar vortices).

Figure 20 shows annual cycles of transport for both hemispheres by wavebreaking evolution and transport direction at 350 K, 380 K, 420 K, and 500 K. As in Figure 19, negative net transport represents equatorward transport and positive net transport, poleward. At 350, 380 and 500 K, anticyclonic wavebreaking accounts for a majority of the transport in both directions, consistent with the observed wavebreaking frequency in Figure 18. The annual cycles of poleward transport at 350 K and 380 K show a fall maxima in both hemispheres, while equatorward transport reaches a maximum during each hemisphere's summer. There is little annual cycle in either transport direction at 420 K. The net transport at 420 K in the northern hemisphere, however, shows a weak annual cycle and spring maximum. At 500 K, the annual cycles for both transport directions reach a maximum in hemisphere winter and spring, in agreement with the analysis of [36]. The transport magnitudes observed at 500 K in this analysis also agree with [36], with the exception of the observed winter peak which is roughly twice the previously observed magnitude. The net transport at 380 K in both hemispheres is dominated by the summer peak in extratropics-to-tropics transport, which shows the largest monthly transport magnitudes of any potential temperature level (20–30 % of a hemisphere). It is important to note that the near zero transport observed in both directions during winter at 350 K is likely due to our definition of transport in Chapter IIIB2, which identifies only deep transport events ($\geq$5 degree along trajectory 10-day equivalent latitude change). There are wavebreaking events observed throughout the entire year at all levels, but transport and mixing

is confined to a narrow region along the troposphere-stratosphere boundary during the annual minimum in wavebreaking frequency. Differences in seasonal and annual transport magnitudes between this study and previous studies may in part be a result of this definition.

As discussed in Chapter III2, PV at the tropopause break from the ERA-Interim reanalysis is near ± 4 pvu in the 350–370 K potential temperature range while the commonly used ± 2 pvu contour for troposphere-stratosphere separation in previous studies is deeper into the tropics. To test the dependence of transport magnitude and direction on the analyzed dynamical wavebreaking contour, the same analysis techniques used for dynamical contours at the tropopause break are applied at 350 K using the ± 2 pvu contour of PV. Figure 21 shows the observed annual cycle of transport by hemisphere, wavebreaking evolution and transport direction. For both hemispheres, the net annual cycle of transport is now primarily equatorward (into the troposphere), in agreement with previous studies. This analysis illustrates that the choice of troposphere-stratosphere boundary has a significant impact on the observed direction and magnitude of transport. The number of events identified along the ± 2 pvu PV contour was slightly lower than that at the tropopause break.

To address the questions raised in Chapter I on the dependence of transport direction on the characteristics of the mean flow, we aim to identify any possible modes of transport observed for the identified wavebreaking events. Figure 22 shows frequency distributions of events as a function of their associated equatorward and poleward transport area for wavebreaking events at the four levels. These distributions show that, for all levels, most transport events are relatively small (< 0.5 % of a hemisphere in either direction) and smoothly vary with increasing scale (i.e., there are no distinct transport modes). If, instead, frequency distributions are shown as a function of the fraction of tropical and extratropical air mass area transported pole-

ward or equatorward for each event, three distinct modes of transport are observed. Figure 23 shows these distributions. For anticyclonic events at 380 K, all three modes (frequency maxima) are observed at comparable frequencies and are identified by the gray arrows. A mode of predominately poleward transport is evidenced by transport fractions of > 70 % of the tropical air mass and < 15 % of the extratropical air mass. Similarly, a mode of predominately equatorward transport is evidenced by transport fractions of < 15 % of the tropical air mass and > 70 % of the extratropical air mass. Thirdly, a mode of comparable transport in both directions (bidirectional) is evidenced by transport fractions of 30 % to 50 % in each direction. The three frequency maxima are also observed at 420 K, but the equatorward mode is largely diminished. The equatorward transport mode is not observed for the anticyclonic distributions at 350 K or 500 K. For cyclonically sheared wavebreaking events, only one mode of transport is observed: poleward. It is important to note here that the distributions from Figures 22 and 23 are not separated by hemisphere because there is little difference between the hemispheres.

Following the identification of three transport modes in Figure 23b, composite mean dynamical fields from the ERA-Interim reanalysis at the last identified time in each wavebreaking event lifecycle are computed. Figure 24 shows composite mean equivalent latitude, wind speed and direction, and tropopause height of anticyclonic events at 380 K for each hemisphere and poleward, equatorward and bidirectional transport modes. The number of events contributing to and the mean latitude of these composites are given in Table III. For the poleward transport mode (Figure 24a), the mean flow shows characteristics similar to that proposed in the Introduction: a "split jet" where the subtropical jet on the upstream side of the breaking wave extends poleward and meridionally overlaps the equatorward subtropical jet downstream. In the northern hemisphere, this split jet feature is clearly observed with large

meridional overlap (~45 degrees). Although there is also evidence of distinct jet axes poleward and equatorward of the wavebreaking region in the southern hemisphere, the jet axis poleward stretches over the entire domain while the equatorward jet axis extends from the western edge of the wavebreaking signature (~15 degrees upstream) to ~35 degrees downstream, approaching the latitude of the poleward subtropical jet. For the equatorward transport mode (Figure 24b), there is no evidence of a split subtropical jet in either hemisphere. There is, however, a weakening of the subtropical jet immediately downstream of the breaking wave and a strong anticyclonic circulation upstream in the tropical reservoir of the northern hemisphere. In the southern hemisphere, there is also a slight weakening of the subtropical jet downstream of the breaking wave, evidenced by uncertainty in the location of the jet axis there. In addition, there is a much weaker anticyclonic circulation observed in the tropical reservoir upstream that is not clearly observed at the scale shown. For the bidirectional transport mode (Figure 24c), the mean flow shows characteristics consistent with features of both directional modes, but with a nearly uniform subtropical jet. The largest differences between hemispheres are observed downstream of the breaking wave, where the jet axis in the northern hemisphere tilts equatorward while the jet axis in the southern hemisphere tilts slightly poleward. For these composite states, there are clear differences in the characteristic mean flow between hemispheres. Contrasting features of the mean flow between transport modes are most distinct in the northern hemisphere while the mean flow is considerably stronger throughout the domain in the southern hemisphere. In addition, the meridional extent of the wavebreaking signature (equivalent latitude fold) is smaller in the southern hemisphere for all modes, possibly due to the increased jet strength there. The observed differences in transport mode flow geometry between hemispheres may be related to differences in the large-scale geometry of the subtropical jet. In addition, the poleward and equatorward

transport modes are consistent with the characteristics of primarily poleward (P2) and primarily equatorward (LC1) anticyclonic wavebreaking events, evidenced by the meridionally folded equivalent latitude field relative to the mean 13 km tropopause altitude contour (the tropopause break) and the mean latitudes of the wavebreaking region (see Table III).

The seasonal dependency of the three transport modes illustrates their contribution to the observed annual cycle of transport at 380 K (Figure 20b). Annual cycles of the monthly frequency of the three transport modes relative to the total annual frequency of each mode are shown for the southern and northern hemispheres in Figure 25. For both hemispheres, the equatorward transport mode shows a distinct peak during summer while the poleward transport mode shows two peaks: a smaller one during late spring/early summer and one nearly twice as large during fall. Annual cycles of the bidirectional transport mode show a broad peak from late spring to late fall in each hemisphere. These annual cycles in transport mode frequency illustrate that the directional transport modes largely control the observed annual cycles in air mass transport in Figure 20b.

In addition to transport estimates and the dynamical characterization of Rossby wavebreaking events, geographical distributions of wavebreaking events are useful for air mass source characterization. Figures 26a–26f show hemispherically normalized geographical distributions of wavebreaking events for various seasons and wavebreaking evolution at the four potential temperature levels. The significant variability in the location of wavebreaking maxima across all altitudes, especially in the northern hemisphere, illustrates the observed sensitivity of wavebreaking to the geometry of the flow. Wavebreaking at lower altitudes is largely determined by the characteristics of the subtropical jet, while wavebreaking aloft is controlled by the geometry of the polar vortices. The transitional altitude between these competing flow regimes is near

420 K in the ERA-Interim reanalysis. Figure 26a shows the geographical distribution of anticyclonically sheared wavebreaking events at 350 K during hemisphere summer. In the northern hemisphere, two distinct maxima are observed: one over the central Pacific and another over the eastern Atlantic. In the southern hemisphere, one distinct maximum is observed in the southeast Pacific just west of the southern tip of South America while a broader, less distinct maximum is observed south and west of Australia over the Indian ocean. These distributions are comparable to previous climatologies at 350 K [e.g., 20].

Figure 26b shows the geographical distribution of anticyclonic wavebreaking events at 500 K during hemisphere winter. One large, dominant maximum in wavebreaking frequency is observed in each hemisphere. The northern hemisphere maximum stretches from the south of Alaska to the south-central United States over the eastern Pacific and the southern hemisphere maximum, broader in longitude and narrower in latitude, stretches from the southeastern tip of Africa over the Indian ocean to the south-central Pacific. Weaker and much smaller maxima are observed at 500 K in the northern hemisphere over southeast Asia and the eastern Atlantic, and in the southern hemisphere over South America.

Figures 26c and 26d show geographical distributions of anticyclonic wavebreaking events at 380 K for the summer and fall, respectively. These two seasons are shown in order to characterize source regions of the transport modes identified in Figures 23, 24 and 25 above. Overlaid on each map at 380 K are contours of hemispherically normalized frequency maxima of two of the three previously identified transport modes. The thick white contours in both maps show frequency maxima of the bidirectional transport mode. In Figure 26c (380 K summer), the thick black contours show frequency maxima of predominately equatorward transport. It is evident from this distribution that the anticyclonic features observed in the composite

means in Figure 24b largely correspond to wavebreaking frequency maxima downstream of stationary anticyclones in each hemisphere. In the northern hemisphere, the observed frequency maximum in the western Pacific is dominated by equatorward transport immediately downstream of the southeast Asian monsoon anticyclone while the maximum over North America is dominated by bidirectional transport. In the southern hemisphere, there are three maxima of equatorward transport. The maximum in the western Pacific is immediately downstream of the Australian monsoon anticyclone, while the maxima over the Indian ocean and Atlantic are downstream of much smaller anticyclones not associated with large-scale monsoon circulations. The maxima in equatorward transport over the Indian ocean and southwest Pacific are located upstream of bidirectional transport maxima, while the weaker maximum over the southern Atlantic is dominated by extratropics-to-tropics transport. In Figure 26d (380 K fall), the thick black contours show frequency maxima of predominately poleward transport. In the northern hemisphere, one maximum is observed over the far eastern Atlantic and is located in the region of a climatological split in the subtropical jet (see Figure 1). This split jet feature is most prevalent over the northern Atlantic during fall, while the split jet feature observed over the northern Pacific is most prevalent during spring (not shown). In the southern hemisphere, a broad poleward transport frequency maximum stretches from the Indian ocean to the western Pacific and corresponds to a weaker climatological split subtropical jet there. For both hemispheres, the tropics-to-extratropics transport frequency maxima at 380 K during fall lie immediately downstream of bidirectional transport frequency maxima.

Figures 26e and 26f show geographical distributions for all seasons at 420 K for anticyclonic and cyclonic wavebreaking events, respectively. The distributions of anticyclonic events at 420 K show two distinct maxima in the northern hemisphere and one maximum in the southern hemisphere. For cyclonically sheared wavebreaking

events, there are two distinct maxima observed in each hemisphere. These maxima are generally located in regions of relatively low anticyclonic wavebreaking frequency and correspond to equatorward displacements of the subtropical jet, which result in cyclonic meridional wind shear along the tropical boundary.

C.   Convective Injection into Stratospheric Intrusions

1.   START08 Analysis

a.   Research Flight 12

Research Flight 12 (RF12) provides the clearest observations from START08 of convection penetrating into a stratospheric intrusion. The flight took place on 15 May 2008 from 15:58 to 20:35 UTC. It targeted a stratospheric intrusion descending below the polar jet stream over western Colorado and eastern Utah. Figure 27a shows the 300 hPa wind speed and geopotential height over the continental United States at 18 UTC on 15 May. The flight track is shown on the map by the thick black line with a gray border. The observed stratospheric intrusion, which is shown in the vertical section in Figure 27b, is on the western side of a large-amplitude trough. The section is taken along the red line A–B in Figure 27a. In the section, the intrusion can be seen by the vertically folded structure of the potential vorticity (PV, purple contours). On the anticyclonic side of the jet, the lapse-rate tropopause (orange line) coincides closely with the sharp PV gradient between the troposphere and stratosphere; but on the cyclonic side of the jet, the bottom of the intrusion is between 2 and 7 km below the lapse-rate tropopause. The coordinates of the flight track are shown in black and red and are projected onto the vertical section. During the flight, the aircraft sampled the observed stratospheric intrusion several times and encountered convection within the intrusion during one segment of the flight: the portion of the flight track

highlighted in red in Fig. 27b.

Scattered convection occurs over western Colorado throughout RF12. Figure 28 shows the composite radar reflectivity from the Grand Junction, Colorado NEXRAD site (KGJX) at 17:12 UTC. This coincides with the flight segment where convection was observed to be penetrating into the stratospheric intrusion. The flight track and location of the aircraft at the radar analysis time are shown in black and the flight segment with observed convective influence in red, with the aircraft nose pointing in the flight direction. The radar reflectivity shows that the aircraft sampled two convective systems along the red flight segment, one just before the radar analysis time shown and the other just after. Hereafter, the first convective system sampled will be referred to as convective plume 1 (CP1) and the second as convective plume 2 (CP2). The presence of active convection at the aircraft altitude is verified by images from the wing-mounted video camera aboard the GV aircraft. Figures 29a & 29b show snapshots from convective plumes CP1 and CP2, respectively. During CP1 the aircraft sampled the top of a convective anvil cloud and during CP2 the aircraft sampled a convective updraft, as can be seen from the ice on the camera lens in Fig. 29b.

Data from the GV aircraft show tropospheric levels of trace gases at the times of the encounters with the convective plumes. Figure 30a is a vertical section of radar reflectivity, PV, and aircraft altitude along the red segment of the flight track overlaid with in situ ozone and water vapor measurements . In addition, mean ice particle diameter is plotted directly below the section to identify observations made within clouds. The flight path during this flight segment was straight, level, and within the stratospheric intrusion (black line). The GFS and radar analyses are interpolated in space and time to the flight track. There is no radar information below $\sim$4 km in the vertical section because the altitude of the radar used here, KGJX, is 3.05 km.

The encounters with convective plumes CP1 and CP2 (marked by the red vertical lines) are accompanied by peaks in water vapor (500–700 ppmv) and, conversely, valleys in ozone (50–75 ppbv). These features coincide with the radar echoes. Mean ice particle diameters in the convective plumes are $\sim$30-35 μm for both CP1 and CP2. Measurements outside of the convective plumes show higher concentrations of ozone ($>$150 ppbv) and lower water vapor ($<$200 ppmv), characteristic of mixed extratropical tropospheric and stratospheric air. The in situ measurements are at altitudes near or above the 4 pvu surface and up to 2 km above the bottom of the stratospheric intrusion. Figures 30b, 30c, 30d & 30e show the recent history of radar reflectivity for the air parcels sampled by the aircraft along this flight segment from backward trajectory calculations. Vertical radar reflectivity sections are plotted along the material line defined by the aircraft path advected backwards in time from the aircraft analysis time to 15, 30, 45 and 60 minutes earlier, respectively. That is, for a given aircraft measurement, the radar reflectivity in the column containing that air parcel at past times is mapped to the vertical section of aircraft data. For both convective plumes, the magnitude and vertical extent of reflectivity decreases at earlier times, suggesting that the convective influence occurred in the recent past (within the prior 45 minutes).

Analysis of medium to long-lived trace gas measurements from the GV aircraft illustrates the characteristic source air masses and mixing regimes observed during RF12. In Figure 31a, observations of ozone (O_3) and carbon monoxide (CO) are colored by aircraft potential temperature to identify different mixing regimes. The relationship between O_3 and CO can be used to identify the stratosphere, troposphere, and tropopause transition layer [e.g., 110, 111, 41]. The troposphere, stratosphere and transition branches are clearly visible in the aircraft measurements. Following the methods in [41], the stratospheric and tropospheric branches are identified us-

ing least-squares polynomial and linear curve fitting, respectively. We use CO < 30 ppbv and O_3 < 70 ppbv to compute the fits for the stratospheric and tropospheric branches. Two characteristic mixing lines (tropopause transition layers) are observed during RF12: tropical and extratropical. They can be distinguished by their potential temperatures (labeled in Fig. 31a). The aircraft sampled tropical upper tropospheric (UT) air above the stratospheric intrusion on the anticyclonic side of the jet (labeled in the vertical section in Fig. 27b). Backward trajectories reveal that this air was in the tropical UT a few days earlier (latitude < 25° N, not shown). The tropical UT air has higher potential temperatures than the extratropical mixing layer, due to its location above the jet core and below the high tropopause on the equatorward side of the jet. This tropical UT air also has much lower O_3 than is typically found in the extratropical transition layer, likely due to convective detrainment of tropical lower troposphere air [e.g., 115]. In Figure 31b, mixing by convective injection can be identified by high concentrations of water vapor (>100 ppmv, blue dots) in the extratropical transition layer branch. Additionally, the tropospheric source for convective injection has ∼130 ppbv of CO, while the tropospheric source for the remaining observations (no convection, red dots) in the extratropical transition layer has ∼100 ppbv.

b.   Research Flight 6

Research Flight 6 (RF06) took place from 1 May 2008 at 19:51 UTC to 2 May 2008 at 00:10 UTC. It targeted a stratospheric intrusion descending below the polar jet stream over southern Colorado and northern New Mexico. The aircraft briefly encountered convection penetrating into the intrusion on two legs of the flight, shown in red in Figure 32b. As in Figure 27, Figures 32a and b show 300 hPa wind speed and geopotential height over the continental United States and a vertical section of

the GFS analysis at 00 UTC on 2 May, respectively. The flight sampled the observed stratospheric intrusion near the axis of a large-amplitude trough. The section, taken along the red line A–B in Figure 32a, shows that the aircraft sampled the observed stratospheric intrusion several times and at various altitudes. The bottom of the intrusion in this case is up to 5 km below the model lapse-rate tropopause on the cyclonic side of the jet.

The aircraft flew near convective tops during two portions of the flight over southern Colorado. There are large, ongoing areas of shallow convection over south-central and southeastern Colorado throughout the flight. Figures 33a and 33b show maps of the composite radar reflectivity from the Pueblo, Colorado NEXRAD site (KPUX) near the times of each observation of convective injection, 21:47 and 23:42, respectively. The aircraft location at the radar analysis time and flight track (within 30 minutes of the analysis time) are shown on each map. As in Figure 32b, the red portions of the flight track illustrate measurements during the encounters with convection. The radar reflectivity shows that each observation of convective injection during RF06 was sampled near, but not directly inside, systems penetrating the intrusion.

Trace gas measurements from the aircraft during RF06 show similar characteristics to those observed during RF12. Figures 34a and b, similar to Figure 30a, are vertical sections of PV and tropopause altitude overlaid with in situ measurements of ozone, water vapor and mean ice particle diameter and aircraft altitude during each encounter with convective injection. Observations of convective influence are highlighted by a light gray background in each section. During the first encounter (Figure 34a, 21:45–21:51 UTC) the aircraft sampled air with high water vapor (>400 ppmv) and low ozone ($\sim$100 ppbv) at PV of 2–4 pvu and below the model lapse-rate tropopause near 21:49 UTC. Observations near the ozone minimum during this

flight segment show the presence of convective cloud (large ice particles). In agreement with RF12, measurements outside of the cloud show higher concentrations of ozone (>200 ppbv) and lower water vapor (100–200 ppmv), characteristic of mixed extratropical tropospheric and stratospheric air. During the second encounter with convective injection (Figure 34b, 23:39–23:45 UTC) the aircraft sampled air with similar characteristics at PV up to $\sim$4 pvu while descending through the boundary of the intrusion. The presence of convective cloud during this segment of the flight is observed at PV up to $\sim$2 pvu. Additional analyses of long-lived trace gas measurements for the convective injection observed in RF06 (not shown) are comparable to the results given for RF12 (e.g., Figure 31b).

c.   Trace Gas Relationship

In addition to understanding the source air masses and mixing from measurements of long-lived trace gases, finding a unique signature of convective injection into stratospheric intrusions would be useful for future studies. Figures 35a, b, and c show density plots of O_3 and water vapor (H_2O) measurements for RF12, RF06, and the remaining START08 flights, respectively. Figure 35c does not include data from research flights 1-3 due to the lack of VCSEL water vapor data. During the remaining thirteen flights, the aircraft did not fly through convection penetrating into a stratospheric intrusion. The measurements of convective injection during RF12 and RF06 are identified by the blue and green ellipses in Figures 35a and b, respectively. The observations enclosed by the ellipses for each research flight show lines of mixing between the convectively injected tropospheric air and stratospheric air in the intrusions. The endpoints of these mixing lines identify the trace gas concentrations for each source air mass. In the vertical sections for each flight (Figures 30a and 34), the observations within the convective clouds lie close to the tropospheric ends of

the observed mixing lines. The red ellipse in Figure 35c shows the combined area of the blue and green ellipses at $H_2O > 100$ ppmv and shows that for the remaining START08 flights there are few or no observations within the O_3-H_2O space enclosed by the ellipse. These comparisons show that, in all of the measurements made during the START08 project, air from convective injection in stratospheric intrusions is uniquely characterized by $H_2O \geq \sim 100$ ppmv and $O_3 \geq \sim 125$ ppbv.

2. Case Study: 11 April 2008

The in situ measurements, model analyses, and radar reflectivities from RF12 and RF06 provide direct evidence of moist convection penetrating into a stratospheric intrusion. Unfortunately, both cases from START08 occurred over high altitude terrain where mean sea-level pressure reductions of the surface meteorology can be complicated and often not representative of the responsible synoptic features [e.g., 116]. As we have shown, however, it is possible to use meteorological analyses and radar data to identify and analyze this type of event. In this section, we use GFS analyses and NEXRAD radar data to carry out an additional case study of convective injection in a stratospheric intrusion over the great plains of the continental United States. This example will help develop a better understanding of the relationship between the synoptic-scale meteorology and occurrence of convective injection.

On 11 April 2008 a mid-latitude cyclone and associated frontal system was propagating south and east over the great plains of the continental United States. This frontal system was associated with a deep stratospheric intrusion descending along the eastern side of a large-amplitude upper-tropospheric trough. Figure 36a shows mean sea level pressure from the GFS analysis and the National Weather Service (NWS) Hydrometeorological Prediction Center (HPC) surface frontal analysis for 11 April at 00 UTC. The center of the surface cyclone (large red "L") is located near the

Nebraska-Iowa border at the analysis time. There are two surface cold fronts present: the front farther east (cold front 1) is along the leading edge of the deep stratospheric intrusion while the other (cold front 2), lies behind. Cold front 1 has a weak temperature (and moisture) gradient (not shown), which is indicated somewhat by its stationary character in southern Arkansas and Central Texas. Cold front 2, behind the intrusion, has a strong temperature gradient and a classic pressure "kink" along the frontal boundary. These thermal relationships reverse at upper levels, where the temperature gradient for cold front 1 is strong (not shown). Figure 36b shows wind speed and geopotential height at 300 hPa for 11 April at 00 UTC. The upper-level trough and associated cyclone center (large magenta "L") are nearly aligned with the surface cyclone. The upper-level cyclone center is slightly west and south of the observed surface cyclone. For clarity, the remaining analyses are shown for the same analysis time as Fig. 36.

The depth of the 11 April stratospheric intrusion is shown in the map in Figure 37a as the *lowest* altitude of the 2 pvu potential vorticity surface. Areas where the 2 pvu surface is folded (and the altitude is multi-valued) are colored in blue. Areas where the 2 pvu altitudes are less than 6.5 km are outlined by the thick black line. The location of the surface cyclone center is denoted by the large red "L" (as in Fig. 36a). A vertical section of PV, wind speed, the lapse-rate tropopause and NEXRAD radar reflectivity taken along the line A–B is shown in Fig. 38. In Figure 37a, the areas where the intrusion is closest to the surface are often in regions where the 2 pvu surface is folded, characteristic of descent below the cyclonic side of the upper-tropospheric jet stream. The folded structure of PV can be clearly seen in the vertical section, with the 2 pvu surface up to 7 km below the lowest identifiable lapse-rate tropopause (Fig. 38). The analyzed lapse-rate tropopause in this case may be misidentified as the secondary tropopause near the jet stream as illustrated by the

large jump from 10 to 17 km in the middle of the section [e.g., 81]. In Figure 37b, the composite radar reflectivity is displayed along with the boundary of the deepest part of the fold (as in Fig. 37a) with areas where the 2 pvu surface is folded outlined by a thick white line. There are several mesoscale convective systems (MCSs) and scattered convective cells throughout the domain. The vertical section A–B slices through one of the MCSs in an area where the stratospheric intrusion is deep, but not folded. In Fig. 38 the radar reflectivity shows that the MCS reaches altitudes up to ~10 km. At this level, which is as much as 5 km above the bottom of the intrusion, PV is >4 pvu. To measure the depth of penetration of the convection into the fold, the maximum altitudes of the 10 dBZ and 20 dBZ radar reflectivity surfaces relative to the 2 pvu surface are shown in Figures 37c and d, respectively. Red colors indicate locations where convection penetrates through the 2 pvu surface. For reference, the boundaries of the fold are shown as in Figure 37b. The highest convective injection into the intrusion is observed for two large MCSs in central Iowa and Missouri in areas where the intrusion is deep, but not folded. There are also a few convective cells in western Illinois along the leading edge of the intrusion with tops well above the bottom of the intrusion. The intrusion near these convective cells, however, is folded and the mass of stratospheric air mixed with tropospheric air by the convection is limited compared to the deep convection in areas where the intrusion is not folded. Some convection does penetrate the 2 pvu surface away from the fold where it lies at higher altitude and near the lapse-rate tropopause (e.g., northeastern Arkansas). The depth of injection in those areas , however, is significantly less than where convection penetrates into the intrusion.

3. Trajectory Analysis

One question of importance is whether tropospheric air injected into the fold by convection is simply returned to the troposphere by the descending intrusion, or whether it mixes with air that remains in the stratosphere. To address this question we compute 5-day forward trajectories for the convective injection events from the three case studies. For a typical stratospheric intrusion length scale of 3000 km and a wind speed of 30 m s^{-1}, the time scale for an air parcel to travel the length of an intrusion is 10^5 seconds ($\sim$1 day). The life cycle of a stratospheric intrusion, however, can be greater than 4 days. Therefore, a timescale of 5 days is appropriate for the identification of the transport direction of stratospheric air within the fold at the analysis time. It is important to emphasize that these trajectories are driven by the large-scale winds from the GFS analyses and do not include vertical transport by the convection. Rather, the trajectories show the large-scale transport of the convectively influenced air mass.

Figures 39a, b and c show vertical sections of GFS analyses, NEXRAD radar reflectivity ≥ 1 dBZ, and the destination layers for air parcels initialized along the vertical sections for each case. The section for RF12 (Figure 39a) is taken parallel to the flight segment where convective injection is observed. Radar reflectivities for RF12 are from the analysis time shown in Figure 28. The section for RF06 (Figure 39b) is at the same coordinates as that in Figure 32b and is taken parallel to the flight track and near the observations of convective injection. Radar reflectivities for RF06 are given as the maximum reflectivity of the two analysis times shown in Figure 33. The scattered radar reflectivity features seen above the lapse-rate tropopause in this case are all < 5 dBZ and are identified as ground clutter (beam side-lobe contamination) from the mountains west of KPUX. For the NEXRAD radar beam,

side-lobe contamination peaks at -29 dB, which is ~3 degrees from the beam center in all directions. The mountains west of KPUX are at elevations up to ~3 km above the altitude of the radar. Under typical atmospheric refraction of the radar beam, side-lobe contamination is possible up to scan elevations of ~6 degrees or altitudes of 9-13 km at the ranges from KPUX in the vertical section for RF06. The section for the 11 April case study (Figure 39c) is the same as that in Figure 38. For each section, the gray color-filled areas indicate stratospheric air that was transported into the troposphere, defined as forward trajectory particles with PV $\geq$ 1 pvu at the analysis time and altitude below the GFS lapse-rate tropopause 5 days later. Due to column stretching and consequent changes in the static stability, the bottom of a stratospheric intrusion may lie several kilometers below the lapse-rate tropopause. Depending on the subsequent Lagrangian history, however, the air in the intrusion may remain in the stratosphere or be irreversibly transported into the troposphere.

For RF12, the stratospheric intrusion and much of the lower stratospheric air on the cyclonic side of and below the altitude of the polar jet maximum moves into the troposphere. For RF06, most of the stratospheric intrusion air mass up to and within ~1 km of the analyzed lapse-rate tropopause is transported into the troposphere. For the 11 April case, the air transported into the troposphere is largely limited to that lying near the boundary of the stratospheric intrusion (PV < 4 pvu). For both START08 research flights, the trajectories show that the tropospheric air injected into the stratosphere by convection returns to the troposphere within a few days. For the 11 April case, much of the convectively influenced air mass at high PV (>4 pvu) remains in the stratosphere (i.e., no gray color-filling). This relationship is clearly shown in the higher altitudes of the MCS (middle of figure 39c).

It is important to note that the convective injection events for the START08 flights and the 11 April case study occur on opposite sides of their associated upper-

level trough axes. For RF12 and RF06, the injection is observed on the upstream side of the upper-level trough, where curvature effects of the wind reinforce the cross-jet ageostrophic circulation that facilitates stratospheric intrusions and descent on the cyclonic side of the jet (see Chapter I). For the 11 April case study, convective injection is observed on the downstream side of the upper-level trough, where curvature effects weaken the descent in the fold. These differences in the ageostrophic circulation may be important in determining the primary direction of STE.

CHAPTER V

SUMMARY & DISCUSSION

Tropospheric intrusions observed during START08 show good correspondence between the observed kinematics from the NCEP GFS analyses and in situ measurements of trace gases aboard the aircraft. The tropospheric intrusions sampled by the GV aircraft can be traced back to Rossby wavebreaking events. For both RF01 and RF14, intruding air from the tropical upper troposphere was sampled well north of the subtropical jet and several kilometers above the extratropical tropopause. Back trajectories show that transport in these events took place above the subtropical jet and along isentropic surfaces (Figures 10 & 14). The intruding air masses are characterized by low PV, low static stability, and chemical composition more typical of the troposphere.

The mixing timescales of the observed tropospheric intrusions can be estimated by fitting a simple box model (Chapter IIIA) to trace species with varying lifetimes (Table I). The model fits for both RF01 and RF14 give a mixing timescale of 5 to 6 days. This mixing timescale is an important parameter to understand when considering this type of transport and mixing in applications such as chemistry-climate model validation (CCMVal, [117]).

A global analysis of tropospheric intrusions for April–June 2008 found 19 significant tropospheric intrusions. All but one of the intrusion events had its source over the Tropical Pacific. In our analysis, we found Rossby wavebreaking in the west/central Pacific and east Pacific regions to be common, with a higher frequency of occurrence in the west/central Pacific. Tropospheric intrusions in the west/central Pacific are related to high-frequency large-amplitude Rossby wavebreaking events as discussed in the previous literature [e.g., 20, 118, 29]. Tropospheric intrusions in the

east Pacific region are related to equatorward Rossby wavebreaking in the Pacific westerly duct. The high frequency of tropospheric intrusions in the east Pacific may be due to La Niña conditions present during 2008.

Several filaments of air with tropospheric properties were observed in the 370–400 K potential temperature range during START08. These filaments are seen in the in situ trace gas measurements by the aircraft, but the Eulerian analyses fail to represent these small-scale features. As discussed in section 3, it is likely that these air masses were part of larger tropospheric intrusion events more than a week prior to being sampled by the GV aircraft. Therefore, the intrusions have had time to mix further and deform with the large-scale synoptic flow, rendering them indistinguishable in large-scale dynamical and meteorological fields. The air still possesses, however, characteristics that are significantly different than the surrounding background stratosphere (Figure 15). These observations suggest that irreversible transport by tropospheric intrusion events is common, at least during the START08 experiment period (April-June 2008). Further confirmation of a relationship between the filaments and prior tropospheric intrusion events was found by using reverse-domain-filled maps of equivalent latitude (Figure 16). This approach provides a more detailed representation of tropospheric intrusions and their filamentation than the diagnostics given in [10]. It can also be used for operational forecasts in future aircraft missions.

It is evident from our analysis during the START08 experiment that tropospheric intrusions are a common mechanism of STE. These intrusions can have a significant impact on the composition and distribution of trace species in the middleworld. Although tropospheric intrusions can be readily related to large-amplitude Rossby wavebreaking over the Pacific and Atlantic oceans, breaking of equatorward propagating Rossby waves in the westerly ducts appears to play a significant role, which may be more significant during the ENSO cold phase (La Niña).

The observed frequency, seasonality, transport characteristics, and geographical distributions of Rossby wavebreaking events at the equivalent latitude of the tropopause break in the 350–500 K potential temperature range have been analyzed from 30 years of ERA-Interim reanalyses. The results presented in this study are, with the exception of transport, in good agreement with the results from previous studies of the "dynamical tropopause" at 350 K, which ranges from 1.5–3.5 pvu in the referenced literature. In this study, anticyclonically sheared wavebreaking events dominate at all altitudes and are observed most frequently in the southern hemisphere. Cyclonically sheared wavebreaking events are observed most frequently in the northern hemisphere and reach a maximum in the stratosphere at 420 K, strongly decreasing in frequency above and below this level. Similarly, the total number of wavebreaking events reaches a maximum at 420 K, with the lowest wavebreaking frequencies observed near the core of the subtropical jet (350–360 K). Results for each hemisphere are comparable.

Air mass area transport for each Rossby wavebreaking event was estimated using a Lagrangian method described in detail in Chapter IIIB2. The net annual wavebreaking transport is observed to be equatorward within the 370–390 K potential temperature range and poleward at altitudes above and below. Away from 420 K, transport from Rossby wavebreaking shows significant seasonal variability with a strong peak during hemisphere summer at lower levels (≤400 K) and a winter peak at upper levels (≥450 K), consistent with previous isentropic transport studies. Although the observed seasonal cycles in transport are consistent with results from previous work, the magnitude and direction of transport show significant differences. Notably, the observed direction of transport in the 350–360 K potential temperature range is in disagreement with previous studies. These discrepancies are shown to be largely dependent on the choice of tropics-extratropics (or troposphere-stratosphere) boundary

in the dynamical field. Absolute values of PV at the tropopause break (or tropical boundary) in this study are found to be $\geq\sim4$ pvu at all analyzed altitudes, while the more commonly used 2 pvu contour is found deeper into the tropics (Figs. 4b & 5a). When a PV value of ±2 pvu is used for analysis, the transport direction is shown to reverse and become consistent with previous studies (contrast Figs. 20a & 21). These results suggest that the use of 2 pvu is not representative of the boundary between troposphere and stratosphere at this level and leads to a misidentification of the net direction of transport, at least in the ERA-Interim reanalysis. The general characteristics of the geographical distributions at 350 K, however, seem to be independent of analyzed dynamical boundary. As identified in Chapter IIIB1, the annual cycle of a dynamical boundary at the tropopause can vary significantly and care should be taken when evaluating transport relative to such a boundary. Furthermore, several previous studies have also used ±2 pvu as the troposphere-stratosphere boundary on lower potential temperature levels that vertically intersect the lapse-rate tropopause in the extratropics. [98] show that there is also significant seasonal variability in PV at the tropopause below 350 K, which is often nearer ±3 pvu. The sensitivity of transport estimates to this boundary at lower levels is not known.

Frequency distributions of wavebreaking events as a function of the fractional transport of the tropical and extratropical air masses allow for the identification of three prevalent modes of anticyclonic wavebreaking transport near the subtropical jet: poleward, equatorward and bidirectional. Composite mean meteorological and dynamical fields identify characteristics of the mean flow for each transport mode. The poleward transport mode is shown to be associated with a split subtropical jet, as proposed in the Introduction. In addition, geographical distributions of poleward transport are found to be collocated with climatological split features of the jet in the spring and fall of each hemisphere, suggesting that the geometry of the mean flow

largely determines the wavebreaking evolution and subsequent transport. Comparatively, events within the equatorward transport mode are shown to be located immediately downstream of large anticyclones during hemisphere summer and not associated with a split subtropical jet. These equatorward transport events are responsible for the observed net transport into the tropics in the 370–390 K potential temperature range and are primarily associated with monsoon circulations. Bidirectional transport events are observed during all seasons and are generally collocated with all global frequency maxima, except for that downstream of the southeast Asian monsoon during north hemisphere summer which is uniquely a source for extratropics-to-tropics wavebreaking transport. Furthermore, the equatorward and poleward transport modes are comparable to the LC1 and P2 classifications from [24] and [25], respectively.

The mechanisms for the development and maintenance of split subtropical jets are not known, though they occur frequently during transition seasons in both hemispheres (see Fig. 1). Numerical studies suggest that their stability may, in part, be a result of baroclinic eddy accumulation poleward of a preexisting subtropical jet, or eddy moment flux divergence between the poleward and equatorward jet components of a split jet [e.g., 119, 120]. The results presented here suggest that these splits in the subtropical jet are distinct pathways for tropical UTLS air into the extratropical LS. Few studies have analyzed observations within these transported air masses and no in situ observations near the subtropical jet during the development of one of these wavebreaking events have been analyzed at this time. In addition, little is known about the dominant equatorward transport downstream of the monsoon circulations. Monsoon circulations are known to inject polluted boundary layer air deep into the tropical LS via convection and large-scale ascent [e.g., 7]. The results presented in this study suggest that transport of extratropical LS air into the tropics downstream of monsoon anticyclones may play a critical role in determining the composition of

the tropical UTLS and subsequent ascent into the Brewer-Dobson circulation. In situ meteorological and chemical observations of these processes will help to further characterize the climatological impact of these events. Analysis of trace gas observations from satellites in the UTLS will also be helpful.

It is evident from the transport analyses presented and the example given in Figure 2 that the sensitivity of transport to the dynamical boundary used, even between troposphere and stratosphere in the horizontal dimension, requires further evaluation. Previous studies have shown that the lapse-rate tropopause sharply identifies the transition between troposphere in stratosphere both chemically and dynamically [e.g., 41, 42, 121]. It has also been shown previously and within this study that dynamical variables such as PV (or equivalent latitude) at the lapse-rate tropopause can vary significantly with season and meteorological condition. Identifying the best representation between troposphere and stratosphere in these dynamical variables at all altitudes is necessary for accurate transport determination. Consequently, transport studies at lower altitudes should be updated to reflect potential dependencies of the magnitude and direction of transport on the choice of troposphere-stratosphere boundary.

Aircraft observations from START08 provide the first direct, in situ measurements of convective injection into a stratospheric intrusion. Because the lapse-rate tropopause does not coincide with the bottom of descending stratospheric intrusions, this would not normally be identified as overshooting convection penetrating into the stratosphere. During RF12, the peaks and valleys in trace gas and microphysical data coincide exactly with passage through convective cloud tops, as evidenced by the wing camera imagery from the GV aircraft (Figure 29). Radar reflectivities and trace gas measurements also agree well, demonstrating significant convective influence within the observed intrusion. Similar results are presented for RF06, which sampled

convectively injected air near, but not through, the tops of active convection. Convection is observed at altitudes up to 3 km above the bottom of the intrusion during RF12 and up to 2 km above the bottom of the intrusion during RF06 (Figure 39). The convectively injected air masses observed during START08 have characteristics of a mixture of stratospheric and lower-tropospheric or boundary layer air and can be uniquely characterized by $H_2O \geq \sim100$ ppmv and $O_3 \geq \sim125$ ppbv. A wider range of samples will be required to establish that this trace gas relationship is unique to convectively injected air in all circumstances.

The 11 April 2008 case study illustrates the potential extent of convective mixing associated with a tropopause fold. The observations show that convective injection can be deep, reaching altitudes more than 5 km above the bottom of the intrusion and PV surfaces >4 pvu, near the altitude of the polar jet maximum. Based on these cases and previous research, we propose a conceptual model of the synoptic conditions conducive to convective injection in stratospheric intrusions. Figure 40 is a schematic of the surface and upper-level meteorological conditions characteristic of such transport events. In the mature or decaying phase of a mid-latitude cyclone, when the upper-level trough catches up with the low-level cyclone, the upper-level polar jet stream can be located above the warm sector of the surface cyclone. Given the existence of a stratospheric intrusion, deep convective injection is most likely along or ahead of the leading edge of the surface cold front. This meteorological condition is well documented and often referred to as a "split front", meaning the surface and upper level fronts (commonly the leading edge of the intrusion) are not continuous with height [e.g., 122, 123, 124]. Because this is a common synoptic situation, it seems likely that convective injection into stratospheric intrusions is a relatively frequent occurrence in midlatitudes. In fact, recent work suggests this meteorological condition may be a consequence of the midlatitude cyclone occlusion

process [e.g., 125].

It should be noted that the PV analyses shown here do not account for the non-conservative processes associated with the penetrating convection that irreversibly mix tropospheric and stratospheric air. This convective mixing can erode the lower altitude intrusion air mass and effectively elevate the tropopause. The PV analyses do, however, illustrate the bounds of stratospheric influence associated with the observed intrusions. This relationship is shown clearly in Figures 30a and 34.

Downward transport of stratospheric air into the troposphere by tropopause folding has been known and studied for many years. The trajectory analysis for the three cases shows that STE can potentially occur in both directions due to tropopause folding. When deep convective injection occurs, it could have a significant impact on the distribution of chemically and radiatively important trace species in the lower stratosphere. The transport direction, and even the depth of convective injection, may be dependent on the strength of the cross-jet ageostrophic circulation that facilitates stratospheric intrusions, as suggested by Figure 39 (see also the discussion in Chapter I).

The depth of convective injection is greater in the 11 April case study than during START08 RF12 and RF06. The depth and extent of convective injection in a stratospheric intrusion may have a larger impact on the composition of the UTLS than deep convection penetrating a flat tropopause. The frequency of occurrence and seasonality of these events, however, are not well known. In previous studies, convective overshooting of the lapse-rate tropopause is found at altitudes in the lower stratosphere with peak ozone (O_3) concentrations of 150–200 ppbv [e.g., 72, 73, 75]. The peak ozone concentrations at the altitude of convective injection in the stratospheric intrusions observed during START08 RF12 and RF06 are comparable at $\sim$200 and $\sim$250 ppbv, respectively (Figures 30, 31 and 34). It is also possible that convection

penetrates more deeply into stratospheric intrusions due to the lower static stability relative to the unfolded tropopause [e.g., 123, 126]. Recent modeling studies suggest that the contribution of moist convection to stratosphere-to-troposphere transport can be large in midlatitudes, especially over land during the summer [e.g., 127, 128]. Therefore, an understanding of the relative contributions of convective injection into stratospheric intrusions and convective overshooting of the lapse-rate tropopause, as well as their seasonality, is important for the accurate determination of STE in the extratropics.

REFERENCES

[1] S. P. Sander, R. R. Friedl, A. R. Ravishankara, D. M. Golden, C. E. Kolb, M. J. Kurylo, M. J. Molina, G. K. Moortgat, H. Keller-Rudek, B. J. Finlayson-Pitts, P. H. Wine, R. E. Huie, and V. L. Orkin, "Chemical kinetics and photochemical data for use in atmospheric studies: Evaluation number 15," *Jet Propulsion Laboratory*, vol. 6, no. 2, pp. 1–77, 2006.

[2] B. J. Hoskins, "Towards a PV-theta view of the general circulation," *Tellus*, vol. 43, pp. 27–35, 1991.

[3] J. R. Holton, P. H. Haynes, M. E. McIntyre, A. R. Douglass, and L. Pfister, "Stratosphere-troposphere exchange," *Rev. Geophys.*, vol. 33, no. 4, pp. 403–439, 1995.

[4] A. Stohl, H. Wernli, P. James, M. Bourqui, C. Forster, M. A. Liniger, P. Seibert, and M. Sprenger, "A new perspective of stratosphere-troposphere exchange," *Bull. Am. Meteorol. Soc.*, vol. 84, no. 11, pp. 1565–1573, 2003.

[5] A. W. Brewer, "Evidence for a world circulation provided by the measurements of helium and water vapour distribution in the stratosphere," *Q. J. R. Meteorol. Soc.*, vol. 75, pp. 351–363, 1949.

[6] G. M. B. Dobson, "Origin and distribution of the polyatomic molecules in the atmosphere," *Proc. Roy. Soc. London*, vol. 236, no. 1205, pp. 187–193, 1956.

[7] W. J. Randel, M. Park, L. Emmons, D. Kinnison, P. Bernath, K. A. Walker, C. Boone, and H. Pumphrey, "Asian monsoon transport of pollution to the stratosphere," *Science*, vol. 328, pp. 611–613, 2010.

[8] M. A. Olsen, A. R. Douglass, P. A. Newman, J. C. Gille, B. Nardi, V. A. Yudin, D. E. Kinnison, and R. Khosravi, "HIRDLS observations and simulation of a lower stratospheric intrusion of tropical air to high latitudes," *Geophys. Res. Lett.*, vol. 35, L21813, 2008.

[9] M. A. Olsen, A. R. Douglass, M. R. Schoeberl, J. M. Rodriquez, and Y. Yoshida, "Interannual variability of ozone in the winter lower stratosphere and the relationship to lamina and irreversible transport," *J. Geophys. Res.*, vol. 115, D15305, 2010.

[10] L. L. Pan, W. J. Randel, J. C. Gille, W. D. Hall, B. Nardi, S. Massie, V. Yudin, R. Khosravi, P. Konopka, and D. Tarasick, "Tropospheric intrusions associated with the secondary tropopause," *J. Geophys. Res.*, vol. 114, D10302, 2009.

[11] L. L. Pan, K. P. Bowman, E. L. Atlas, S. C. Wofsy, F. Zhang, J. F. Bresch, B. A. Ridley, J. V. Pittman, C. R. Homeyer, P. Romashkin, and W. A. Cooper, "The Stratosphere-Troposphere Analyses of Regional Transport 2008 experiment," *Bull. Am. Meteorol. Soc.*, vol. 91, pp. 327–342, 2010.

[12] G. M. B. Dobson, "The laminated structure of the ozone in the atmosphere," *Q. J. R. Meteorol. Soc.*, vol. 99, no. 422, pp. 599–607, 1973.

[13] M. E. McIntyre and T. N. Palmer, "Breaking planetary waves in the stratosphere," *Nature*, vol. 305, no. 13, pp. 593–600, 1983.

[14] P. A. Newman and M. R. Schoeberl, "A reinterpretation of the data from the NASA stratosphere-troposphere exchange project," *Geophys. Res. Lett.*, vol. 22, no. 18, pp. 2501–2504, 1995.

[15] G. Vaughan and C. Timmis, "Transport of near-tropopause air into the lower

midlatitude stratosphere," *Q. J. R. Meteorol. Soc.*, vol. 124, pp. 1559–1578, 1998.

[16] F. M. O'Connor, G. Vaughan, and H. De Backer, "Observations of subtropical air in the European mid-latitude lower stratosphere," *Q. J. R. Meteorol. Soc.*, vol. 125, pp. 2965–2986, 1999.

[17] N. G. Bradshaw, G. Vaughan, R. Busen, S. Garcelon, R. Jones, T. Gardiner, and J. Hacker, "Tracer filamentation generated by small-scale Rossby wave breaking in the lower stratosphere," *J. Geophys. Res.*, vol. 107, no. D23, 4689, 2002.

[18] D. W. Waugh and L. M. Polvani, "Climatology of intrusions into the tropical upper troposphere," *Geophys. Res. Lett.*, vol. 27, no. 23, pp. 3857 – 3860, 2000.

[19] D. W. Waugh, "Impact of potential vorticity intrusions on subtropical upper tropospheric humidity," *J. Geophys. Res.*, vol. 110, D11305, 2005.

[20] G. A. Postel and M. H. Hitchman, "A climatology of Rossby wave breaking along the subtropical tropopause," *J. Atmos. Sci.*, vol. 56, pp. 359–373, 1999.

[21] H. Wernli and M. Sprenger, "Identification and ERA-15 climatology of potential vorticity streamers and cutoffs near the extratropical tropopause," *J. Atmos. Sci.*, vol. 64, pp. 1569–1586, 2007.

[22] O. Martius, C. Schwierz, and H. C. Davies, "Breaking waves at the tropopause in the wintertime northern hemisphere: Climatological analyses of the orientation and the theoretical LC1/2 classification," *J. Atmos. Sci.*, vol. 64, pp. 2576–2592, 2007.

[23] J. Song, C. Li, J. Pan, and W. Zhou, "Climatology of anticyclonic and cyclonic Rossby wave breaking on the dynamical tropopause in the southern hemisphere," *J. Clim.*, vol. 24, pp. 1239–1251, 2011.

[24] C. D. Thorncroft, B. J. Hoskins, and M. E. McIntyre, "Two paradigms of baroclinic-wave life-cycle behaviour," *Q. J. R. Meteorol. Soc.*, vol. 119, pp. 17–55, 1993.

[25] D. Peters and D. W. Waugh, "Influence of barotropic shear on the poleward advection of upper-tropospheric air," *J. Atmos. Sci.*, vol. 53, no. 21, pp. 3013–3031, 1996.

[26] A. Gabriel and D. Peters, "A diagnostic study of different types of Rossby wave breaking events in the northern extratropics," *J. Meteorol. Soc. Japan*, vol. 86, no. 5, pp. 613–631, 2008.

[27] T. Ndarana and D. W. Waugh, "A climatology of Rossby wave breaking along the southern hemisphere tropopause," *J. Atmos. Sci.*, vol. 68, pp. 798–811, 2011.

[28] M. Nakamura and R. A. Plumb, "The effects of flow asymmetry on the direction of Rossby wave breaking," *J. Atmos. Sci.*, vol. 51, no. 14, pp. 2031–2045, 1994.

[29] M. H. Hitchman and A. S. Huesmann, "A seasonal climatology of Rossby wave breaking in the 320–2000-K layer," *J. Atmos. Sci.*, vol. 64, pp. 1922–1940, 2007.

[30] D. P. Dee, S. M. Uppala, A. J. Simmons, P. Berrisford, P. Poli, S. Kobayashi, U. Andrae, M. A. Balmaseda, G. Balsamo, P. Bauer, P. Bechtold, A. C. M. Beljaars, L. van de Berg, J. Bidlot, N. Bormann, C. Delsol, R. Dragani, M. Fuentes, A. J. Geer, L. Haimberger, S. B. Healy, H. Hersbach, E. V. Hólm, L. Isaksen,

P. Kållberg, M. Köhler, M. Matricardi, A. P. McNally, B. M. Monge-Sanz, J.-J. Morcrette, B.-K. Park, C. Peubey, P. de Rosnay, C. Tavolato, J.-N. Thépaut, and F. Vitart, "The ERA-Interim reanalysis: configuration and performance of the data assimilation system," *Q. J. R. Meteorol. Soc.*, vol. 137, pp. 553–597, 2011.

[31] P. J. Webster and J. R. Holton, "Cross-equatorial response to middle-latitude forcing in a zonally varying basic state," *J. Atmos. Sci.*, vol. 39, pp. 722–733, 1982.

[32] A. J. Matthews and G. N. Kiladis, "Interactions between ENSO, transient circulation, and tropical convection over the Pacific," *J. Clim.*, vol. 12, pp. 3062–3086, 1999.

[33] T. Horinouchi, F. Sassi, and B. A. Boville, "Synoptic-scale Rossby waves and the geographic distribution of lateral transport routes between the tropics and extratropics in the lower stratosphere," *J. Geophys. Res.*, vol. 105, no. D21, pp. 26579–26592, 2000.

[34] R. K. Scott and J.-P. Cammas, "Wave breaking and mixing at the subtropical tropopause," *J. Atmos. Sci.*, vol. 59, pp. 2347–2361, 2002.

[35] P. Chen, J. R. Holton, A. O'Neill, and R. Swinbank, "Isentropic mass exchange between the tropics and extratropics in the stratosphere," *J. Atmos. Sci.*, vol. 51, no. 20, pp. 3006–3018, 1994.

[36] D. W. Waugh, "Seasonal variation of isentropic transport out of the tropical stratosphere," *J. Geophys. Res.*, vol. 101, no. D2, pp. 4007–4023, 1996.

[37] A. Dethof, A. O'Neill, and J. Slingo, "Quantification of the isentropic mass

transport across the dynamical tropopause," *J. Geophys. Res.*, vol. 105, no. D10, pp. 12279–12293, 2000.

[38] K.-H. Seo and K. P. Bowman, "A climatology of isentropic cross-tropopause exchange," *J. Geophys. Res.*, vol. 106, no. D22, pp. 28,159–28,172, 2001.

[39] P. Jing, D. M. Cunnold, E.-S. Yang, and H.-J. Wang, "Influence of isentropic transport on seasonal ozone variations in the lower stratosphere and subtropical upper troposphere," *J. Geophys. Res.*, vol. 110, D10110, 2005.

[40] N. Nakamura, "Extratropical stratosphere-troposphere mass exchange associated with isentropic mixing: A 1992–2005 climatology derived from advection-diffusion calculations," *J. Geophys. Res.*, vol. 112, D24303, 2007.

[41] L. L. Pan, W. J. Randel, B. L. Gary, M. J. Mahoney, and E. J. Hintsa, "Definitions and sharpness of the extratropical tropopause: A trace gas perspective," *J. Geophys. Res.*, vol. 109, D23103, 2004.

[42] M. I. Hegglin, C. D. Boone, G. L. Manney, and K. A. Walker, "A global view of the extratropical tropopause transition layer from atmospheric chemistry experiment fourier transform spectrometer o-3, h2o, and co," *J. Geophys. Res.*, vol. 114, D00B11, 2009.

[43] E. F. Danielsen, "Stratospheric-tropospheric exchange based on radioactivity, ozone and potential vorticity," *J. Atmos. Sci.*, vol. 25, pp. 502–518, 1968.

[44] M. A. Shapiro, "Turbulent mixing within tropopause folds as a mechanism for the exchange of chemical constituents between the stratosphere and troposphere," *J. Atmos. Sci.*, vol. 37, pp. 994–1004, 1980.

[45] E. V. Browell, E. F. Danielsen, S. Ismail, G. L. Gregory, and S. M. Beck, "Tropopause fold structure determined from airborne lidar in situ measurements," *J. Geophys. Res.*, vol. 92, no. D2, pp. 2112–2120, 1987.

[46] C. Appenzeller and H. C. Davies, "Structure of stratospheric intrusions into the troposphere," *Nature*, vol. 358, pp. 570–572, 1992.

[47] C. Appenzeller, H. C. Davies, and W. A. Norton, "Fragmentation of stratospheric intrusions," *J. Geophys. Res.*, vol. 101, no. D1, pp. 1435–1456, 1996.

[48] O. Cooper, C. Forster, D. Parrish, E. Dunlea, G. Hübler, F. Fehsenfeld, J. Holloway, S. Oltmans, B. Johnson, A. Wimmers, and L. Horowitz, "On the life cycle of a stratospheric intrusion and its dispersion into polluted warm conveyor belts," *J. Geophys. Res.*, vol. 109, D23S09, 2004.

[49] L. L. Pan, K. P. Bowman, M. Shapiro, W. J. Randel, R. S. Gao, T. Campos, C. Davis, S. Schauffler, B. A. Ridley, J. C. Wei, and C. Barnet, "Chemical behavior of the tropopause observed during the stratosphere-troposphere analyses of regional transport experiment," *J. Geophys. Res.*, vol. 112, D18110, 2007.

[50] M. A. Shapiro, "The role of turbulent heat flux in the generation of potential vorticity in the vicinity of upper-level jet stream systems," *Mon. Wea. Rev.*, vol. 104, pp. 892–906, 1976.

[51] M. A. Shapiro, "Further evidence of the mesoscale and turbulent structure of upper level jet stream-frontal zone systems," *Mon. Wea. Rev.*, vol. 106, pp. 1100–1111, 1978.

[52] E. F. Danielsen, R. S. Hipskind, W. L. Starr, J. F. Vedder, S. E. Gaines, D. Kley, and K. K. Kelly, "Irreversible transport in the stratosphere by internal waves of

short vertical wavelength," *J. Geophys. Res.*, vol. 96, no. D9, pp. 17,433–17,452, 1991.

[53] W. B. Johnson and W. Viezee, "Stratospheric ozone in the lower troposphere -i. presentation and interpretation of aircraft measurements," *Atmos. Environ.*, vol. 15, no. 7, pp. 1309–1323, 1981.

[54] J. D. Price and G. Vaughan, "The potential for stratosphere-troposphere exchange in cut-off-low systems," *Q. J. R. Meteorol. Soc.*, vol. 119, pp. 343–365, 1993.

[55] J.-F. Lamarque and P. G. Hess, "Cross-tropopause mass exchange and potential vorticity budget in a simulated tropopause folding," *J. Atmos. Sci.*, vol. 51, no. 15, pp. 2246–2269, 1994.

[56] A. O. Langford and S. J. Reid, "Dissipation and mixing of a small-scale stratospheric intrusion in the upper troposphere," *J. Geophys. Res.*, vol. 103, no. D23, pp. 31,265–31276, 1998.

[57] H. J. Reid and G. Vaughan, "Convective mixing in a tropopause fold," *Q. J. R. Meteorol. Soc.*, vol. 130, pp. 1195–1212, 2004.

[58] O. R. Cooper, A. Stohl, G. Hübler, E. Y. Hsie, D. D. Parrish, A. F. Tuck, G. N. Kiladis, S. J. Oltmans, B. J. Johnson, M. Shapiro, J. L. Moody, and A. S. Lefohn, "Direct transport of midlatitude stratospheric ozone into the lower troposphere and marine boundary layer of the tropical Pacific Ocean," *J. Geophys. Res.*, vol. 110, D23310, 2005.

[59] M. A. Olsen, A. R. Douglass, and M. R. Schoeberl, "Estimating downward

cross-tropopause ozone flux using column ozone and potential vorticity," *J. Geophys. Res.*, vol. 107, no. D22, 4636, 2002.

[60] H. Wernli and M. Bourqui, "A Lagrangian "1-year climatology" of (deep) cross-tropopause exchange in the extratropical Northern Hemisphere," *J. Geophys. Res.*, vol. 107, no. D2, 4021, 2002.

[61] M. Sprenger and H. Wernli, "A northern hemispheric climatology of cross-tropopause exchange for the ERA15 time period (1979–1993)," *J. Geophys. Res.*, vol. 108, no. D12, 8521, 2003.

[62] M. Sprenger, M. C. Maspoli, and H. Wernli, "Tropopause folds and cross-tropopause exchange: A global investigation based upon ECMWF analyses for the time period March 2000 to February 2001," *J. Geophys. Res.*, vol. 108, no. D12, 8518, 2003.

[63] F. Sanders and J. R. Gyakum, "Synoptic-dynamic climatology of the "bomb"," *Mon. Wea. Rev.*, vol. 108, pp. 1589–1606, 1980.

[64] P. J. Roebber, "Statistical analysis and updated climatology of explosive cyclones," *Mon. Wea. Rev.*, vol. 112, pp. 1577–1589, 1984.

[65] D. Keyser and M. A. Shapiro, "A review of the structure and dynamics of upper-level fronal zones," *Mon. Wea. Rev.*, vol. 114, pp. 452–499, 1986.

[66] M. A. Shapiro, "Frontogenesis and geostrophically forced secondary circulations in the vicinity of jet stream-frontal zone systems," *J. Atmos. Sci.*, vol. 38, pp. 954–973, 1981.

[67] D. Keyser and M. J. Pecnick, "Diagnosis of ageostropic circulations in a two-

dimensional primitive equation model of frontogenesis," *J. Atmos. Sci.*, vol. 42, no. 12, pp. 1283–1305, 1985.

[68] D. Keyser and M. J. Pecnick, "A two-dimensional primitive equation model of frontogenesis forced by confluence and horizontal shear," *J. Atmos. Sci.*, vol. 42, no. 12, pp. 1259–1282, 1985.

[69] M. J. Reeder and D. Keyser, "Balanced and unbalanced upper-level frontogenesis," *J. Atmos. Sci.*, vol. 45, no. 22, pp. 3366–3386, 1988.

[70] J. S. Sawyer, "The vertical circulation at meteorological fronts and its relation to frontogenesis," *Proc. Roy. Soc. London*, vol. A234, pp. 346–362, 1956.

[71] A. Eliassen, "On the vertical circulation in frontal zones," *Geofys. Publ.*, vol. 24, pp. 147–160, 1962.

[72] O. Poulida, R. R. Dickerson, and A. Heymsfield, "Stratosphere-troposphere exchange in a midlatitude mesoscale convective complex," *J. Geophys. Res.*, vol. 101, no. D3, pp. 6823–6836, 1996.

[73] H. Fischer, M. de Reus, M. Traub, J. Williams, J. Lelieveld, J. de Gouw, C. Warneke, H. Schlager, A. Minikin, R. Scheele, and P. Siegmund, "Deep convective injection of boundary layer air into the lowermost stratosphere at midlatitudes," *Atmos. Chem. Phys.*, vol. 3, no. 3, pp. 739–745, 2003.

[74] P. K. Wang, "Moisture plumes above thunderstorm anvils and their contributions to cross-tropopause transport of water vapor in midlatitudes," *J. Geophys. Res.*, vol. 108, no. D6, 4194, 2003.

[75] M. I. Hegglin, D. Brunner, H. Wernli, C. Schwierz, O. Martius, P. Hoor, H. Fischer, U. Parchatka, N. Spelten, C. Schiller, M. Krebsbach, U. Weers, J. Stae-

helin, and Th. Peter, "Tracing troposphere-to-stratosphere transport above a mid-latitude deep convective system," *Atmos. Chem. Phys.*, vol. 4, no. 3, pp. 741—756, 2004.

[76] E. A. Ray, K. H. Rosenlof, E. C. Richard, P. K. Hudson, D. J. Cziczo, M. Loewenstein, H.-J. Jost, J. Lopez, B. Ridley, A. Weinheimer, D. Montzka, D. Knapp, S. C. Wofsy, B. C. Daube, C. Gerbig, I. Xueref, and R. L. Herman, "Evidence of the effect of summertime midlatitude convection on the subtropical lower stratosphere from CRYSTAL-FACE tracer measurements," *J. Geophys. Res.*, vol. 109, D18304, 2004.

[77] M. Setvák, D. T. Lindsey, R. M. Rabin, P. K. Wang, and A. Demeterová, "Indication of water vapor transport into the lower stratosphere above midlatitude convective storms: Meteosat Second Generation satellite observations and radiative transfer model simulations," *Atmos. Res.*, vol. 89, pp. 170–180, 2008.

[78] K. Bedka, J. Brunner, R. Dworak, W. Feltz, J. Otkin, and T. Greenwald, "Objective satellite-based detection of overshooting tops using infrared window channel brightness temperature gradients," *J. App. Met. Clim.*, vol. 49, pp. 181–202, 2009.

[79] L. L. Pan and L. A. Munchak, "The relationship of cloud top to the tropopause/jet structure from CALIPSO data," *J. Geophys. Res.*, vol. 116, D12201, 2011.

[80] World Meteorological Organization, "Meteorology—a three-dimensional science: Second session of the commission for aerology," *World Meteorol. Organ. Bull.*, vol. 4, pp. 134–138, 1957.

[81] C. R. Homeyer, K. P. Bowman, and L. L. Pan, "Extratropical tropopause transition layer characteristics from high-resolution sounding data," *J. Geophys. Res.*, vol. 115, D13108, 2010.

[82] M. H. Proffitt and R. J. McLaughlin, "Fast-response dual-beam UV-absorption ozone photometer suitable for use on stratospheric balloons," *Rev. Sci. Instrum.*, vol. 54, no. 12, pp. 1719–1728, 1983.

[83] C. Gerbig, S. Schmitgen, D. Kley, A. Volz-Thomas, K. Dewey, and D. Haaks, "An improved fast-response vacuum-UV resonance fluorescence CO instrument," *J. Geophys. Res.*, vol. 104, no. D1, pp. 1699–1704, 1999.

[84] M. A. Zondlo, M. E. Paige, S. M. Massick, and J. A. Silver, "Vertical cavity laser hygrometer for the National Science Foundation Gulfstream-V aircraft," *J. Geophys. Res.*, vol. 115, D20309, 2010.

[85] T. D. Crum and R. L. Alberty, "The WSR-88D and the WSR-88D operational support facility," *Bull. Am. Meteorol. Soc.*, vol. 74, no. 9, pp. 1669–1687, 1993.

[86] K. P. Bowman, L. L. Pan, T. Campos, and R. Gao, "Observations of fine-scale transport structure in the upper troposphere from the High-performance Instrumented Airborne Platform for Environmental Research," *J. Geophys. Res.*, vol. 112, D18111, 2007.

[87] K. P. Bowman, "Large-scale isentropic mixing properties of the Antarctic polar vortex from analyzed winds," *J. Geophys. Res.*, vol. 98, no. D12, pp. 23013–23027, 1993.

[88] K. P. Bowman and G. D. Carrie, "The mean-meridional transport circulation of

the troposphere in an idealized GCM," *J. Atmos. Sci.*, vol. 59, pp. 1502–1514, 2002.

[89] K. Minschwaner, A. E. Dessler, J. W. Elkins, C. M. Volk, D. W. Fahey, M. Loewenstein, J. R. Podolske, A. E. Roche, and K. R. Chan, "Bulk properties of isentropic mixing into the tropics in the lower stratosphere," *J. Geophys. Res.*, vol. 101, no. D5, pp. 9433–9439, 1996.

[90] C. M. Volk, J. W. Elkins, D. W. Fahey, R. J. Salawitch, G. S. Dutton, J. M. Gilligan, M. H. Proffitt, M. Loewenstein, J. R. Podolske, K. Minschwaner, J. J. Margitan, and K. R. Chan, "Quantifying transport between the tropical and mid-latitude lower stratosphere," *Science*, vol. 272, no. 5269, pp. 1763–1768, 1996.

[91] F. Flocke, R. L. Herman, R. J. Salawitch, E. Atlas, C. R. Webster, S. M. Schauffler, R. A. Lueb, R. D. May, E. J. Moyer, K. H. Rosenlof, D. C. Scott, D. R. Blake, and T. P. Bui, "An examination of chemistry and transport processes in the tropical lower stratosphere using observations of long-lived and short-lived compounds obtained during STRAT and POLARIS," *J. Geophys. Res.*, vol. 104, no. D21, pp. 26625–26642, 1999.

[92] N. J. Warwick, J. A. Pyle, G. D. Carver, X. Yang, N. H. Savage, F. M. O'Connor, and R. A. Cox, "Global modeling of biogenic bromocarbons," *J. Geophys. Res.*, vol. 111, D24305, 2006.

[93] C. B. Markwardt, "Non-linear least squares fitting in idl with mpfit," in *Astronomical Data Analysis Software and Systems (ADASS) XVIII*, D. Bohlender, P. Dowler, and D. Durand, Eds. Astron. Soc. Pac., San Francisco, Calif., 2009, vol. 411 of *Astron. Soc. Pac. Conf. Ser.*, pp. 251–254.

[94] D. J. Seidel and W. J. Randel, "Recent widening of the tropical belt: Evidence from tropopause observations," *J. Geophys. Res.*, vol. 112, D20113, 2007.

[95] T. Birner, "Recent widening of the tropical belt from global tropopause statistics: Sensitivites," *J. Geophys. Res.*, vol. 115, D23109, 2010.

[96] W. J. Randel, D. J. Seidel, and L. L. Pan, "Observational characterisitics of double tropopauses," *J. Geophys. Res.*, vol. 112, D07309, 2007.

[97] J. M. Castanheira and L. Gimeno, "Association of double tropopause events with baroclinic waves," *J. Geophys. Res.*, vol. 116, D19113, 2011.

[98] A. Kunz, P. Konopka, R. Müller, and L. L. Pan, "Dynamical tropopause based on isentropic potential vorticity gradients," *J. Geophys. Res.*, vol. 116, D01110, 2011.

[99] J. G. Esler and P. H. Haynes, "Baroclinic wave breaking an the internal variability of the tropospheric circulation," *J. Atmos. Sci.*, vol. 56, pp. 4014–4031, 1999.

[100] B. J. Hoskins, M. E. McIntyre, and A. W. Robertson, "On the use and significance of isentropic potential vorticity maps," *Q. J. R. Meteorol. Soc.*, vol. 111, no. 470, pp. 877–946, 1985.

[101] R. T. Sutton, H. Maclean, R. Swinbank, A. O'Neill, and F. W. Taylor, "High-resolution stratospheric tracer fields estimated from satellite observations using Lagrangian trajectory calculations," *J. Atmos. Sci.*, vol. 51, no. 20, pp. 2995–3005, 1994.

[102] T. Birner, A. Dörnbrack, and U. Schumann, "How sharp is the tropopause at midlatitudes?," *Geophys. Res. Lett.*, vol. 29, no. 14, 1700, 2002.

[103] T. Birner, "Fine-scale structure of the extratropical tropopause," *J. Geophys. Res.*, vol. 111, D04104, 2006.

[104] T. Birner, "Residual circulation and tropopause structure," *J. Atmos. Sci.*, vol. 67, pp. 2582–2600, 2010.

[105] S. Bethan, G. Vaughan, and S. J. Reid, "A comparison of ozone and thermal tropopause heights and the impact of tropopause definition on quantifying the ozone content of the troposphere," *Q. J. R. Meteorol. Soc.*, vol. 122, pp. 929–944, 1996.

[106] V. Wirth, "Static stability in the extratropical tropopause region," *J. Atmos. Sci.*, vol. 60, pp. 1395–1409, 2003.

[107] W. J. Randel, F. Wu, and P. Forster, "The extratropical tropopause inversion layer: Global observations with GPS data, and a radiative forcing mechanism," *J. Atmos. Sci.*, vol. 64, pp. 4489–4496, 2007.

[108] E. Palmén, "On the distribution of temperature and wind in the upper westerlies," *J. Meteorol.*, vol. 5, pp. 20–27, 1948.

[109] E. F. Danielsen, "The laminar structure of the atmosphere and its relation to the concept of a tropopause," *Arch. Meteorol. Geophys. Bioklimatol., Ser. A*, vol. 11, pp. 293–332, 1959.

[110] H. Fischer, F. G. Wienhold, P. Hoor, O. Bujok, C. Schiller, P. Siegmund, M. Ambaum, H. A. Scheeren, and J. Lelieveld, "Tracer correlations in the northern high latitude lowermost stratosphere: Influence of cross-tropopause mass exchange," *Geophys. Res. Lett.*, vol. 27, no. 1, pp. 97–100, 2000.

[111] P. Hoor, H. Fischer, L. Lange, J. Lelieveld, and D. Brunner, "Seasonal variations of a mixing layer in the lowermost stratosphere as identified by the CO-O3 correlation from in situ measurements," *J. Geophys. Res.*, vol. 107, no. D5, 4044, 2002.

[112] A. F. Tuck, D. Baumgardner, K. Chan, J. E. Dye, J. W. Elkins, S. J. Hovde, K. K. Kelly, M. Loewenstein, J. J. Margitan, R. D. May, J. R. Podolske, M. H. Proffitt, K. H. Rosenlof, W. L. Smith, C. R. Webster, and J. C. Wilson, "The Brewer-Dobson circulation in the light of high altitude *in situ* aircraft observations," *Q. J. R. Meteorol. Soc.*, vol. 123, no. 537, pp. 1–69, 1997.

[113] S. Fueglistaler, A. E. Dessler, T. J. Dunkerton, I. Folkins, Q. Fu, and P. W. Mote, "Tropical tropopause layer," *Rev. Geophys.*, vol. 47, RG1004, 2009.

[114] D. J. Seidel, R. J. Ross, J. K. Angell, and G. C. Reid, "Climatological characteristics of the tropical tropopause as revealed by radiosondes," *J. Geophys. Res.*, vol. 106, no. D8, pp. 7857–7878, 2001.

[115] I. Folkins, M. Loewenstein, J. Podolske, S. J. Oltmans, and M. Proffitt, "A barrier to vertical mixing at 14 km in the tropics: Evidence from ozonesondes and aircraft measurements," *J. Geophys. Res.*, vol. 104, no. D18, pp. 22095–22102, 1999.

[116] R. Allan and T. Ansell, "A new globally complete monthly Historical Gridded Mean Sea Level Pressure dataset (HadSLP2): 1850–2004," *J. Clim.*, vol. 19, pp. 5816–5842, 2006.

[117] V. Eyring, N. R. P. Harris, M. Rex, T. G. Shepherd, D. W. Fahey, G. T. Amanatdis, J. Austin, M. P. Chipperfield, M. Dameris, P. M. De F. Forster,

A. Gettelman, H. F. Graf, T. Nagashima, P. A. Newman, S. Pawson, M. J. Prather, J. A. Pyle, R. J. Salawitch, B. D. Santer, and D. W. Waugh, "A strategy for process-oriented validation of coupled chemistry-climate models," *Bull. Am. Meteorol. Soc.*, vol. 86, no. 8, pp. 1117–1133, 2005.

[118] G. A. Postel and M. H. Hitchman, "A case study of Rossby wave breaking along the subtropical tropopause," *Mon. Wea. Rev.*, vol. 129, pp. 2555–2569, 2001.

[119] S. Lee and H-K. Kim, "The dynamical relationship between subtropical and eddy-driven jets," *J. Atmos. Sci.*, vol. 60, pp. 1490–1503, 2003.

[120] C. Yoo and S. Lee, "Persistent multiple jets and PV staircase," *J. Atmos. Sci.*, vol. 67, pp. 2279–2295, 2010.

[121] A. Gettelman, P. Hoor, L. L. Pan, W. J. Randel, M. I. Hegglin, and T. Birner, "The extratropical upper troposphere and lower stratosphere," *Rev. Geophys.*, vol. 49, RG3003, 2011.

[122] C. W. Newton, "Dynamics of severe convective storms," *Meteorol. Monogr.*, vol. 5, no. 27, pp. 33–58, 1963.

[123] M. A. Shapiro, "Mesoscale weather systems of the central United States. *The National STORM Program: Scientific and Technological Bases and Major Objectives*," Tech. Rep. 3.1–3.77, R. A. Anthes, Ed., University Corporation for Atmospheric Research, P.O. Box 3000, Boulder, Colorado 80307, August 1982.

[124] K. A. Browning and G. A. Monk, "A simple model for the synoptic analysis of cold fronts," *Q. J. R. Meteorol. Soc.*, vol. 108, pp. 435–452, 1982.

[125] D. M. Schultz and G. Vaughan, "Occluded fronts and the occlusion process: A fresh look at conventional wisdom," *Bull. Am. Meteorol. Soc.*, vol. 92, no. 4, pp. 443–466, 2011.

[126] M. Griffiths, A. J. Thorpe, and K. A. Browning, "Convective destabilization by a tropopause fold diagnosed using potential-vorticity inversion," *Q. J. R. Meteorol. Soc.*, vol. 126, pp. 125–144, 2000.

[127] S. L. Gray, "A case study of stratosphere to troposphere transport: The role of convective transport and the sensitivity to model resolution," *J. Geophys. Res.*, vol. 108, no. D18, 4590, 2003.

[128] Q. Tang, M. J. Prather, and J. Hsu, "Stratosphere-troposphere exchange ozone flux related to deep convection," *Geophys. Res. Lett.*, vol. 38, L03806, 2011.

APPENDIX A

Table I. AWAS Trace Constituents Used in the Analysis, Their Lifetimes and Destruction (Loss) Processes Considered, and Estimates of Measurement Precision and Uncertainty. The tropospheric and stratospheric photochemical lifetimes are given by τ_t and τ_s, respectively. Lifetimes are given using Jet Propulsion Laboratory (JPL) recommendations for reaction rates [1]. We use $[\mathrm{OH}] = 10^6$ molecules cm^{-3}, $[\mathrm{Cl}] = 10^3$ molecules cm^{-3} and $\mathrm{T} = 223$ K when approximating stratospheric lifetimes and $\mathrm{T} = 253$ K for tropospheric lifetimes. Absolute error is applied in addition to measurement uncertainty when values get near the limits of detection.

Name	Formula	τ_t (weeks)	τ_s (weeks)	Loss	Precision	Uncertainty (%)	Abs Error (%)
3 Pentyl Nitrate	$C_5H_{11}ONO_2$	1	<1	OH + hν	0.1 ppt	±5	10
2 Butyl Nitrate	$C_4H_9ONO_2$	1	1	OH + hν	0.1 ppt	±5	10
Isobutane	i-C_4H_{10}	1	1	OH + Cl	1 ppt	±5	10
Benzene	C_6H_6	2	2	OH + Cl	2 ppt	±5	10
Ethyne	C_2H_2	3	4	OH + Cl	2 ppt	±5	10
Methyl Nitrate	CH_3ONO_2	4	5–7	hν	0.2 ppt	±5	10
Bromoform	$CHBr_3$	5	4–6	hν	0.1 ppt	±10	15
Carbon Monoxide	CO	8	12	OH	5 ppb	±5	10
Ethane	C_2H_6	10	15	OH + Cl	2 ppt	±3	5
Methylene Chloride	CH_2Cl_2	15	42	OH + Cl	0.5 ppt	±5	10
Chloroform	$CHCl_3$	20	45	OH + Cl	0.5 ppt	±5	10

Table II. Number of Observations Used for and Parameters Given by the Box Model Curve Fit

Flight	n_int	n_trop	t_t (weeks)	τ_m (weeks)	$\tau_\mathrm{m}((t_\mathrm{t}-1)>0)$ (weeks)	$\tau_\mathrm{m}(t_\mathrm{t}+1)$ (weeks)
RF01	9	8	0.38	0.73	0.67	0.86
RF14	8	21	1.43	0.84	0.65	1.05

Table III. Number and Mean Latitude ($\bar{\phi}$) of Wavebreaking Events Contributing to the Transport Mode Composites at 380 K in Figure 24

| | NH | | | SH | | |
	T→E	E→T	both	T→E	E→T	both
#	348	676	615	494	659	706
# yr^{-1}	11.6	22.5	20.5	16.5	22.0	23.5
$\bar{\phi}$	41.34	30.72	35.40	−38.21	−30.06	−33.95

APPENDIX B
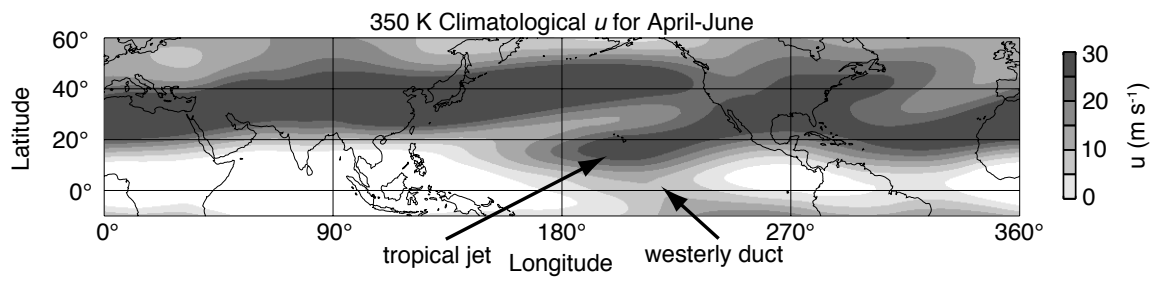
Fig. 1. Climatological mean zonal wind speed (u) on the 350 K potential temperature surface from the ERA-Interim reanalysis for April to June 1981–2010. White areas represent regions of climatological mean easterlies.
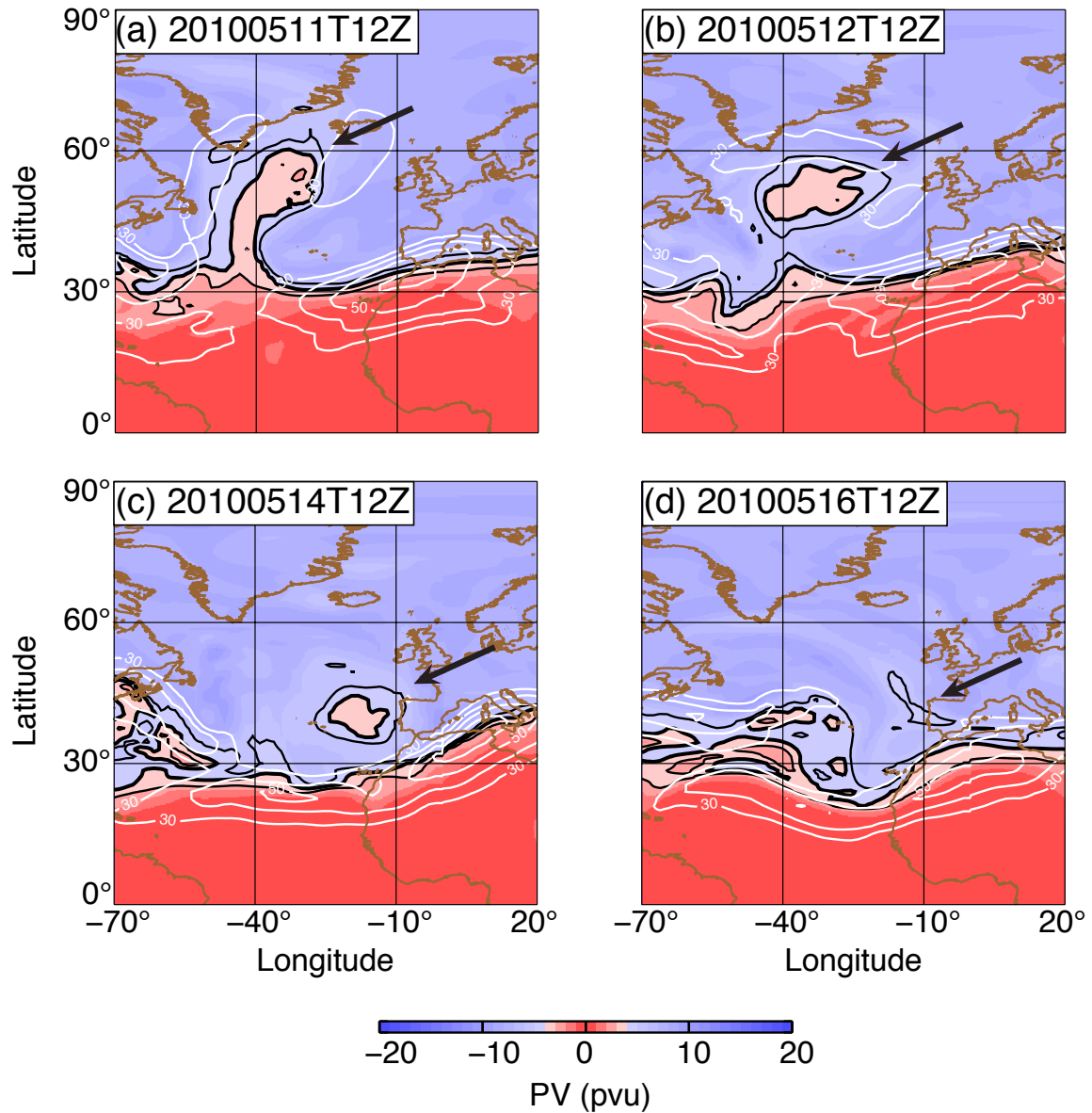
Fig. 2. Evolution of a Rossby wavebreaking event on the 350 K potential temperature surface from the ERA-Interim reanalysis valid (a) 11 May 2010 at 12 UTC, (b) 12 May 2010 at 12 UTC, (c) 14 May 2010 at 12 UTC, and (d) 16 May 2010 at 12 UTC. Red colors represent |PV| < 4 pvu (tropical air), the black contours represent PV values of 3, 4 (thick) and 5 pvu, and the white contours show wind speed (m/s). Black arrows identify the transported air mass at each analysis time.
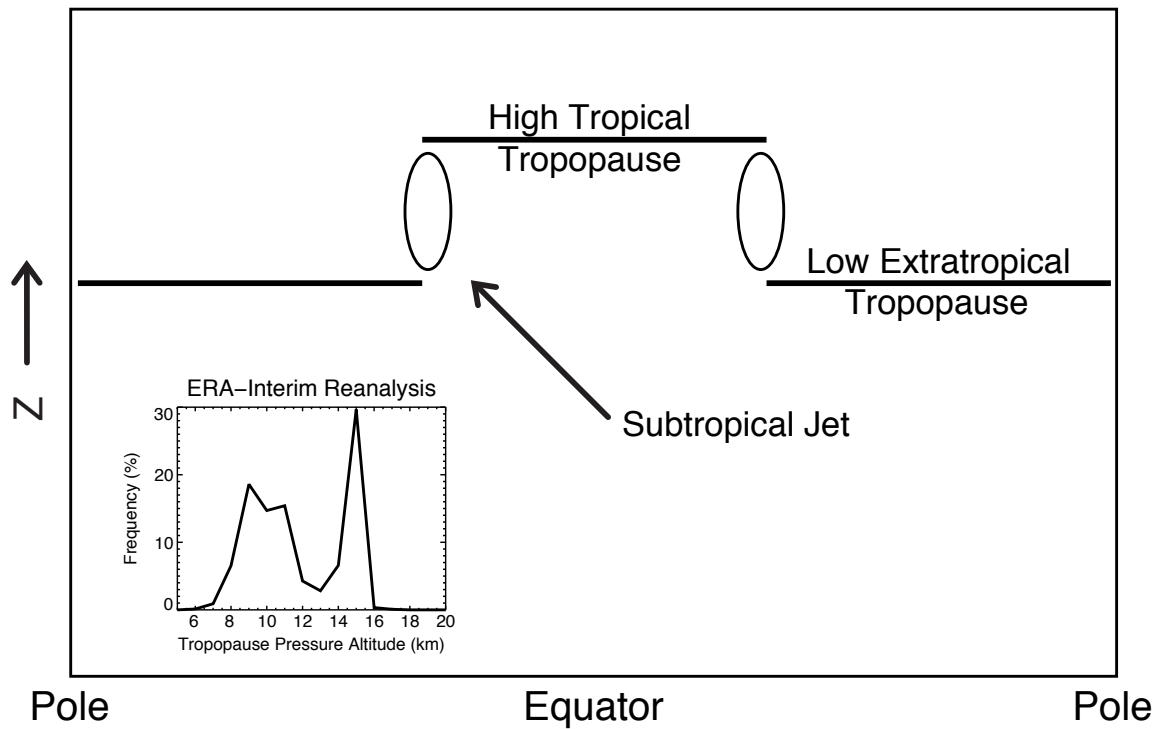
Fig. 3. A representation of the meridional "break" in the tropopause between tropics and extratropics near the subtropical jet. Lower left: global frequency distribution of pressure altitudes of the tropopause from 30 years of ERA-Interim reanalysis data (1981–2010).
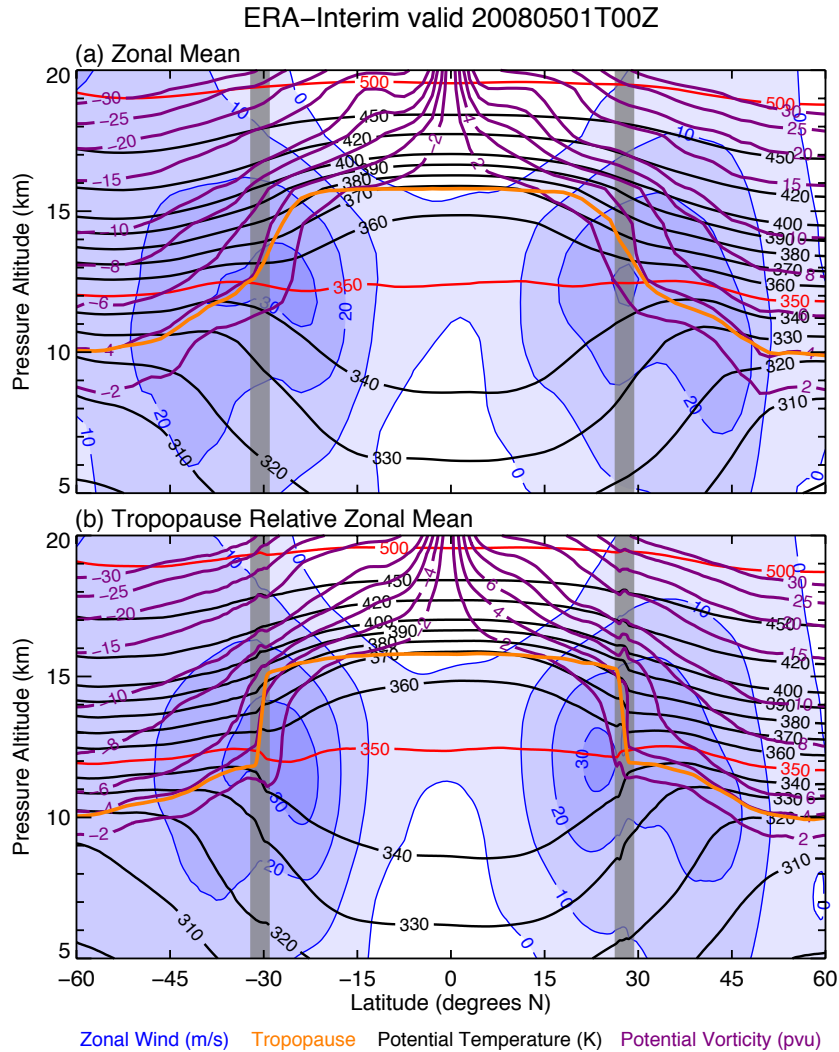
Fig. 4. Zonal mean zonal wind (m/s, color-fill), potential temperature (K, black and red lines), potential vorticity (purple lines), and tropopause altitude (orange line) for the (a) pressure altitude vertical coordinate and (b) tropopause-relative vertical and tropopause break-relative horizontal coordinates from the ERA-Interim reanalysis valid 1 May 2008 at 00 UTC. The mean latitude of the tropopause break, taken as the global 13 km tropopause altitude contour, is shown as the thick gray vertical lines in each hemisphere. The width of these gray lines corresponds to tropopause break latitude $\pm 1.5°$ (the reanalysis horizontal grid resolution).
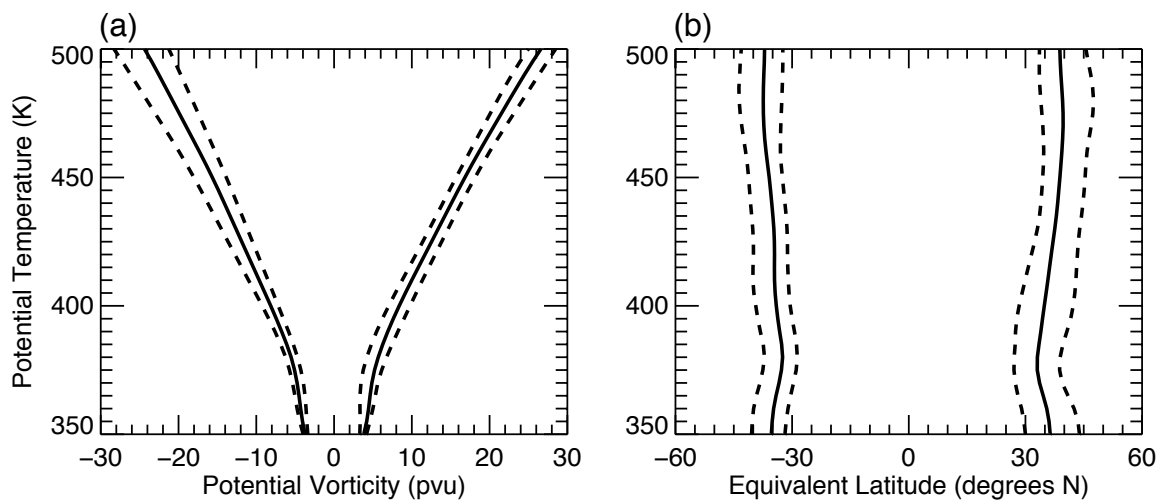
Fig. 5. ERA-Interim annual mean (solid lines), minimum, and maximum (dashed lines) (a) potential vorticity and (b) equivalent latitude at the tropopause break ($Z_{trop} = 13$ km) from 30-year climatological monthly means (1981–2010). Profiles of negative magnitudes represent the southern hemisphere and positive magnitudes, the northern hemisphere.
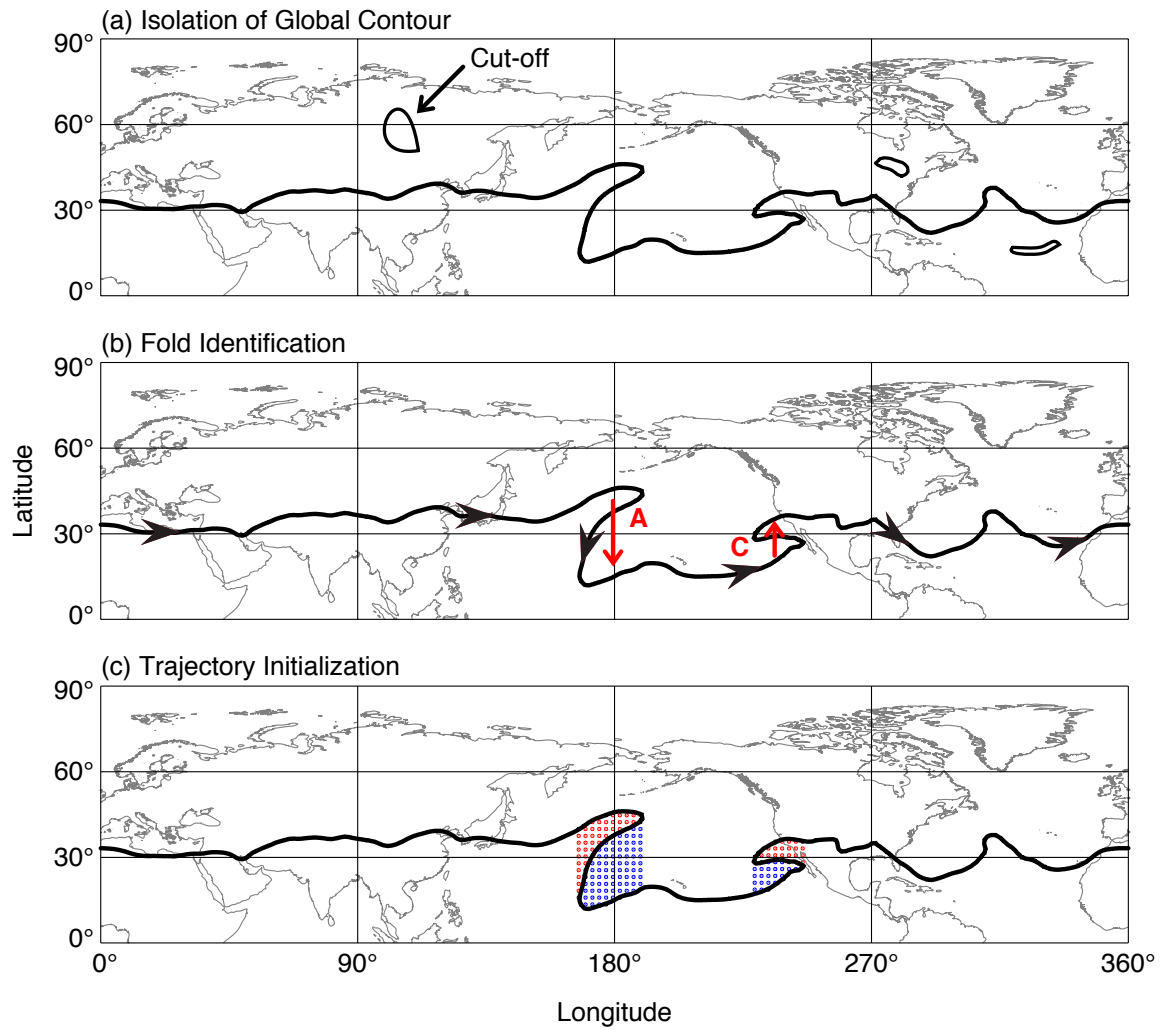
Fig. 6. An illustration of the identification process for wavebreaking events described in Chapter IIIB2.
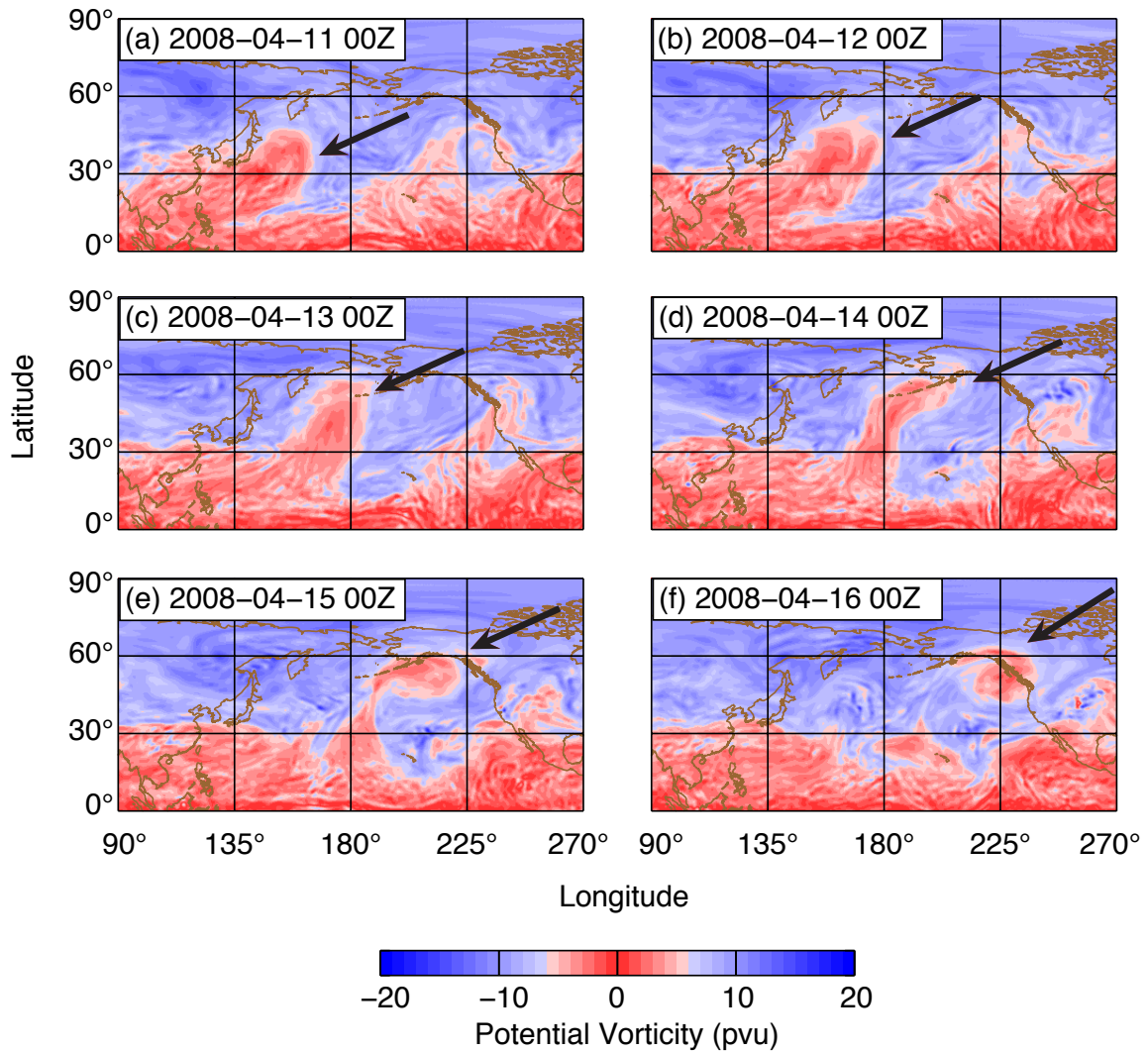
Fig. 7. Evolution of the tropospheric intrusion event sampled during research flight 1 (RF01). The red colors represent |PV| < 6 pvu on the 380 K isentropic surface from high-resolution GFS analyses. Black arrows identify the intruding air mass.
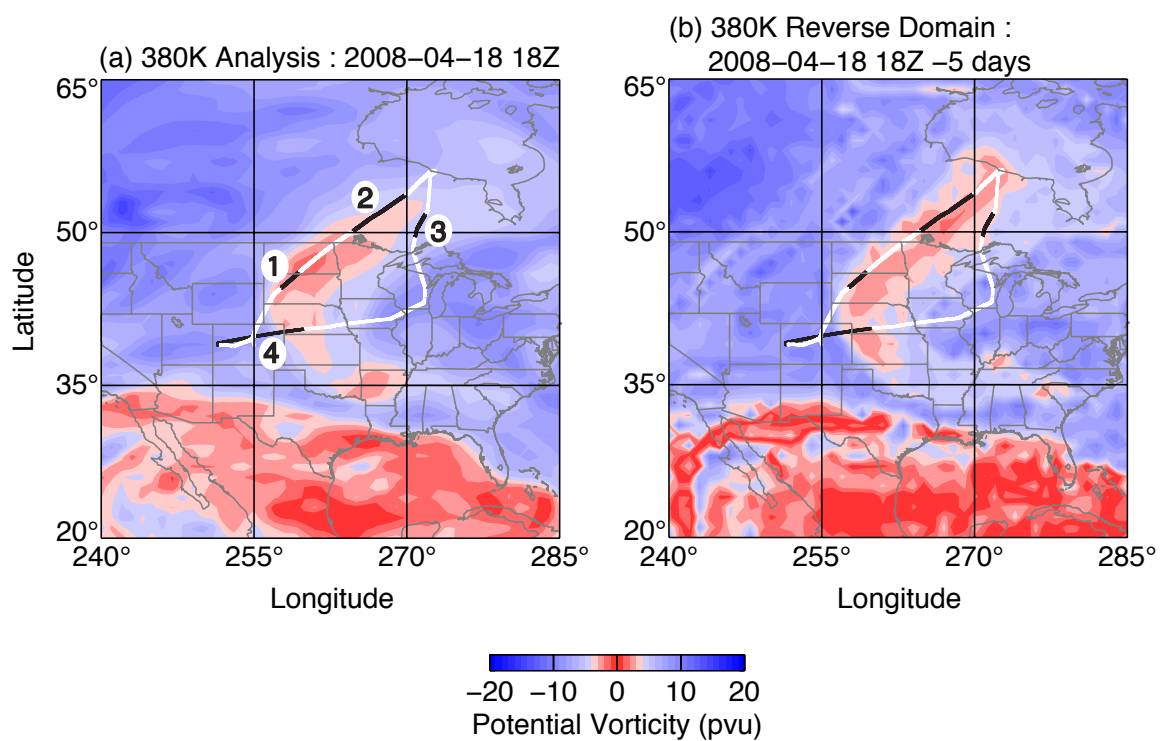
Fig. 8. Maps for the 380 K isentropic surface showing the flight track taken during research flight 1 (RF01) with (a) analysis PV field for 18 April 2008 at 1800 UTC and (b) 5 day reverse domain PV from the analysis time in Figure 8a. The red colors represent $|PV| < 4$ pvu from high-resolution GFS analyses. The black portions of the flight track correspond to the horizontal segments labeled in Figure 9. The flight direction is from Colorado to Hudson Bay to Southeast Wisconsin to Colorado.
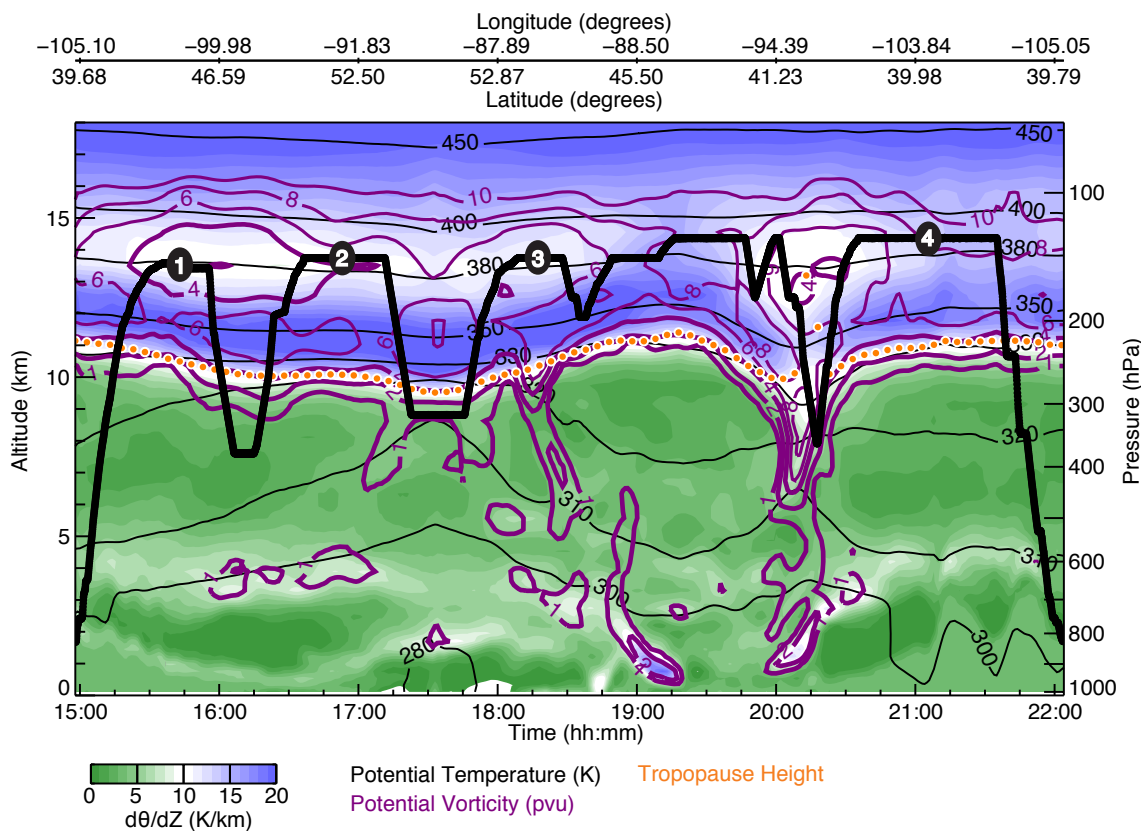
Fig. 9. A vertical cross-section (or curtain) of the atmospheric background for research flight 1 (RF01). All variables are given by high-resolution GFS analyses interpolated to the flight track in space and time. In the curtain, the background is color-filled by the potential temperature lapse rate (or static stability), the orange dots are the NCEP GFS output tropopause height calculated on the model grid, the purple contours are lines of constant potential vorticity, the black contours are potential temperature, and the flight track is the thick black line. Horizontal segments of the flight used for chemical analysis are numbered in white.
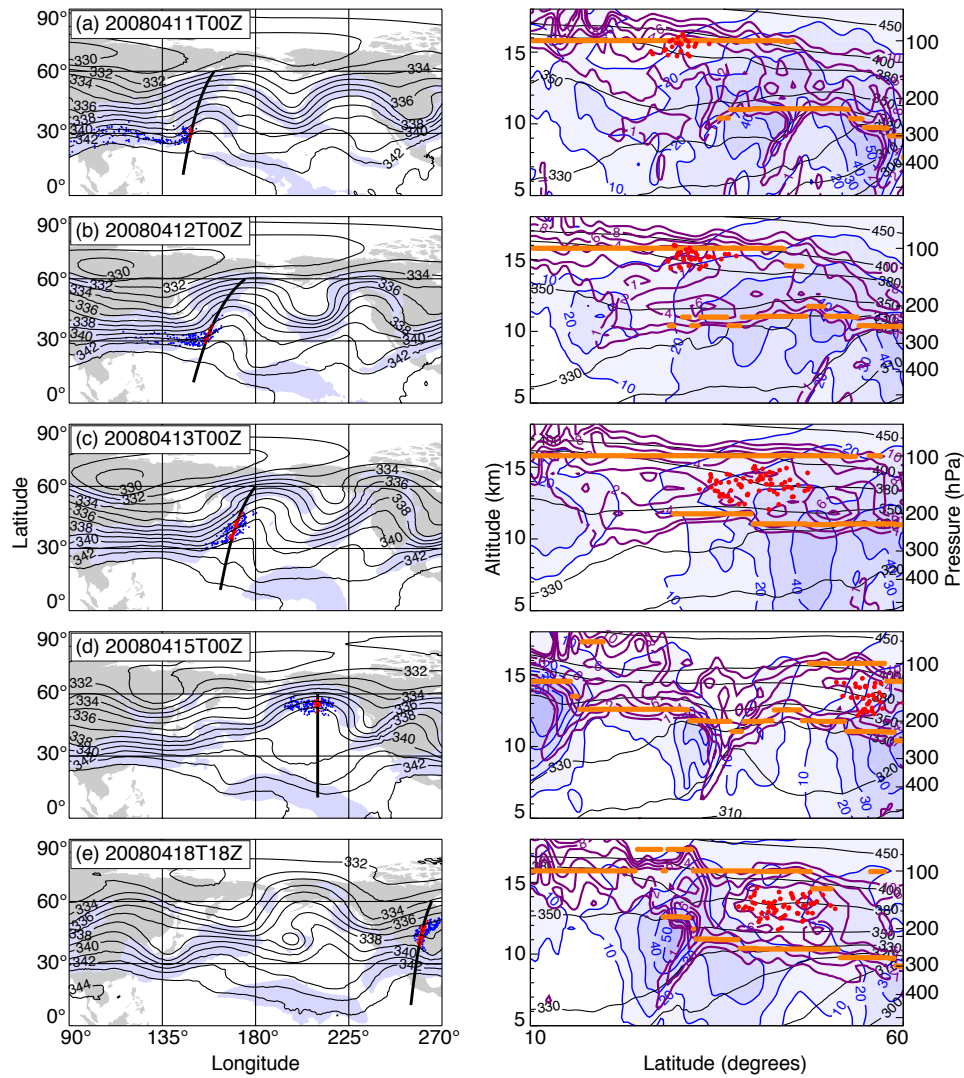
Fig. 10. (left) Maps showing positions of parcels in the intrusion observed on 18 April. On the maps, wind speeds (> 30 m s^{-1}) at 350 K are shown in light blue, contours of Montgomery stream function (units of 10^3 m^2 s^{-2}) are shown in black, trajectory locations are shown as blue and red dots, and the locations of the corresponding vertical section are shown by the thick black lines (great circle arcs). Parcels shown in red on the map correspond to the parcels plotted in red on the vertical section (all parcels within $1°$ of section). (right) Vertical sections from the GFS analysis of wind speed in m s^{-1} (blue colors and contours), potential vorticity in pvu (purple), and potential temperature in K (black). The orange lines are tropopause locations calculated using the WMO algorithm.
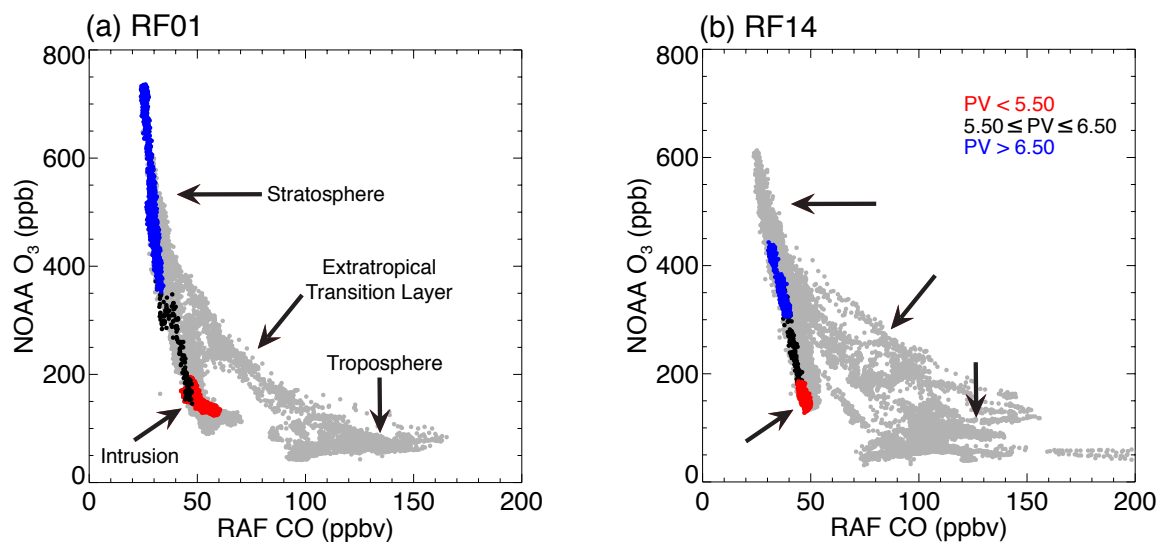
Fig. 11. Scatterplot of NOAA ozone (O_3) and RAF carbon monoxide (CO) for samples taken during (a) RF01 and (b) RF14. All observations are shown in gray. Observations from select horizontal segments (shown for RF01 in Figure 9) are colored by potential vorticity (PV) to illustrate their relationship to the dynamics of the tropospheric intrusion.
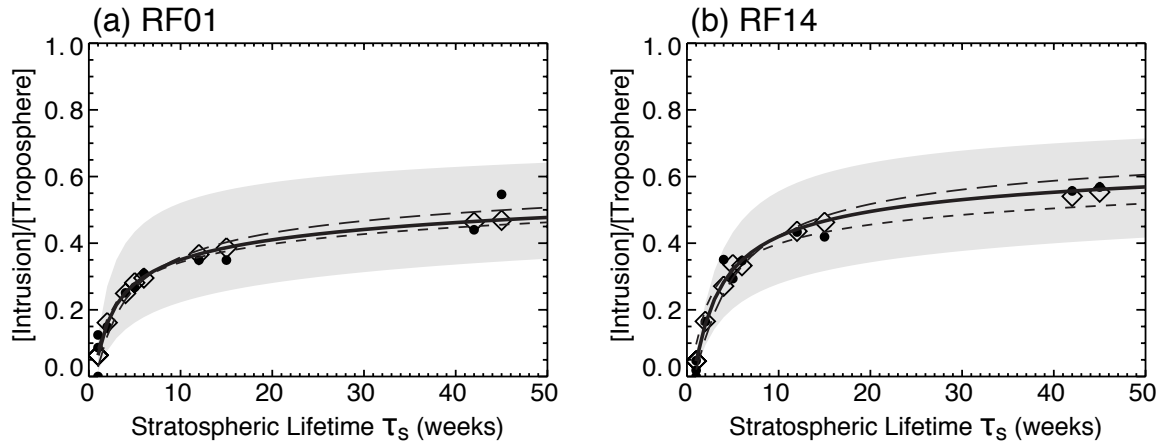
Fig. 12. The ratio of the mean mixing ratio of trace constituents within the observed intrusion to the mean mixing ratio in the troposphere for (a) RF01 and (b) RF14. The black circles are the aircraft data and the black diamonds are values given using parameters from the fit of the model given in Eq. 3.4. The mixing time (τ_m) and tropospheric transit time (t_t) of the fit are given in Table II. The model fit using the lifetime relationship given by the Arrhenius equation is shown in black (solid line). Fits for $t_\mathrm{t} \pm 1$ week are also shown with +1 week long-dashed and -1 week short-dashed. The envelope given by using t_t from the fit and varying τ_m from $\frac{1}{2}\tau_\mathrm{m}$ to $2\tau_\mathrm{m}$ is shown in light gray.
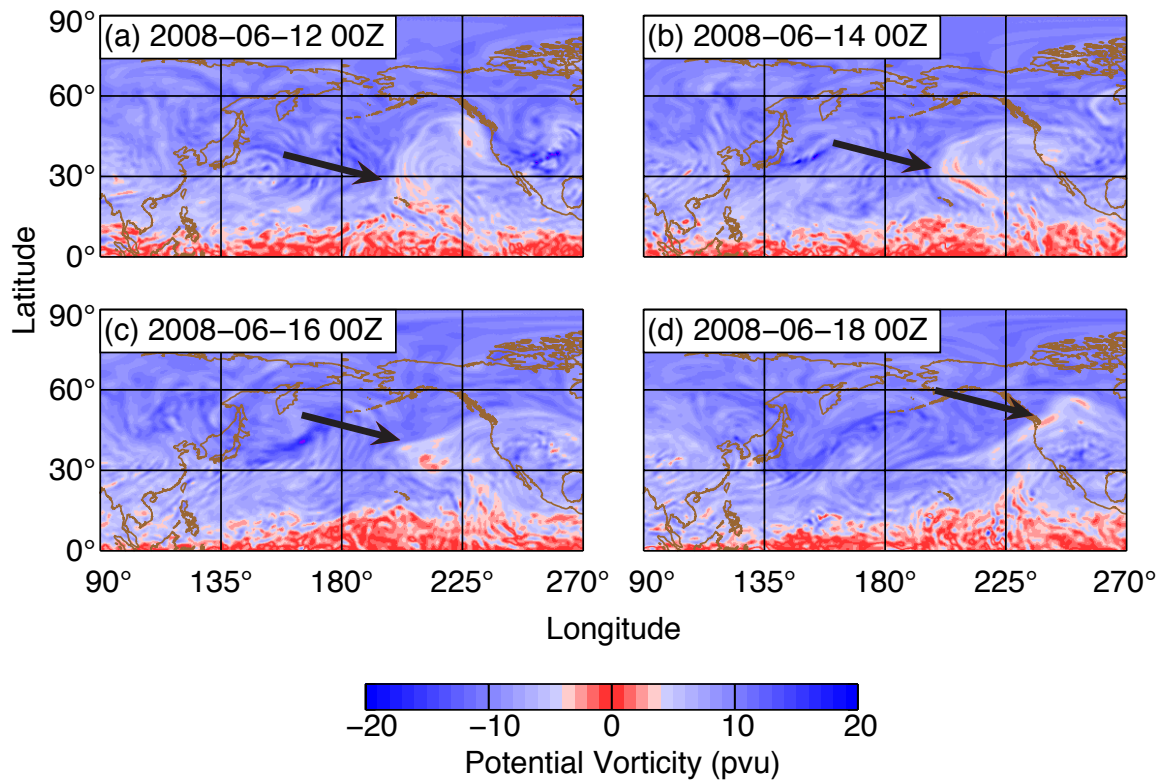
Fig. 13. Evolution of the tropospheric intrusion event sampled during research flight 14 (RF14). The red colors represent |PV| < 4 pvu on the 390K isentropic surface from high-resolution GFS analyses. Black arrows identify the intruding air mass.
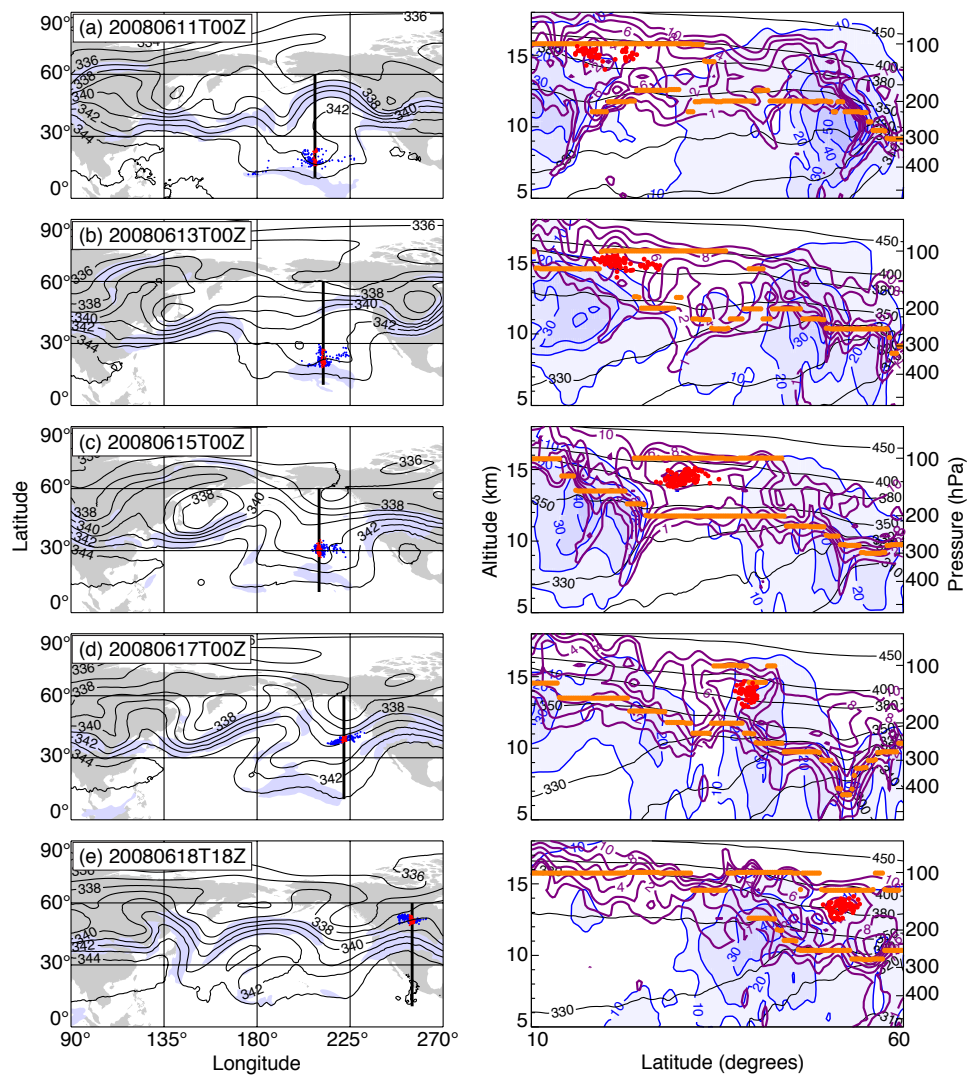
Fig. 14. As in Figure 10, but for RF14.
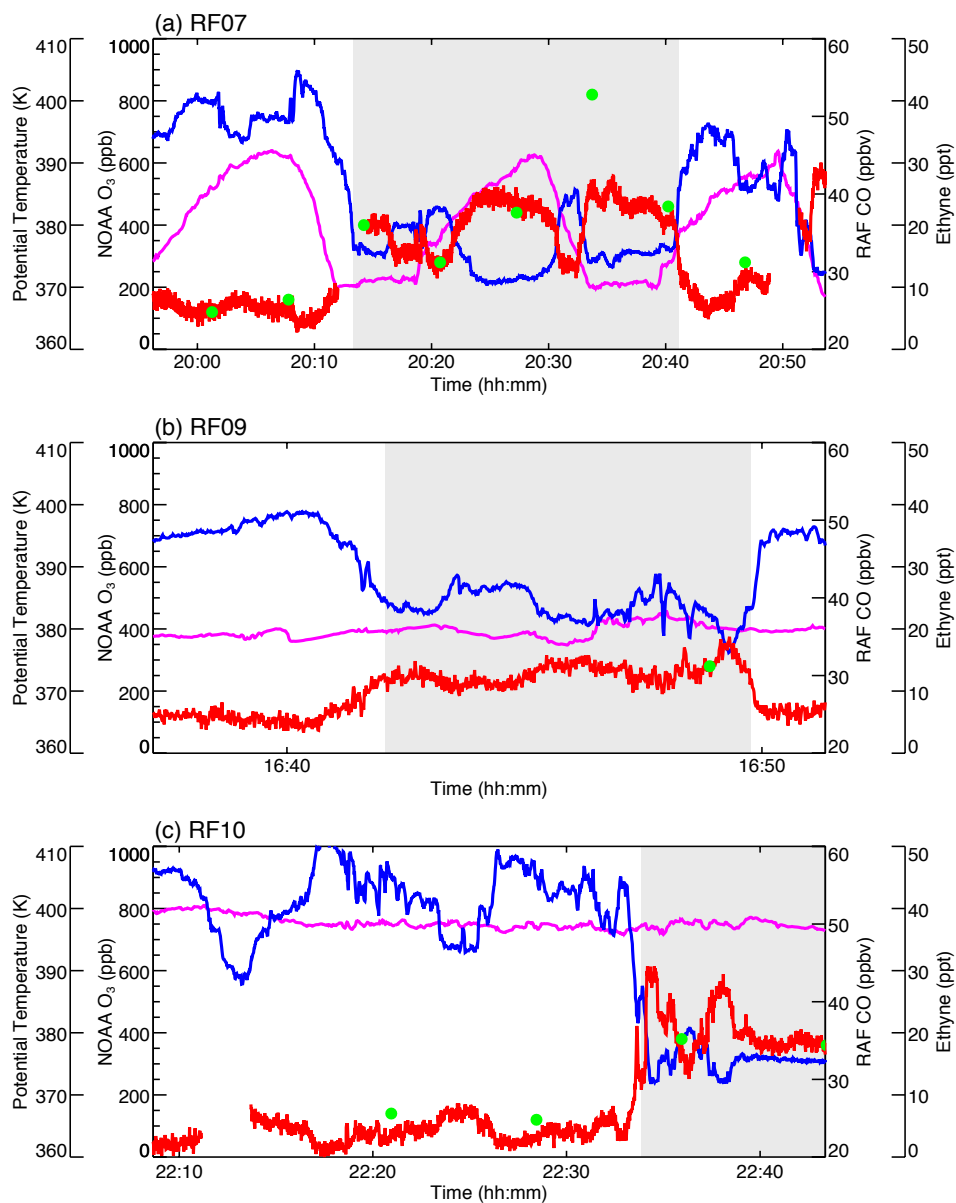
Fig. 15. Timelines for flight segments where small-scale features of air with tropospheric characteristics are observed for flights (a) RF07, (b) RF09 and (c) RF10. In each plot, the magenta line is potential temperature, the blue line is NOAA ozone (O_3), the red line is RAF carbon monoxide (CO), and the green dots are AWAS samples of ethyne (C_2H_2). The periods containing air with tropospheric characteristics are identified by a gray background.
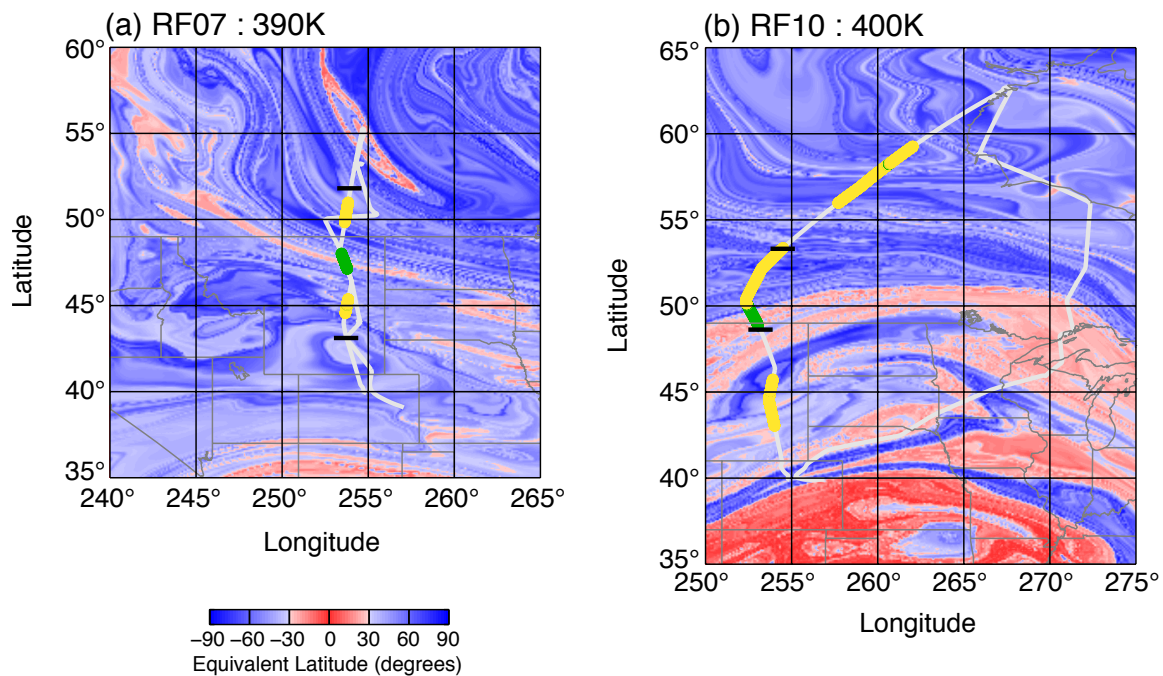
Fig. 16. Maps of 10 day reverse-domain-filled (RDF) equivalent latitude for (a) RF07 on the 390 K isentropic surface and (b) RF10 on the 400 K isentropic surface. The flight track is shown in gray and colored by carbon monoxide (CO) mixing ratio (<30 ppbv, yellow; >30 ppbv, green) where the aircraft potential temperature is within 5 K of the isentropic surface for each map. Black tick marks on the flight track correspond to the timelines shown in Figure 15.
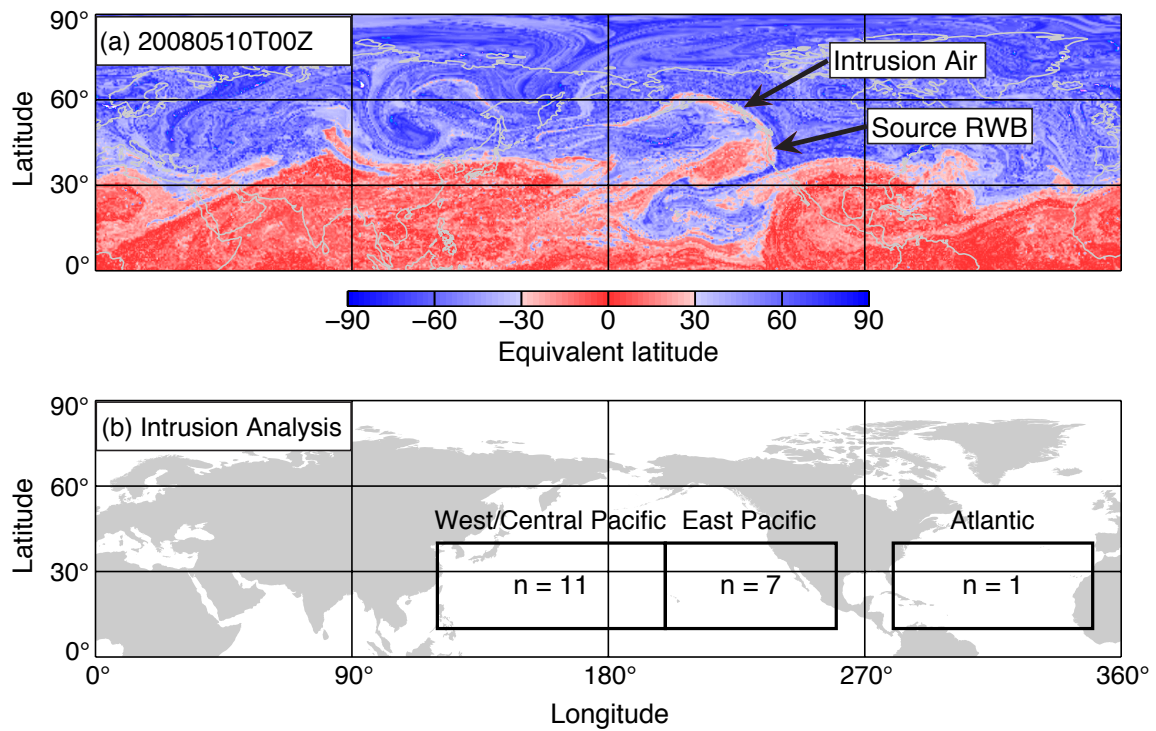
Fig. 17. Maps of (a) an example 10 day reverse-domain-filled (RDF) equivalent lat-itude calculation on the 380 K isentropic surface valid 10 May 2008 at 00 UTC used for the global tropospheric intrusion analysis and (b) number of intrusions observed by region for the global analysis.
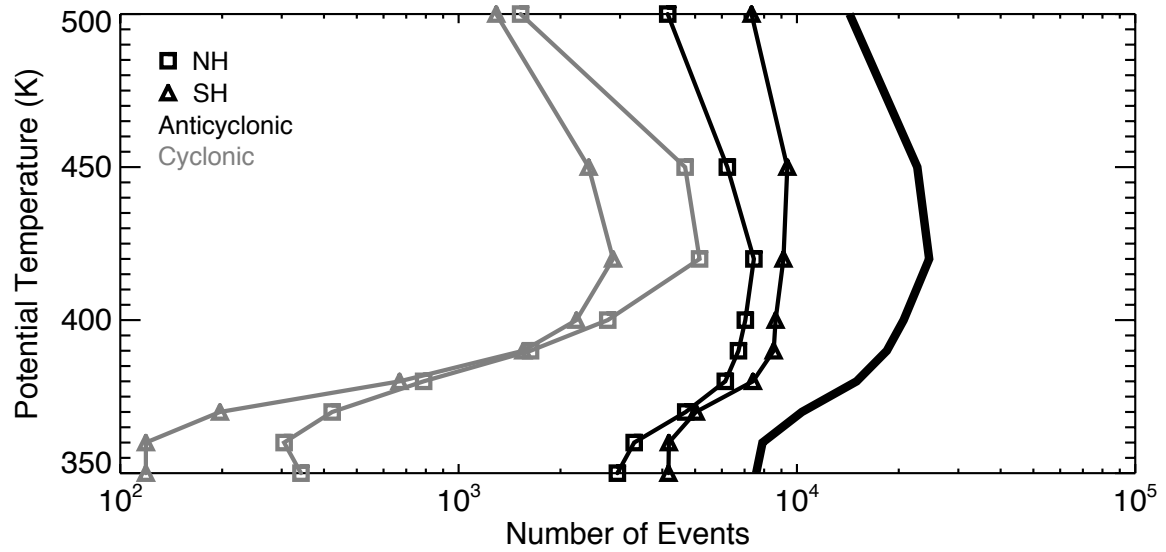
Fig. 18. The number of wavebreaking events identified in the ERA-Interim reanalysis from 1981–2010 as a function of potential temperature. Symbols illustrate the potential temperature surfaces used. The gray symbol-marked lines represent the number of cyclonically sheared events and the black symbol-marked lines, anticyclonic events. Square symbols are northern hemisphere events and triangle symbols are southern hemisphere events. The thick black line is the total of all four profiles.
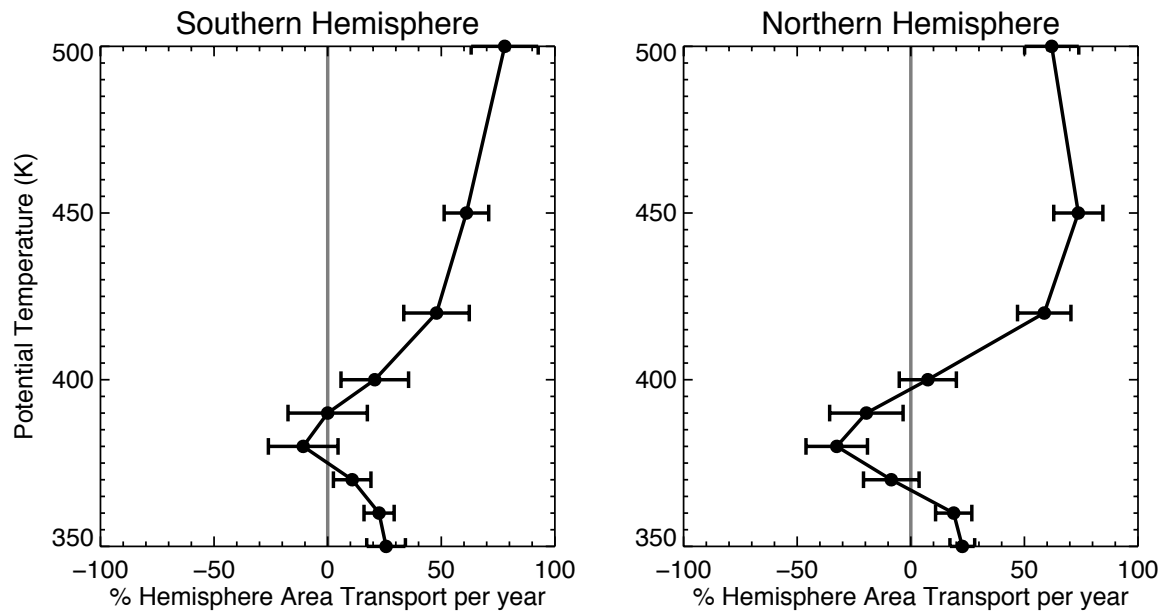
Fig. 19. Net annual Rossby wavebreaking transport as a function of potential temper-ature for the southern hemisphere and the northern hemisphere. In each plot, the black line is the mean and error bars are the standard deviation. Transport magnitudes are shown as the percentage of the area of one hemisphere.
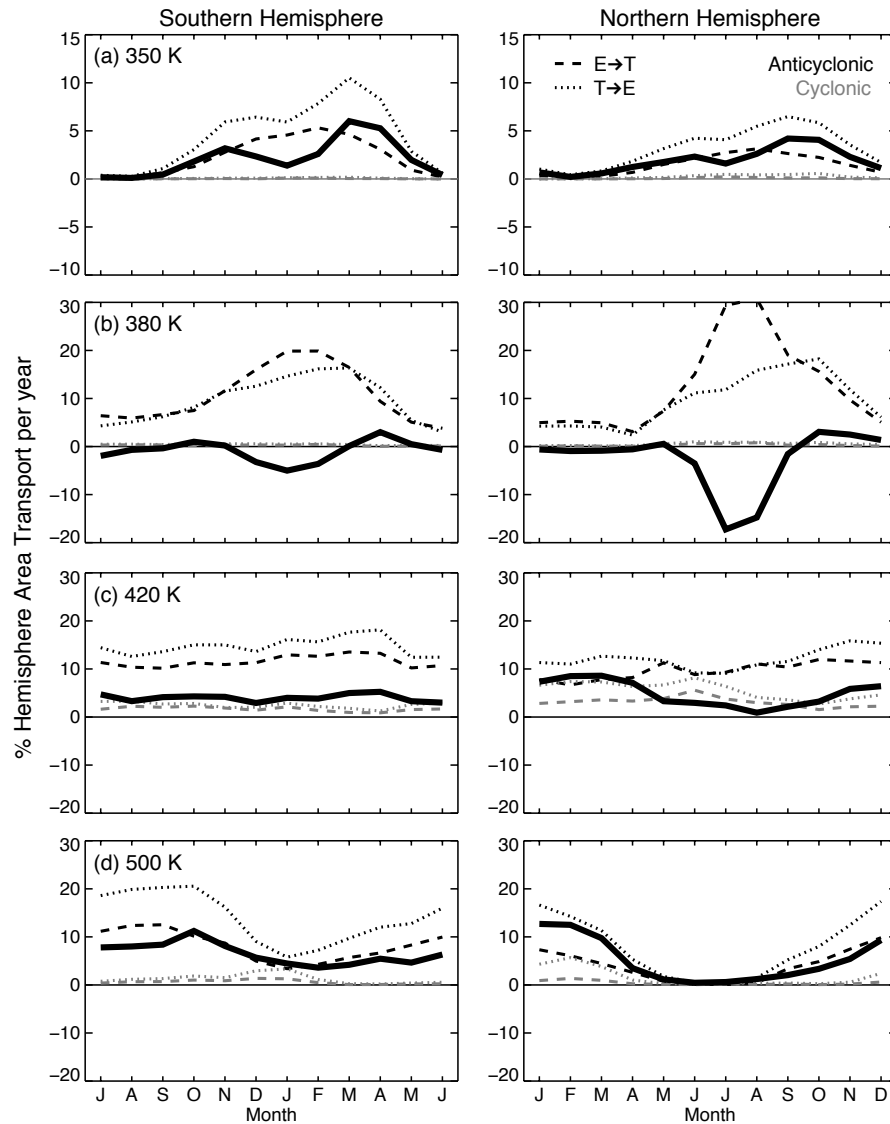
Fig. 20. Annual cycles of Rossby wavebreaking transport at (a) 350 K, (b) 380 K, (c) 420 K, and (d) 500 K. Anticyclonically sheared events are shown in black and cyclonically sheared events, in gray. Dashed lines represent transport from the extratropics into the tropics (equatorward) and dotted lines, tropics into the extratropics (poleward). The thick black line is the net transport, with negative values representing equatorward transport (stratosphere-to-troposphere at lower levels). Note that the abscissa is shifted 6 months between the two hemispheres and that the ordinate is doubly exaggerated for the panels at 350 K. Transport magnitudes are shown as the percentage of the area of one hemisphere.
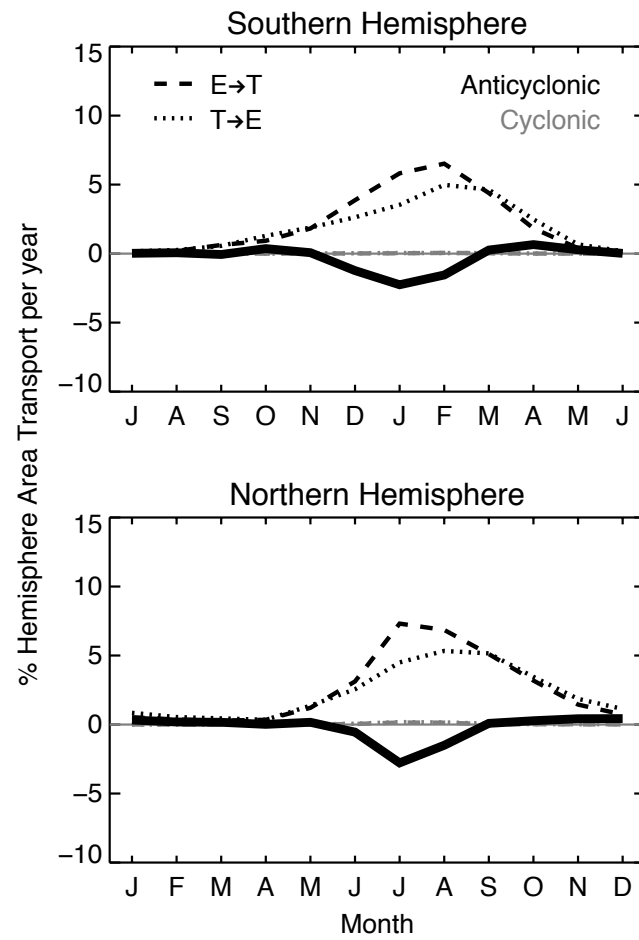
Fig. 21. As in Figure 20a, but relative to the ±2 pvu contour of potential vorticity (PV) at 350 K.
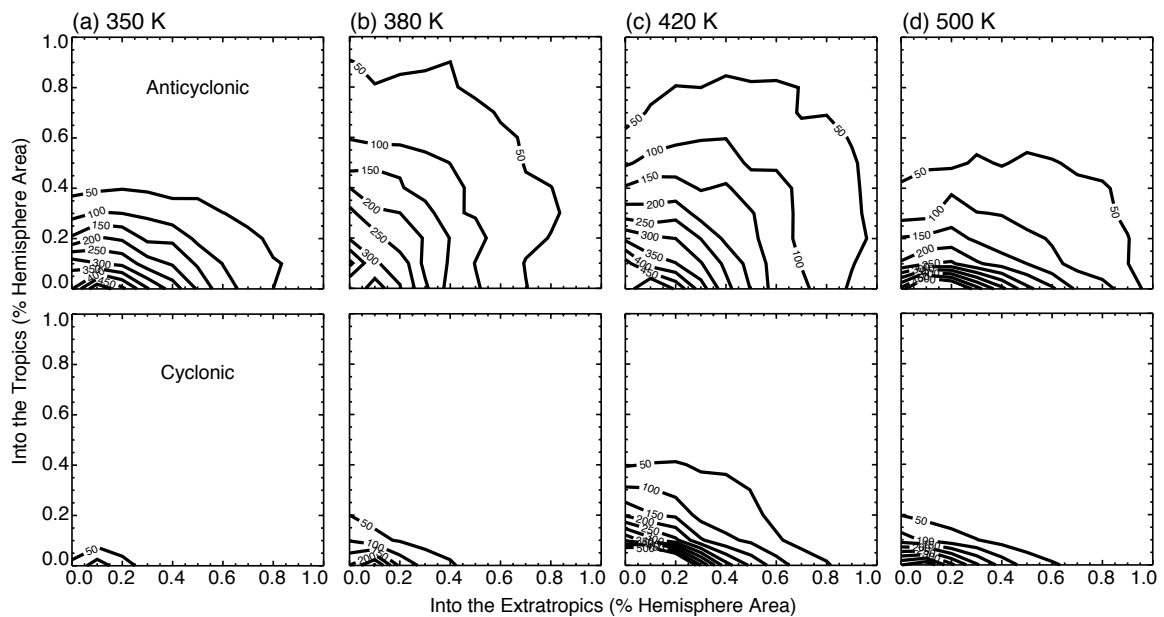
Fig. 22. Density plots of the number of Rossby wavebreaking events as a function of extratropical and tropical air mass transport at (a) 350 K, (b) 380 K, (c) 420 K, and (d) 500 K for top: anticyclonically sheared events and bottom: cyclonically sheared events. Transport magnitudes are shown as the percentage of the area of one hemisphere. These distributions were calculated using a bin resolution of 0.1 x 0.1 %.
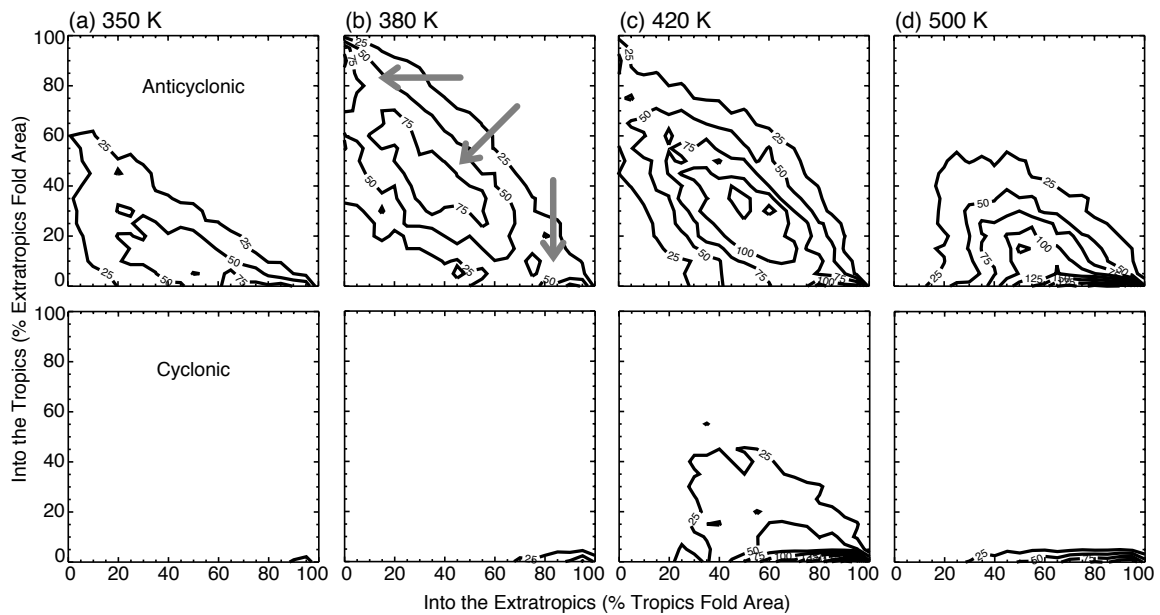
Fig. 23. Density plots of the number of Rossby wavebreaking events as a function of fractional extratropical and tropical air mass transport at (a) 350 K, (b) 380 K, (c) 420 K, and (d) 500 K for top: anticyclonically sheared events and bottom: cyclonically sheared events. Transport magnitudes are shown as the percentage of the analyzed area of each wavebreaking air mass. These distributions were calculated using a bin resolution of 5 x 5 %.
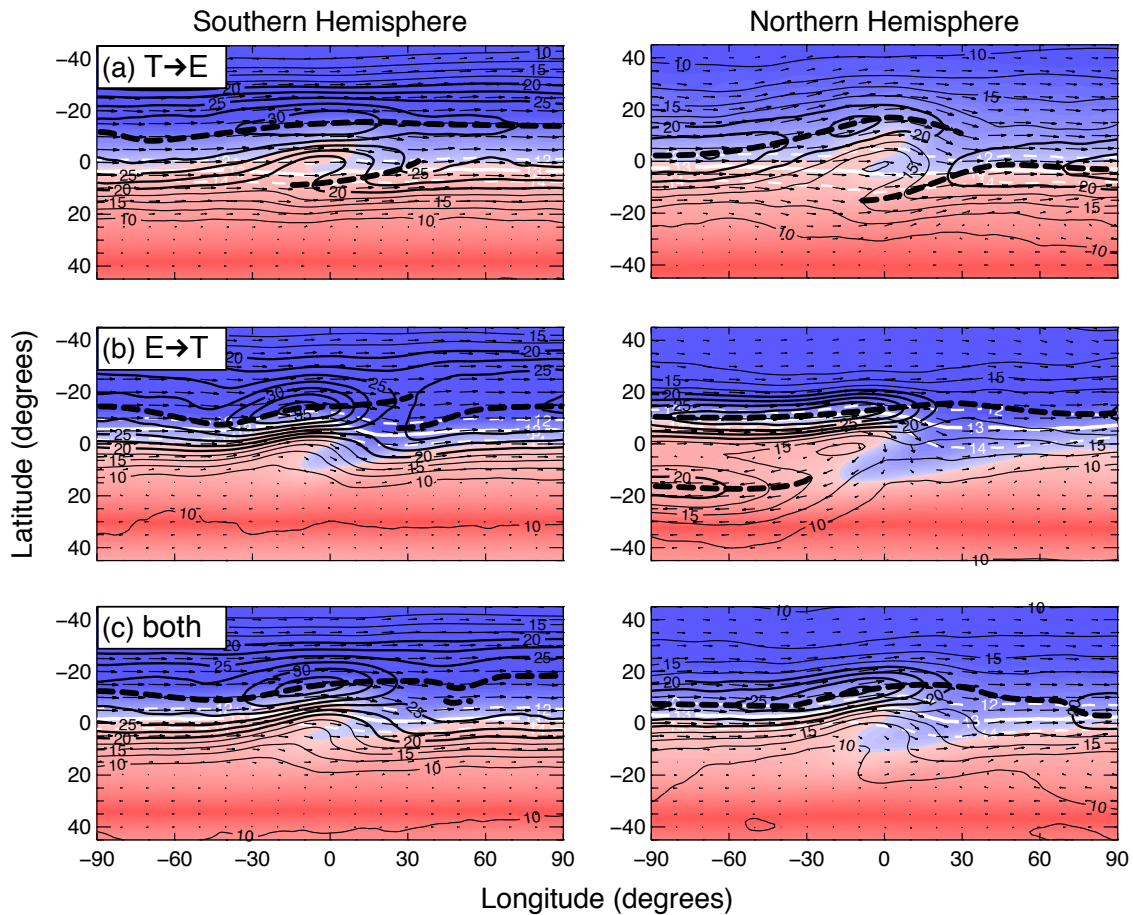
Fig. 24. Composite mean equivalent latitude (color-fill), wind speed (m/s, solid black lines), wind direction (vectors), jet axes (dashed black lines)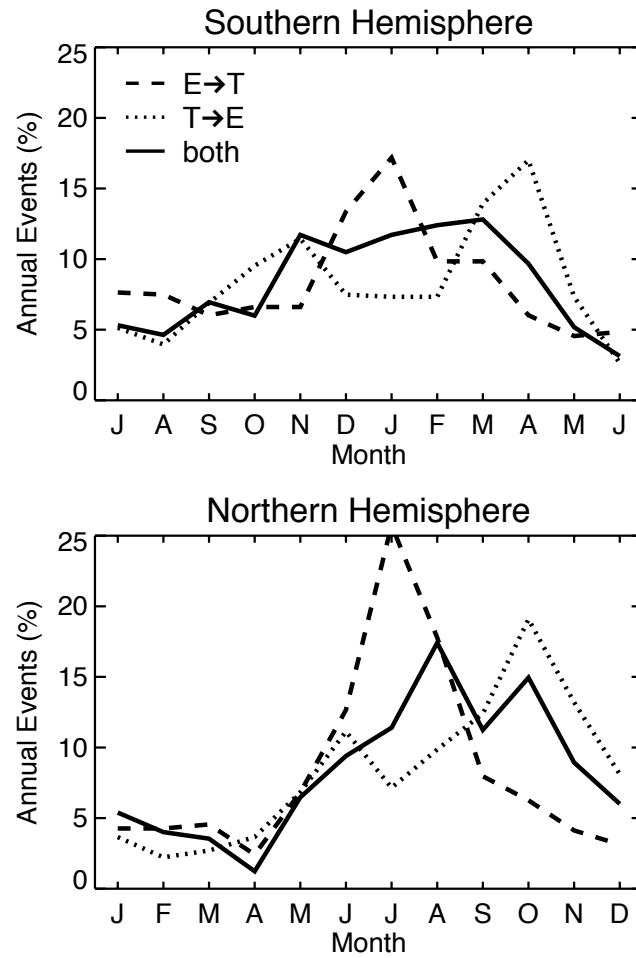, and tropopause pressure altitudes of 12, 13 (solid), and 14 km (white lines) of anticyclonically sheared wavebreaking events on the 380 K potential temperature surface for (a) predominately tropics-to-extratropics transport, (b) predominately extra-tropics-to-tropics transport, and (c) bidirectional transport. The transport designations correspond to the three frequency maxima identified in Figure 23b. Red colors of equivalent latitude represent air equatorward of the mean analyzed wavebreaking contour, while blue colors represent air poleward. Jet axes are shown as meridional maxima in wind speed for wind speeds exceeding 15 m/s. Note that the relative latitude axes for both hemispheres are oriented equator-to-pole. The number of events and their mean latitudes contributing to these composites are given in Table III.

Fig. 25. Annual cycles of anticyclonically sheared wavebreaking events on the 380 K potential temperature surface for predominately tropics-to-extratropics transport (dotted lines), extratropics-to-tropics transport (dashed lines), and bidirectional transport (solid lines). The transport designations correspond to the three frequency maxima identified in Figure 23b. Note that the abscissa is shifted 6 months between the two hemispheres.
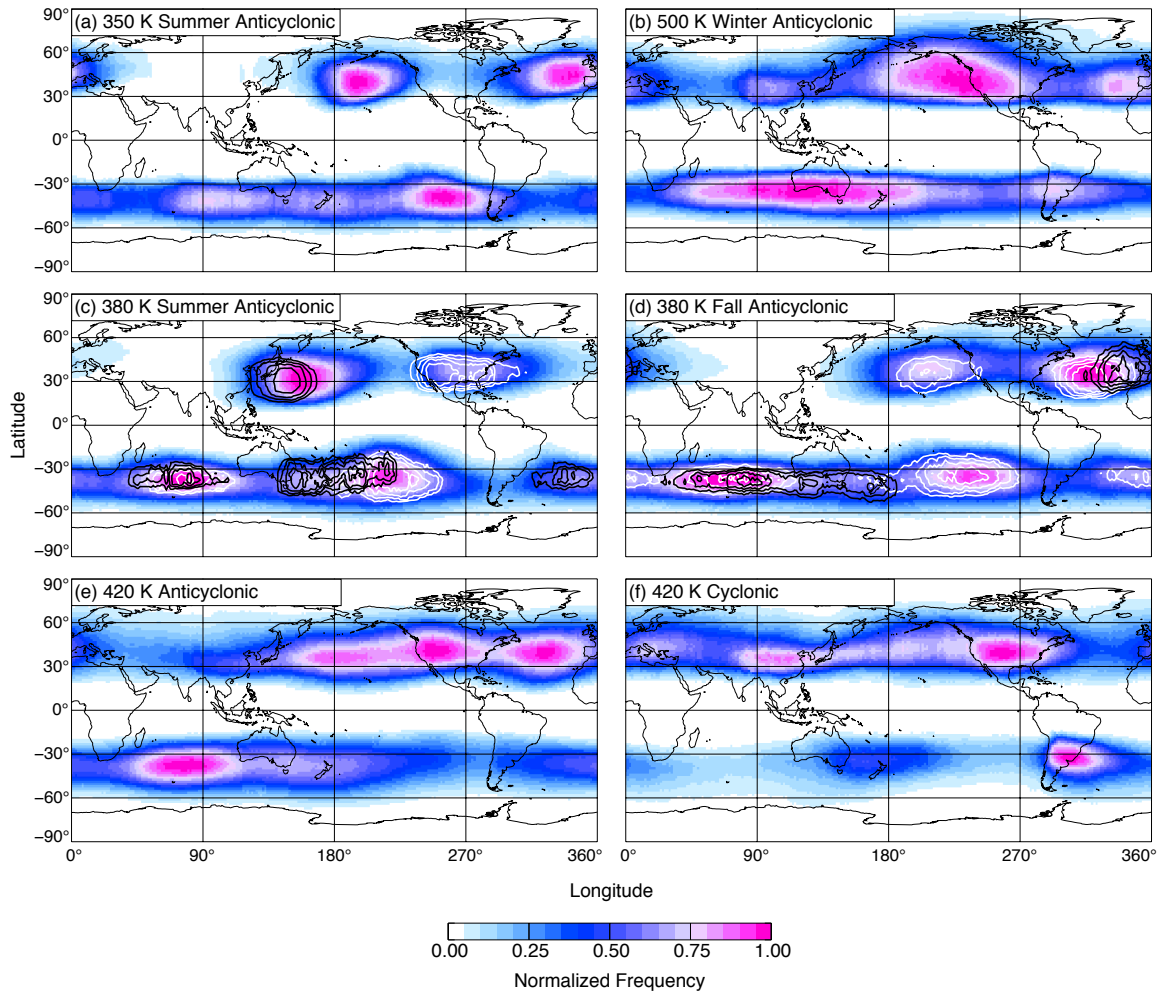
Fig. 26. Hemispherically normalized distributions of anticyclonically sheared wave-breaking events at (a) 350 K during summer, (b) 500 K during winter, (c) 380 K during summer, (d) 380 K during fall, (e) 420 K during all seasons, and of (f) cyclonically sheared wavebreaking events at 420 K during all seasons. The white contours in (c) and (d) represent normalized maxima of bidirectional transport events and are contoured from 0.6 to 1.0 by 0.1. Similarly, the black contours in (c) represent predominately extratropics-to-tropics transport events, and in (d) predominately tropics-to-extratropics transport events. The transport designations correspond to the three frequency maxima identified in Figure 23b.
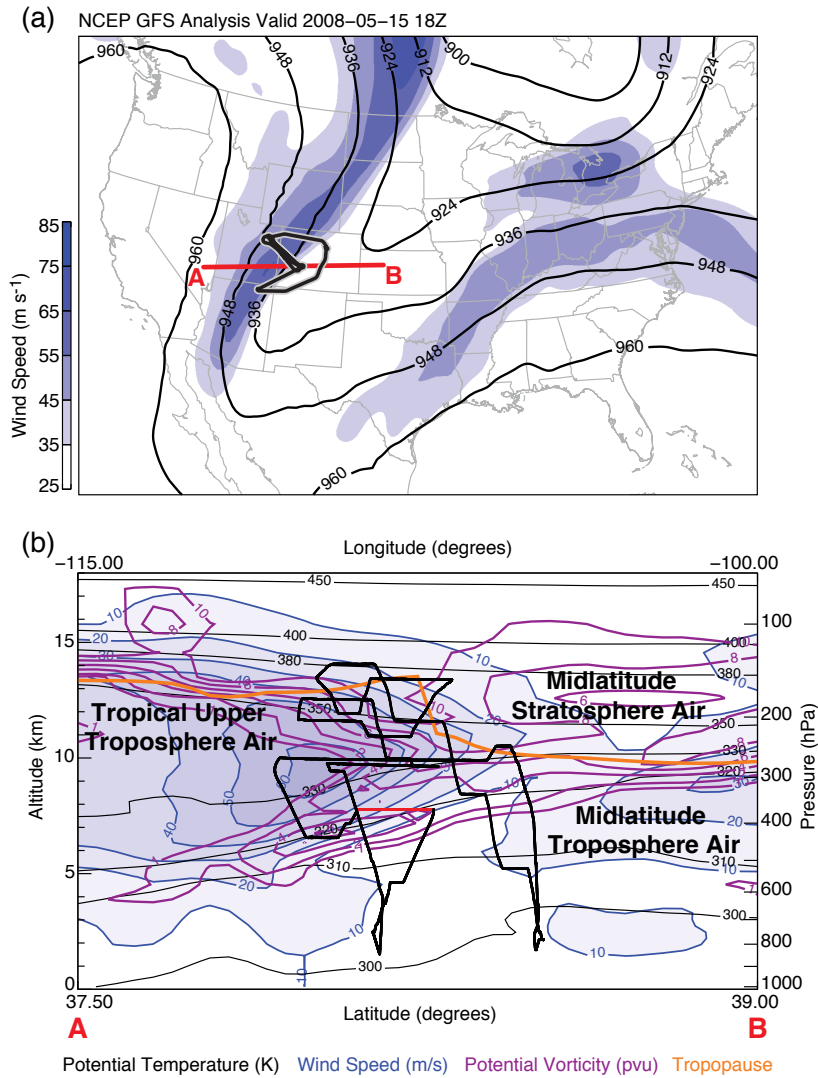
Fig. 27. For research flight 12 (RF12): (a) map of GFS analysis 300 hPa wind speed (color-fill) and geopotential height in dm (black lines) valid 15 May 2008 at 18 UTC and (b) vertical cross-section through the observed stratospheric intrusion with potential temperature (black lines), wind speed (color-fill, blue lines), potential vorticity (purple lines), model output lapse-rate tropopause (orange line), and air masses corresponding to the ozone - carbon monoxide scatterplot given in Figure 31a are labeled in black. The vertical section is taken along the red line A–B in the map. The flight track is the black line outlined in gray on the map and the black and red line projected onto the vertical section. Convective injection into the stratospheric intrusion was observed along the red segment of the flight.
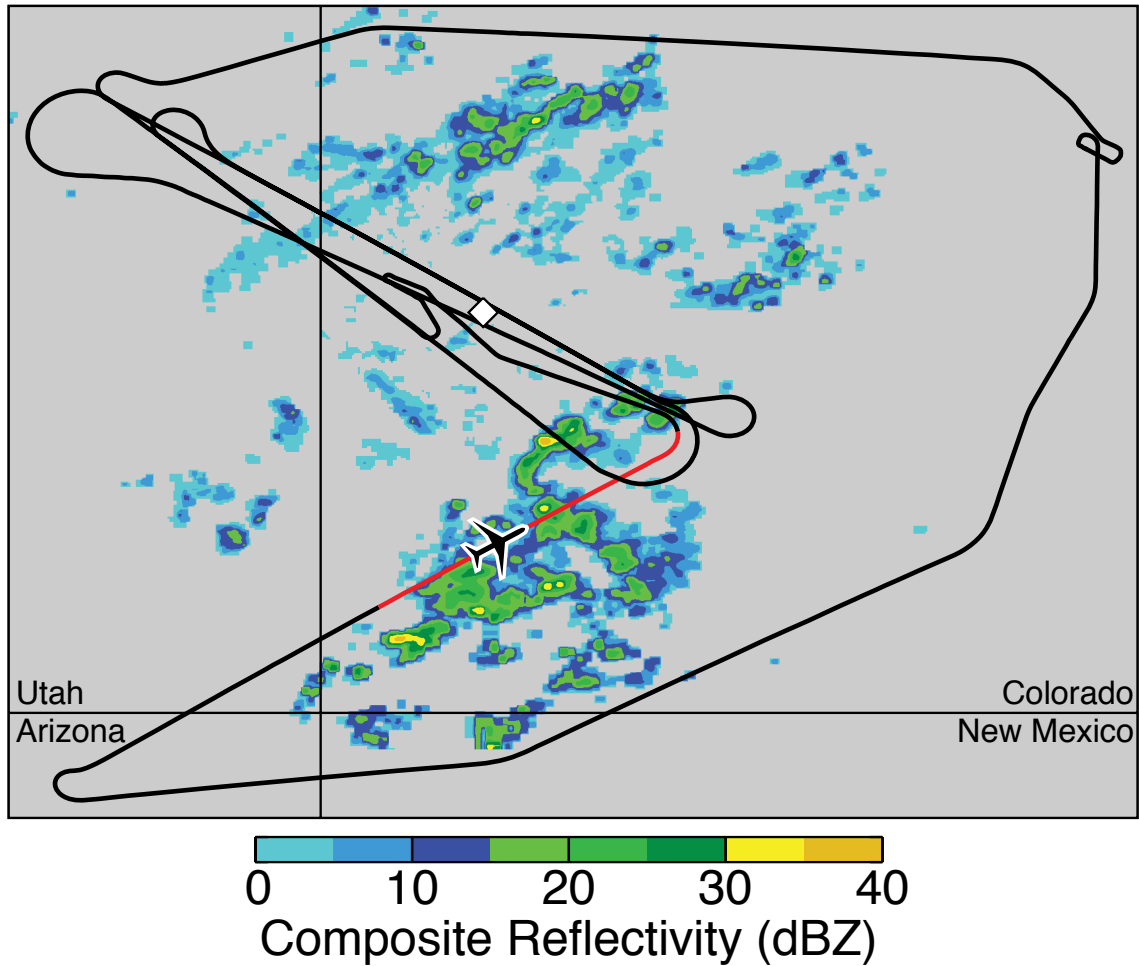
Fig. 28. Composite radar reflectivity from the Grand Junction, Colorado (ICAO code KGJX) NEXRAD station on 15 May 2008 at 17:12 UTC. The black and red line is the flight track from research flight 12 (RF12) with red colors denoting the flight segment of convective injection into the observed stratospheric intrusion (as in Fig. 27b). The airplane symbol is the aircraft location at the radar analysis time with the nose pointing in the flight direction. The white diamond shows the location of the radar.

Fig. 29. Snapshots from the GV aircraft wing-mounted video camera during convective plumes (a) CP1 and (b) CP2 labeled in Figure 30.
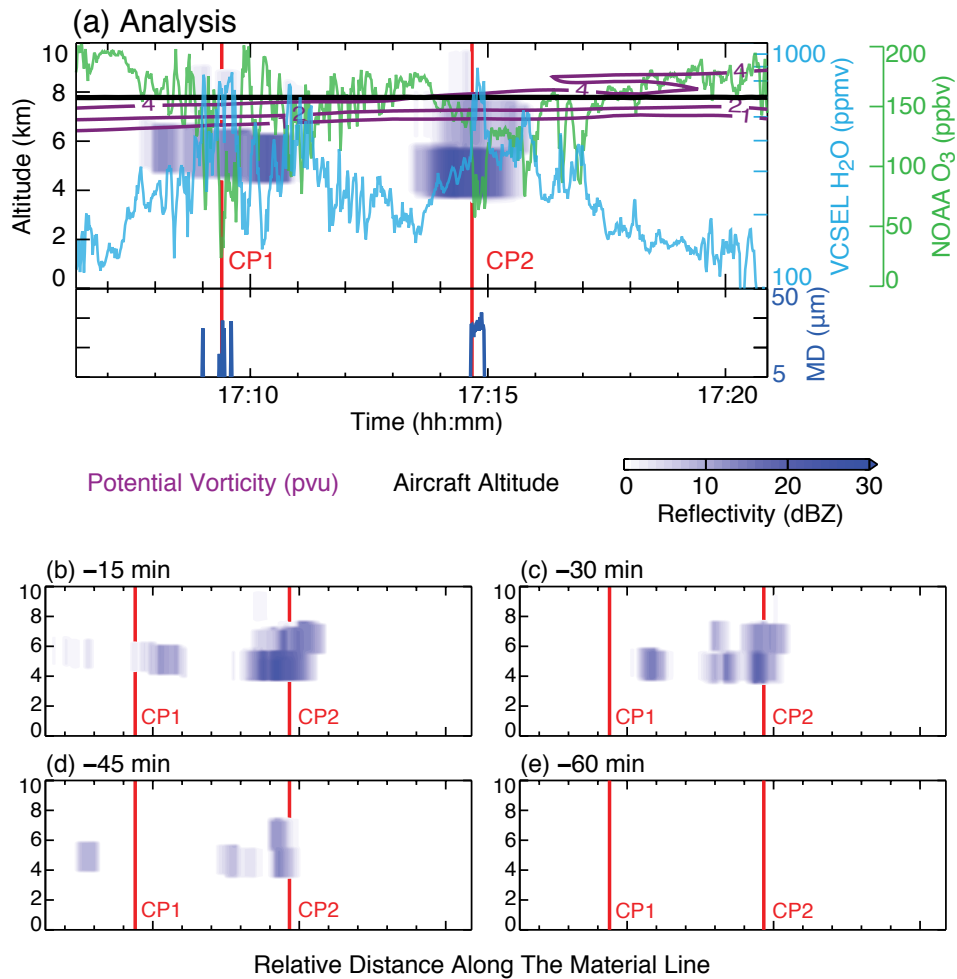
Fig. 30. (a) (top) Vertical section of NEXRAD radar reflectivity (blue color-fill) and GFS analysis potential vorticity (purple lines) and in situ measurements of ozone (O_3, green) and water vapor (H_2O, blue) and (bottom) SID-2H mean ice particle diameter (MD, dark blue) along the flight segment of convective injection into the observed stratospheric intrusion from research flight 12 (red portions of the flight track in Figs. 27b & 28). The aircraft altitude, which is nearly constant along this flight segment, is the thick black line in the vertical section. (b)-(e) Column radar reflectivity along back trajectories from the aircraft analysis times for (b) 15 minutes, (c) 30 minutes, (d) 45 minutes, and (e) 60 minutes prior. The two convective plumes sampled during RF12 are illustrated by the vertical red lines labeled CP1 and CP2 in each section.
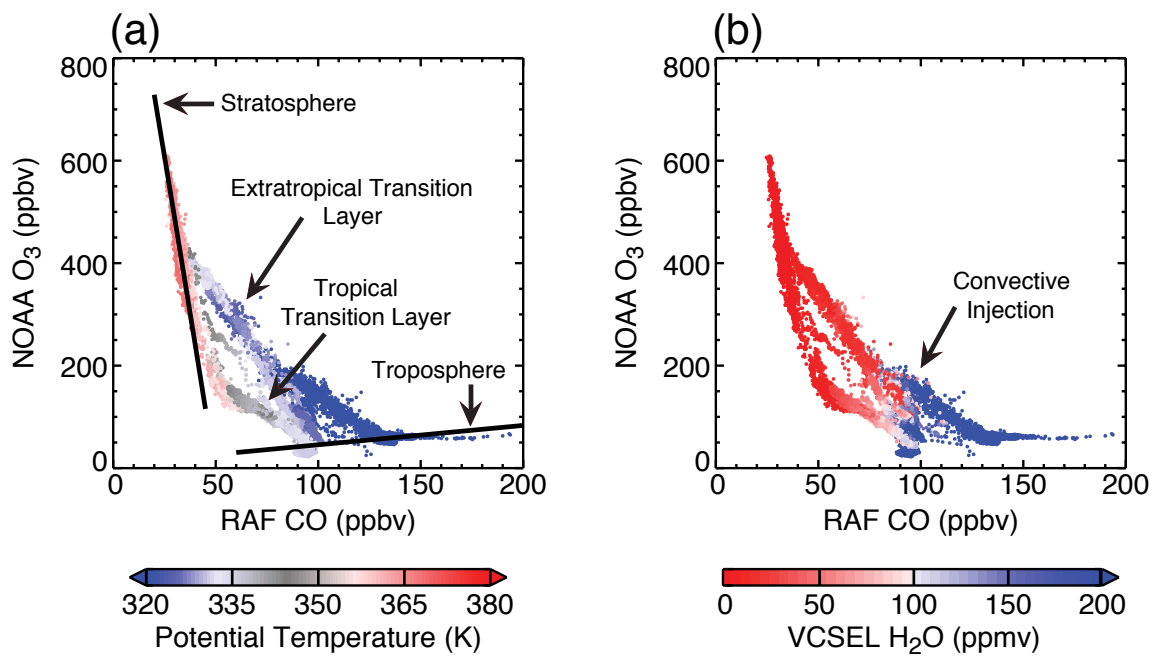
Fig. 31. Scatterplot of ozone (O$_3$) and carbon monoxide (CO) colored by (a) potential temperature and (b) water vapor (H$_2$O) for research flight 12 (RF12).

(a) NCEP GFS Analysis Valid 2008-05-02 00Z

(b)

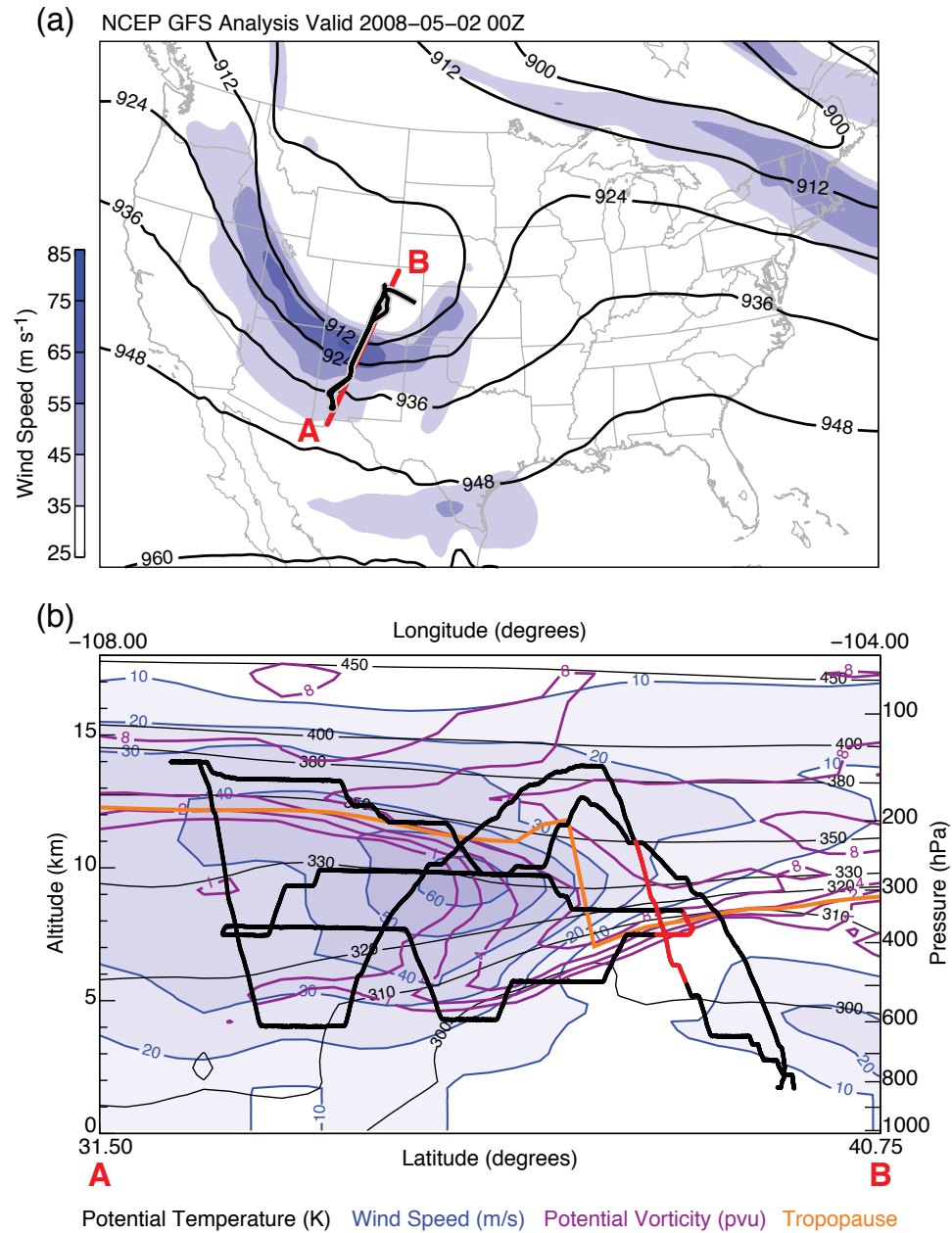Potential Temperature (K)   Wind Speed (m/s)   Potential Vorticity (pvu)   Tropopause

Fig. 32. As in figure 27, but for research flight 6 (RF06) valid 2 May 2008 at 00 UTC.
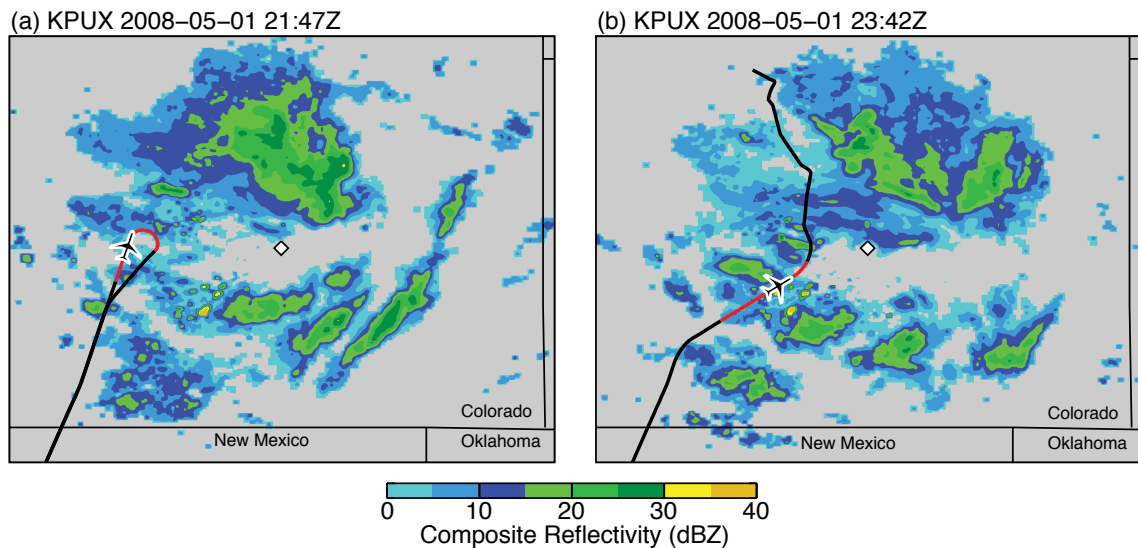
Fig. 33. Composite radar reflectivity from the Pueblo, Colorado (ICAO code KPUX) NEXRAD station on 1 May 2008 at (a) 21:47 UTC and (b) 23:42 UTC. The black and red line on each map is the flight track from research flight 6 (RF06) within 30 minutes of the analysis time. Red colors of each flight track denote flight segments of convective injection into the observed stratospheric intrusion (as in figure 32b). The airplane symbol in each map is the aircraft location at the radar analysis time with the nose pointing in the flight direction. The white diamonds in each map show the location of the radar.
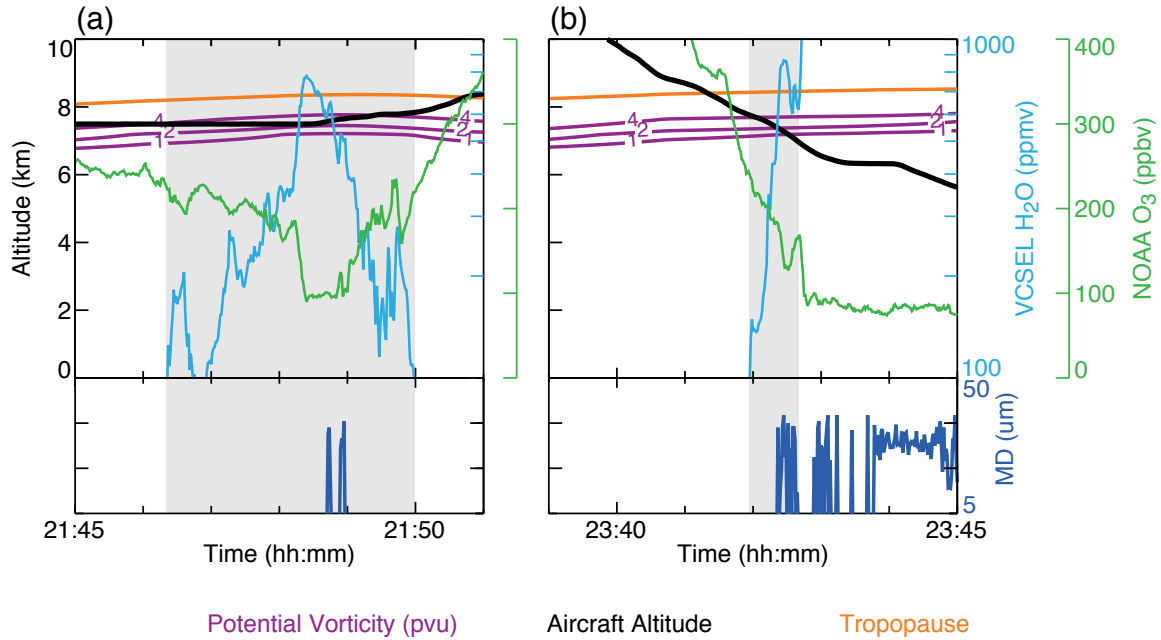
Fig. 34. Vertical section of GFS analysis potential vorticity (purple lines) and model output lapse-rate tropopause (orange lines) and in situ measurements of ozone (O_3, green) and water vapor (H_2O, blue) and (bottom) SID-2H mean ice particle diameter (MD, dark blue) along the flight segments of convective injection into the observed stratospheric intrusion from research flight 06 (red portions of the flight track in Figs. 32b & 33). The aircraft altitude is the thick black line in each vertical section. The periods of measurement with convective injection characteristics are identified by a gray background.
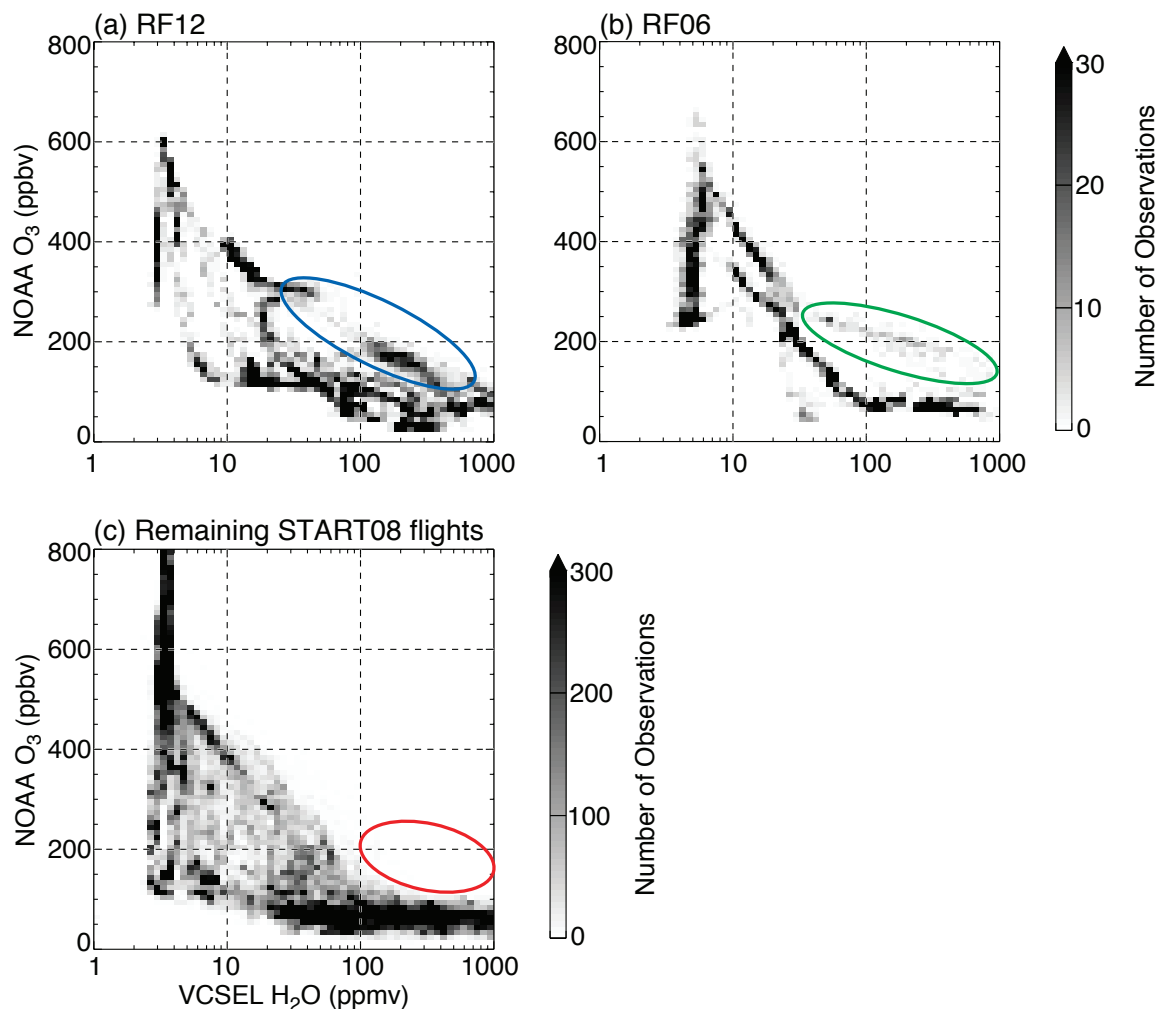
Fig. 35. Density plot of ozone (O$_3$) and water vapor (H$_2$O) for (a) research flight 12 (RF12), (b) research flight 6 (RF06) and (c) remaining START08 flights. The blue and green ellipses in (a) & (b) encapsulate the observations of convective injection during each flight, respectively. The red ellipse in (c) encapsulates the area where convective injection was observed during research flights 12 and 6. No observations were found in this region during the remaining START08 flights.

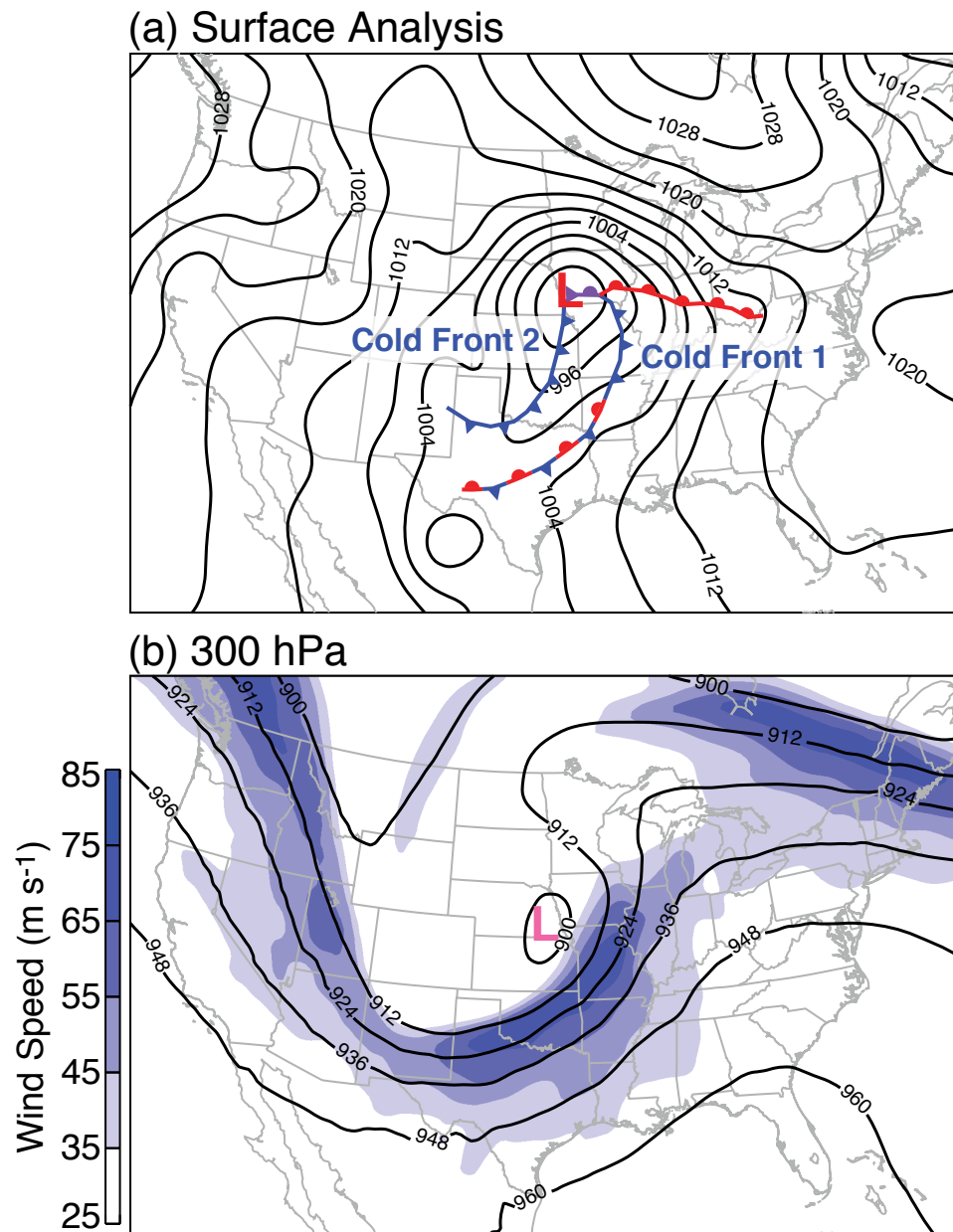## (a) Surface Analysis

(b) 300 hPa

Fig. 36. For 11 April 2008 at 00 UTC, maps of (a) GFS mean sea level pressure in hPa (black lines) and National Weather Service Hydrometeorological Prediction Center frontal analysis and (b) GFS 300 hPa wind speed (color-fill) and geopotential height in dm (black lines). In (a), the location of the surface low (cyclone) is denoted by a large red "L". In (b), the location of the 300 hPa low (cyclone) is denoted by a large magenta "L".
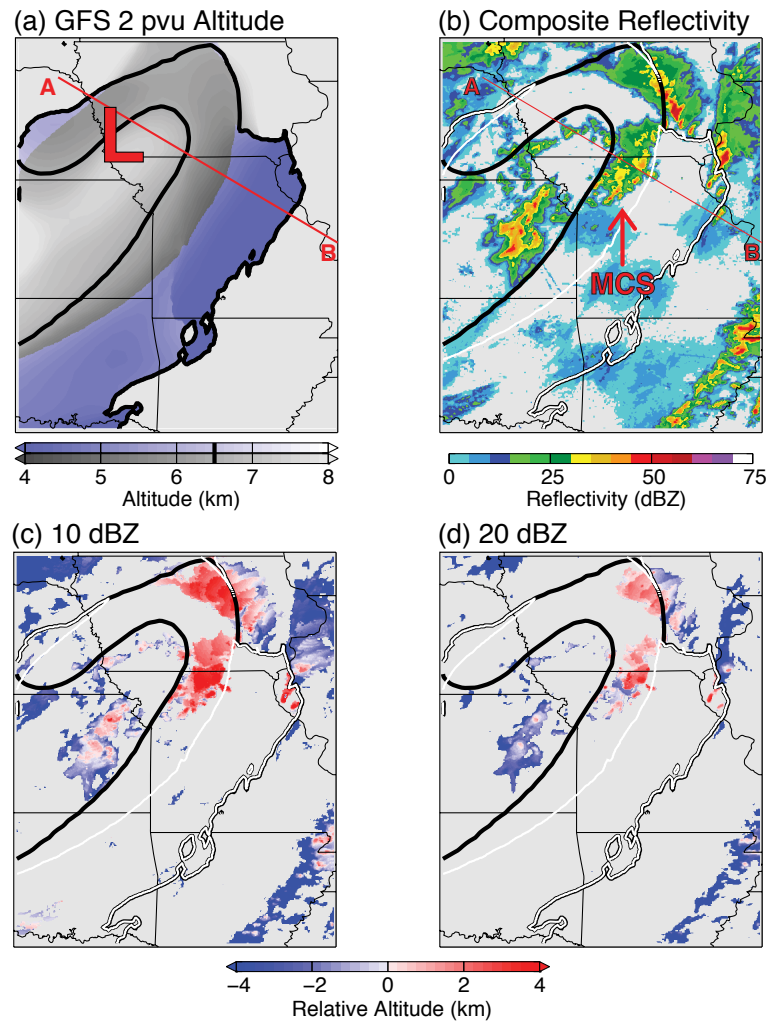
Fig. 37. For 11 April 2008 at 00 UTC, maps of (a) altitude of the 2 pvu surface of GFS analysis potential vorticity, (b) NEXRAD composite radar reflectivity, (c) the maximum altitude of the 10 dBZ reflectivity surface relative to the altitude of the 2 pvu surface and (d) as in (c), but for 20 dBZ. In each map, the 6.5 km altitude contour of the 2 pvu surface is shown by the thick black line. In (a), the location of the surface low (cyclone) is denoted by a large red "L" and areas where the 2 pvu surface is multi-valued (i.e., folded) are colored in blue. In (b)-(d), areas where the 2 pvu surface is multi-valued are shown by the thick white lines. In (a) & (b), the location of the vertical section in figure 38 is given by the thick red line.
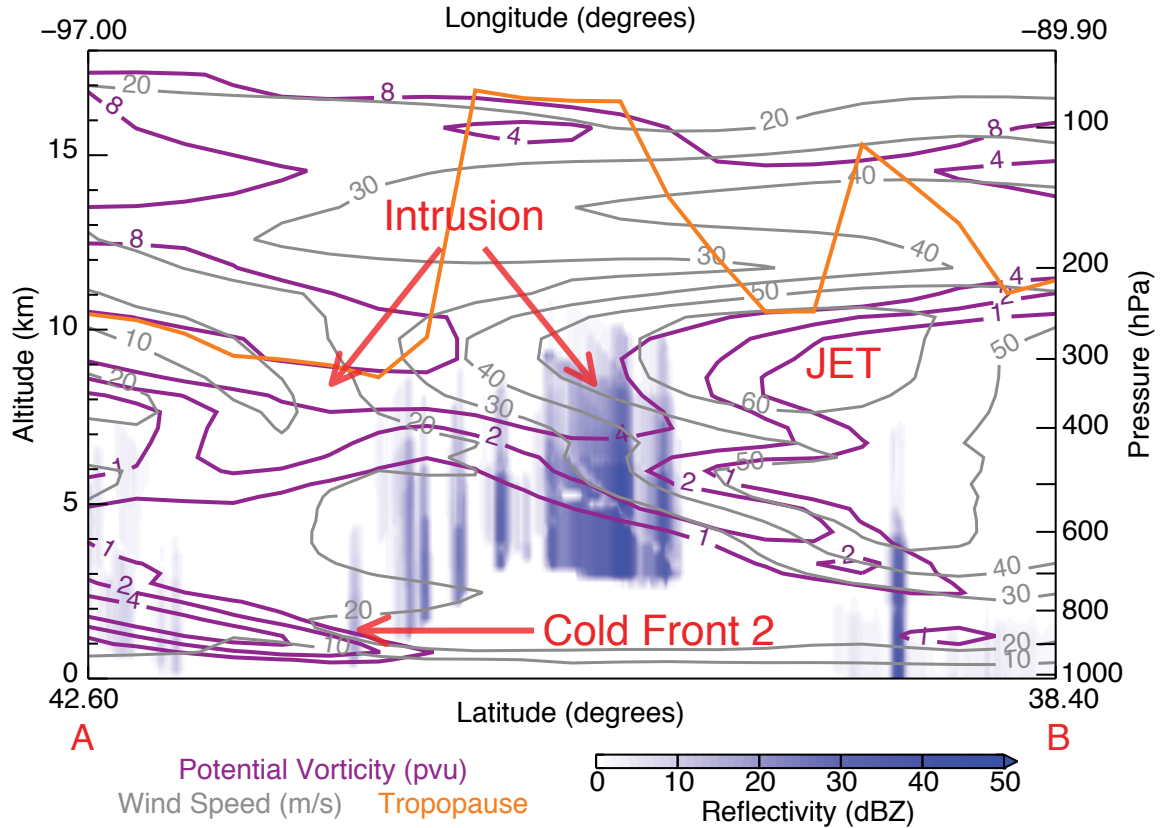
Fig. 38. For 11 April 2008 at 00 UTC, a vertical section of GFS potential vorticity (purple lines), wind speed (gray lines) and model output lapse-rate tropopause (orange line) and NEXRAD radar reflectivity (color-fill). The location of the section is shown by the thick red line in figures 37a & 37b.
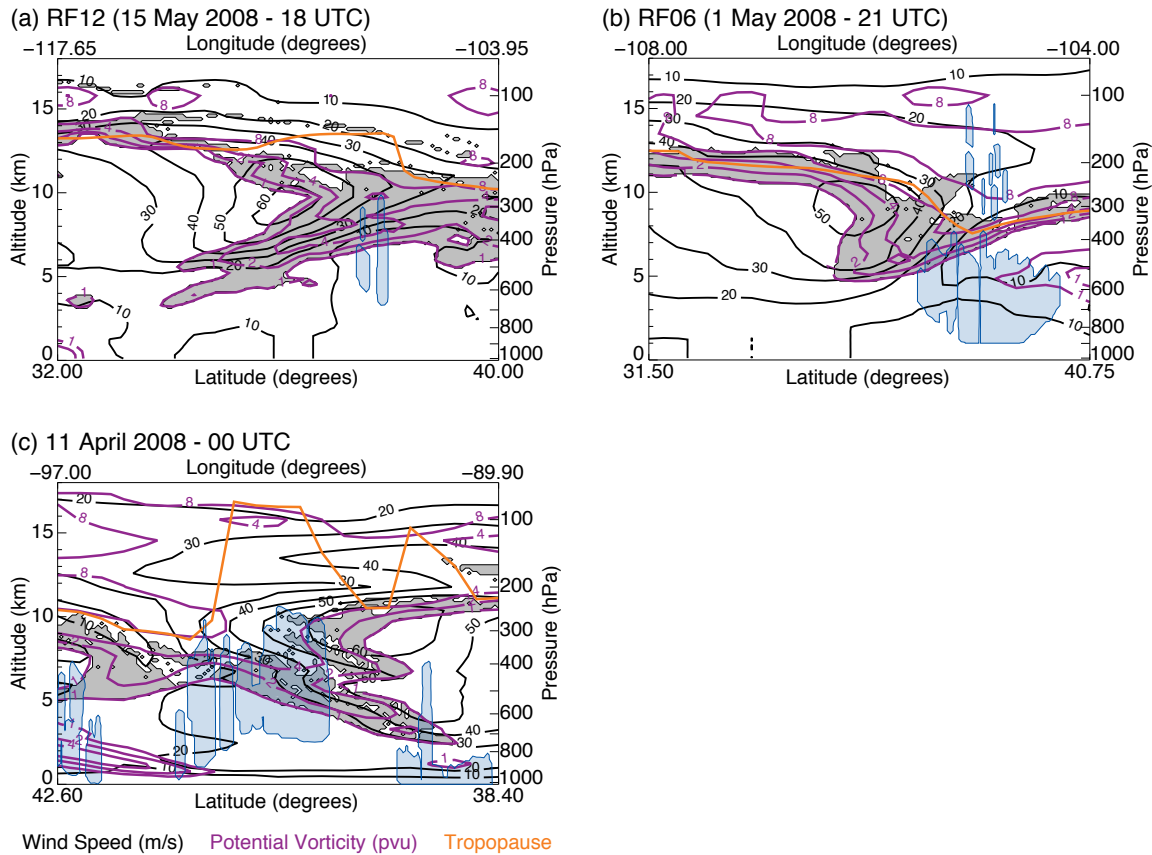
Fig. 39. Vertical sections of GFS analysis potential vorticity (PV, purple lines), wind speed (black lines) and model output lapse-rate tropopause (orange lines) and NEXRAD radar reflectivity ≥ 1 dBZ (blue color-fill) for (a) research flight 12 (RF12) parallel to the flight segment of convective injection, (b) research flight 6 (RF06) and (c) the 11 April 2008 case study. The gray color-filled areas indicate air with a stratospheric component that was transported into the troposphere, defined as forward trajectory particles with PV ≥ 1 pvu at the analysis time and at altitudes below the GFS lapse-rate tropopause 5 days later.
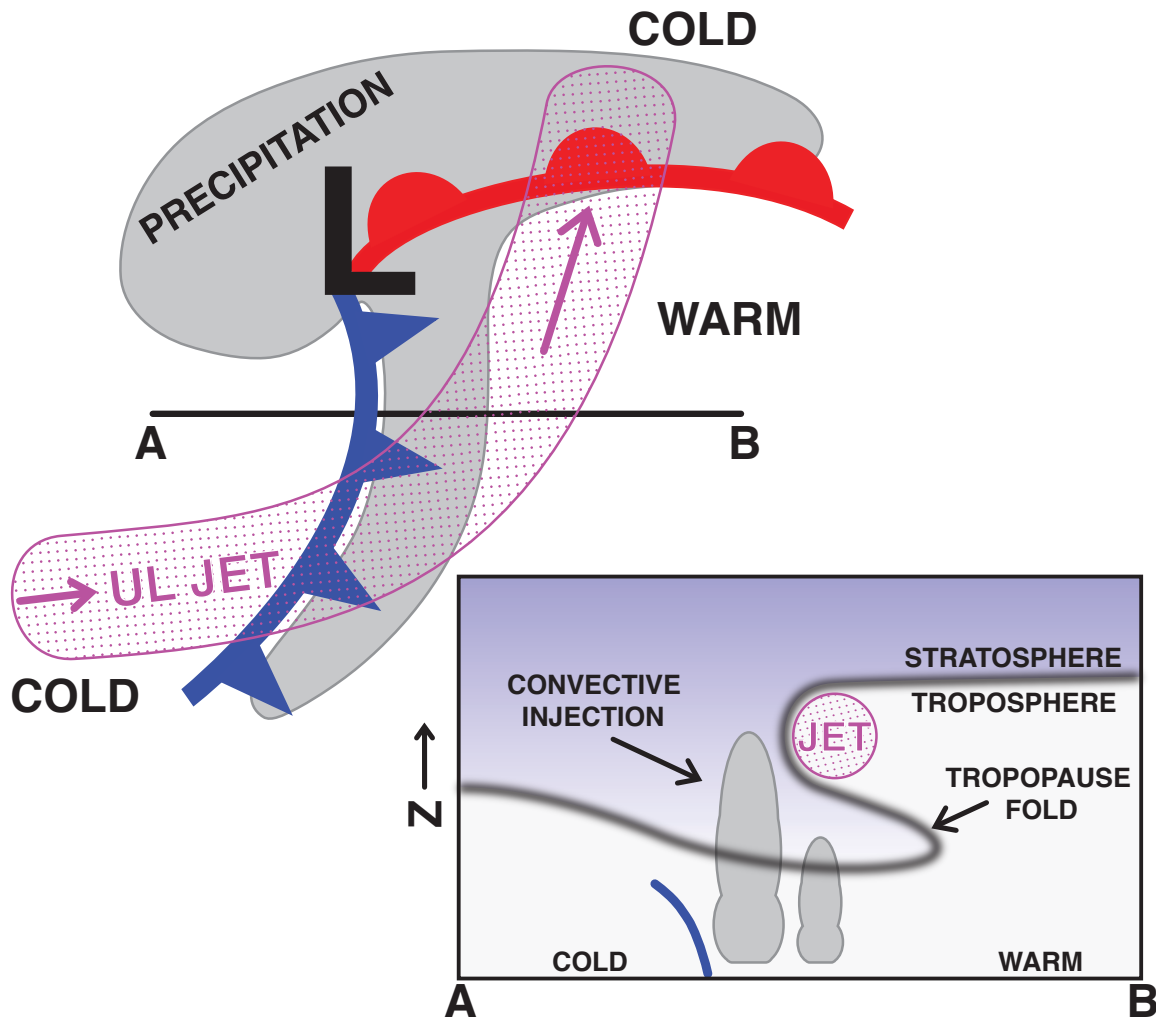
Fig. 40. Conceptual model of the synoptic meteorological conditions conducive to convective injection in stratospheric intrusions. The upper left is a representation of the associated surface and upper-level meteorological conditions. The vertical section, along line A-B, shows the stratospheric intrusion ahead of the surface cold front (a "split front") and location of convective injection.